Molecular simulation of fluid mixtures in bulk and at solid–liquid interfaces

BY

Jesse L. Kern

Submitted to the graduate degree program in Chemistry
and the Graduate Faculty of the University of Kansas in partial fulfillment of
the requirements for the degree of Doctor of Philosophy

Chairperson Prof. Brian B. Laird

Prof. Ward H. Thompson

Prof. Marco Caricato

Prof. Carey K. Johnson

Prof. Juan Bravo-Suarez

Date defended: 5-22-15

The Dissertation Committee for Jesse L. Kern
certifies that this is the approved version of the following dissertation:

Molecular simulation of fluid mixtures in bulk and at solid–liquid interfaces

Chairperson Prof. Brian B. Laird

Date approved: 5-29-15

Abstract

The properties of a diverse range of mixture systems at interfaces are investigated using a variety of computational techniques. Molecular simulation is used to examine the thermodynamic, structural, and transport properties of heterogeneous systems of theoretical and practical importance. The study of binary hard-sphere mixtures at a hard wall demonstrates the high accuracy of recently developed classical-density functionals. The study of aluminum–gallium solid–liquid heterogeneous interfaces predicts a significant amount of prefreezing of the liquid by adopting the structure of the solid surface. The study of ethylene-expanded methanol within model silica mesopores shows the effect of confinement and surface functionalzation on the mixture composition and transport inside of the pores.

From our molecular-dynamics study of binary hard-sphere fluid mixtures at a hard wall, we obtained high-precision calculations of the wall-fluid interfacial free energies, γ. We have considered mixtures of varying diameter ratio, $\alpha = 0.7, 0.8, 0.9$; mole fraction, $x_1 = 0.25, 0.50, 0.75$; and packing fraction, $\eta < 0.50$. Using Gibbs-Cahn Integration, γ is calculated from the system pressure, chemical potentials, and density profiles. Recent classical density-functional theory predictions agree very well with our results.

Structural, thermodynamic, and transport properties of the aluminum–gallium solid–liquid interface at 368 K are obtained for the (100), (110), and (111) orientations using molecular dynamics. Density, potential energy, stress, and diffusion

profiles perpendicular to the interface are calculated. The layers of Ga that form on the Al surface are strongly adsorbed and take the in-plane structure of the underlying crystal layers for all orientations, which results in significant compressive stress on the Ga atoms.

Bulk methanol–ethylene mixtures under vapor-liquid equilibrium conditions have been characterized using Monte Carlo and molecular dynamics. The simulated vapor-liquid coexistence curves for the pure-component and binary mixtures agree well with experiment, as do the mixture volumetric expansion results. Using chemical potentials obtained from the bulk simulations, the filling of a number of model silica mesopores with ethylene and methanol is simulated. We report the compositions of the confined fluid mixtures over a range of pressures and for three degrees of nominal pore hydrophobicity.

Contents

List of Figures

List of Tables

To my father

Chapter 1

Introduction

The study of interfaces and surfaces has become a vast field with applications in heterogeneous catalysis, renewable-energy technology, medical technology, and many more. Compared to the bulk regions of the phases in contact, atoms in the interfacial region have altered chemical and physical environments. For both natural and industrial processes, reactions taking place at interfaces are sensitive to these changes and exploit these new environments. Most of the current understanding of these environments comes from measurement of macroscopic system properties, but recent experimental and computational advances are allowing for new atomic-level measurements to be made on these complex systems. Each new microscopic insight from surface science studies can potentially have a positive economic, health, energy, or technological impact on society.

A detailed understanding of the properties of solid–liquid interfaces between chemically dissimilar materials is important for the description of intriguing and relevant phenomena such as wetting and heterogeneous nucleation. The structural

and thermodynamic properties of chemically heterogeneous solid–liquid interfaces, when compared to those of pure crystal–melt interfaces, remain poorly understood. Imaging techniques such as X-ray scattering and transmission electron microscopy (TEM) can be used to study such interfaces, but they are difficult, and the resolution is not as high as is desirable. Therefore, much of our information pertaining to the structure and thermodynamics of solid–liquid interfaces comes from atomistic simulation.

In this dissertation, a variety of condensed-phase interfacial systems are studied using computational techniques. The goal is to investigate how the atomistic behavior of matter influences the macroscopic properties of materials. Because microscopic details are immediately available in computer simulation, it is well-suited for studying the broad and diverse range of chemical and physical phenomena that can occur at interfaces. While much of the initial computational work in this area has focused on single-component systems, the three systems presented in this work are binary mixtures. The consideration of multiple components increases the complexity of the research problem.

This dissertation opens with this introduction, followed by the basic concepts of molecular simulation, the studies of three intriguing interfacial systems, and conclusion. Molecular dynamics is detailed in Chapter 2, and Monte Carlo is detailed in Chapter 3. The study of binary hard-sphere fluids at a hard wall is presented in Chapter 4. An analysis of the aluminum–gallium solid–liquid interface is presented in Chapter 5. The study of ethylene-expanded methanol in bulk and

confined within silica mesopores is presented in Chapter 6. Finally, the findings discussed in this dissertation are summarized in Chapter 7.

Model systems are useful in understanding phenomena at a fundamental level. The hard-sphere (HS) model is one that is used to isolate the effects of hard-core repulsion and particle geometry from inter-particle attraction. A HS fluid at a smooth, hard wall (HW) is one simple model for a chemically heterogeneous solid–liquid interface. Fundamental characteristics of the HS–HW system, such as the interfacial free energy, can be useful benchmarks used for comparison against the same values for real systems.

Liquid-metal embrittlement (LME) is the weakening that occurs in a metal or alloy polycrystal when it comes in contact with a liquid metal. LME is one of a number of mechanical degredation mechanisms of interest in materials science, and an understanding of the degradation mechanism should be desirable when developing new technologies that utilize a number of metals. One pair of metals that exhibit LME is solid aluminum and liquid gallium. A symmetric-tilt aluminum bicrystal, embrittled by gallium, is shown in Fig. 1.1 [1]. While LME is typically seen as a phenomenon to prevent from occuring, it has been utilized in the stuctural study of polycrystalline metals by way of exposing grain facets [2]. An example of an aluminum fracture surface obtained by LME is shown in Fig. 1.2 [3].

Researchers at the Center for Environmentally Beneficial Catalysis (CEBC) at the University of Kansas have developed a novel heterogenous catalyst for the epoxidation of ethylene by hydrogen peroxide. Ethylene is converted to ethylene oxide (EO) within metal-exchanged silica mesopores (Fig. 1.3). Methanol and

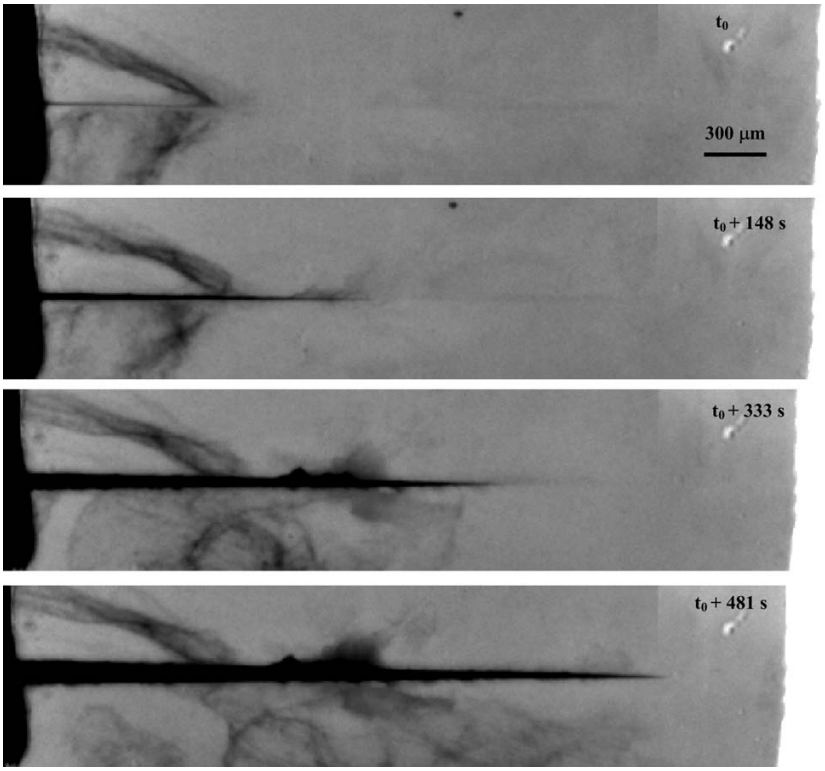

Figure 1.1: Symmetric-tilt aluminum bicrystal embrittlement by gallium. This particular bicrystal has a low-energy grain boundary, and a stress of about 5 MPa was applied in the direction normal to the grain boundary to induce LME. Figure reproduced from Reference [1].

water are present in the process as co-solvents, with methanol providing improved ethylene solubility and water providing hydrogen peroxide stability. Two key benefits of this CEBC epoxidation process are increased EO productivity (rate of EO produced per unit mass of catalyst) versus that of the conventional silver-based process and decreased formation of carbon dioxide from the direct burning of ethylene. It is desirable to understand the microscopic details of the CEBC process

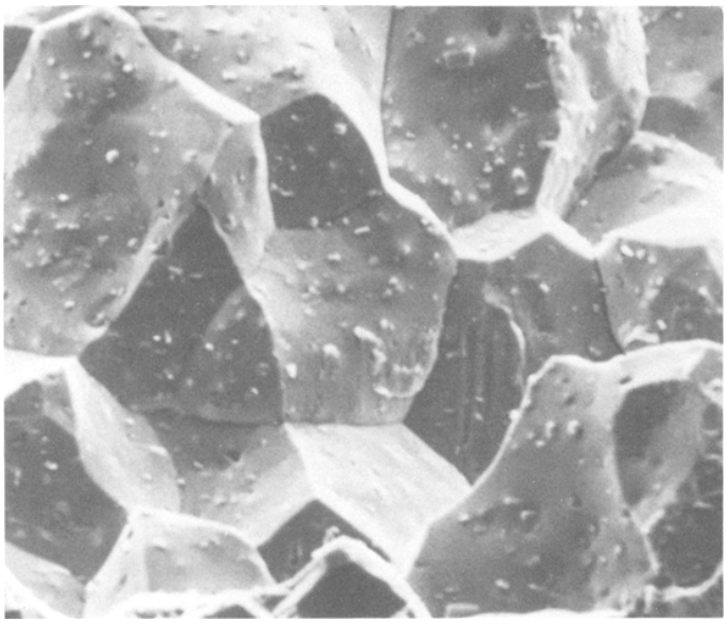

Figure 1.2: Fracture surface of commercial-grade aluminum, embrittled by gallium. The surface was obtained by introducing gallium into a grain boundary and applying strain in the surface-normal direction. The small defects are iron-rich impurities. Image magnification is a factor of 320. Figure reproduced from Reference [3].

so that it may be further improved, and this knowledge may also be used to develop guiding design principles for new processes.

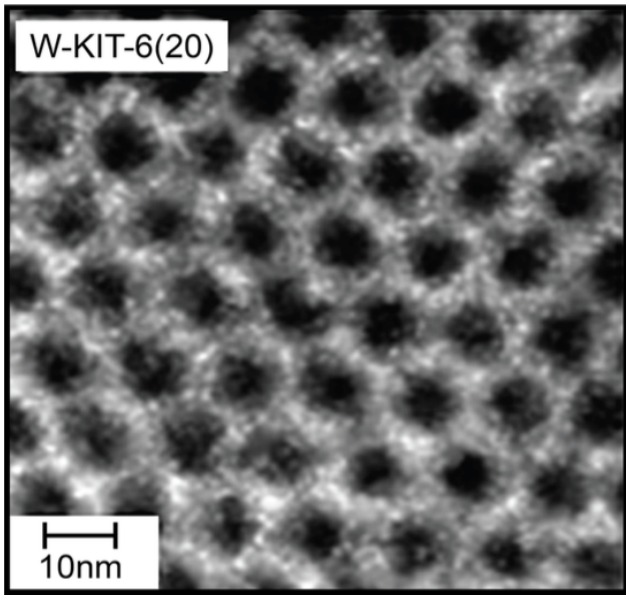

Figure 1.3: TEM image of silica mesopore network. The W-KIT-6(20) refers to a tungsten-doped KIT-6 morphology with a silicon:tungsten loading ratio of 20:1. The pore openings of this network are arranged hexagonally and have an average pore diameter of about 7 nm. Figure reproduced from Reference [4].

Chapter 2

Atomistic molecular-dynamics simulation methods

In general, the goal of atomistic simulation is to connect the microscopic quantities associated with atoms and molecules (namely, positions and momenta) with macroscopic measurables, such as temperature or pressure. Analytically, statistical mechanics can be used to relate microscopic and macroscopic variables through the use of partition functions and probability distributions. Classical molecular dynamics (MD) supplements statistical mechanics by using computers to generate system trajectories of positions and velocities using classical mechanics. This allows complicated, analytical, and exact thermodynamic equations to be approximated by straightforward, numerical equations.

Molecular-dynamics simulation is a well-established technique [5–7] that dates back to the hard-sphere simulations of Alder and Wainwright [8]. The primary benefit that MD has over standard Monte Carlo simulation (Chapter 3) is that MD is particularly suited for calculating time-dependent quantities, such as mean-square displacements or time-correlation functions, which can be used to determine

transport properties. Significant work in optimizing MD algorithms for parallel execution [9] provides a secondary benefit of increasingly fast execution speeds.

As the atomic/molecular description of MD simulation is rooted in classical mechanics, Hamiltonian dynamics is introduced in the first section of this chapter. Next, an overview of microcanonical dynamics is presented. Then, thermostats and barostats, mathematical tools used to enforce constant temperature and pressure for simulations in the canonical or isothermal-isobaric ensembles, are introduced. Finally, a simulation algorithm for hard-sphere dynamics is discussed.

2.1 Hamiltonian dynamics

An understanding of classical mechanics is essential in understanding MD methods. I provide here a quick review of Hamiltonian dynamics; a more thorough explanation can be found in Refs. [6, 7, 10]. The Hamiltonian formulation of dynamics provides a general framework for generating equations of motion from positions and momenta. The classical Hamiltonian H propagates the system through time, sampling ensemble configurational space. Within this manuscript, all Hamiltonians are constant over time, and thus explicit time independence is assumed in the following presentation of Hamiltonian dynamics. From these trajectories, averages over the sampled configurations are used to calculate macroscopic observable properties. The Hamiltonian for an N particle conservative system in three dimensions

is given by

$$H(q^{3N}, p^{3N}) = K(p^{3N}) + U(q^{3N}) = \sum_{i=1}^{N} \frac{\mathbf{p}_i^2}{2m_i} + \sum_{i=1}^{N} U(\mathbf{q}_i) \tag{2.1}$$

where K and U are the kinetic and potential energies, q is position, p is momentum, and m is mass. Taking K purely as a function of momenta and U purely as a function of positions is valid under the assumption of classical behavior.

Hamilton's equations of motion are

$$\dot{q}_\alpha = \frac{\partial H}{\partial p_\alpha} \tag{2.2}$$

$$\dot{p}_\alpha = -\frac{\partial H}{\partial q_\alpha} \tag{2.3}$$

for each Cartesian component α of position and momentum. Together, these constitute a set of $6N$ first-order differential equations. Substituting the full Hamiltonian into Eqs. 2.2 and 2.3 results in

$$\dot{q}_\alpha = p_\alpha / m \tag{2.4}$$

$$\dot{p}_\alpha = -\nabla U_\alpha = F_\alpha \tag{2.5}$$

which are consistent with the usual definition of linear momentum and with Newton's second law. One important property of the Hamiltonians used in this work is that they are conserved over time, that is, $dH/dt = 0$. Ensuring that this is true is a vital part of determining the validity of the molecular-dynamics protocol. In

practice, numerical integration is not exact, but the error that this introduces can be monitored and should be shown to be negligible for each simulation.

While the kinetic energy term of the Hamiltonian is general for unconstrained (non-rigid) dynamics, the potential energy may take many forms. In this manuscript, a number of potentials are considered. First, the hard-sphere model, whose pair potential ϕ_{ij} between spheres i and j is infinite within the hard core and zero elsewhere

$$\phi_{ij}(q_{ij}) = \begin{cases} \infty & q_{ij} < \sigma \\ 0 & q_{ij} \geq \sigma \end{cases} \tag{2.6}$$

for spheres of diameter σ and for interparticle separation q_{ij}. The second potential is the embedded-atom method (EAM) model, whose potential energy is given by the sum of a pair interation Φ and an energy F required to "embed" an atom into a background electron density ρ

$$U = \frac{1}{2}\sum_{i,j}\Phi(q_{ij}) + \sum_{i}F(\rho_i) \tag{2.7}$$

Third, molecular models, which include Lennard-Jones (LJ) and Coulombic intermolecular pair potentials, in addition to intramolecular bond, angle, and dihedral potential terms.

$$U = \sum_{i,j}\phi_{LJ}(q_{ij}) + \sum_{i,j}\phi_{Coulomb}(q_{ij}) + V_{bond} + V_{angle} + V_{dihedral} \tag{2.8}$$

where the intramolecular potentials V are functions of relative position within the molecular frame. Once the potential energy of a system is defined, the equations

of motion are specified, and dynamics can be carried out. Microcanonical (NVE), canonical (NVT), and isothermal-isobaric (NPT) dynamics are discussed in the following sections.

2.2 NVE dynamics

The microcanonical (NVE) statistical ensemble is the probability distribution of constant particle number, volume, and energy, which are all basic *extensive* thermodynamic properties. Given a form for the Hamiltonian, the positions and momenta of particles in the system can evolve through time. Because the Hamiltonian must be conserved, the total energy is also conserved, and exactly integrating Hamilton's equations will result in constant-energy dynamics. However, the numerical integration techniques used in computer simulation are not exact. Energy drift is easily monitored, and it is good practice to confirm that the drift is negligible.

The first step in numerically integrating the equations of motion is calculating the forces F_i on each particle. The forces can then be used to update the particle momenta p_i, which then influences the particle position q_i at some time Δt in the future. At this future time, new forces must be calculated, and the scheme is repeated. One of the most common of such integrators is the velocity-Verlet algorithm [6, 11]. The velocity Verlet equations

$$\mathbf{q}_i(t+\Delta t) = \mathbf{q}_i(t) + \Delta t \frac{\mathbf{p}_i(t)}{m_i} + \frac{\Delta t^2}{2m_i}\mathbf{F}_i(t) \tag{2.9}$$

$$\mathbf{p}_i(t+\Delta t) = \mathbf{p}_i(t) + \frac{\Delta t}{2}[\mathbf{F}_i(t) + \mathbf{F}_i(t+\Delta t)] \tag{2.10}$$

result from basic algebraic manipulation of the Taylor series expansions (out to the quadratic term) of positions and momenta. Two important properties of the velocity-Verlet algorithm are that it is both *time reversible* and *symplectic*, and thus the algorithm is numerically stable. Time reversibility means that the dynamical equations are invariant under a sign change in time. A symplectic integrator preserves the volume and orientation of phase space over time.

While the description of NVE dynamics is fairly straightforward, the simple observation that most experiments are not conducted at constant energy suggests that there are drawbacks to considering only the microcanonical Hamiltonian. Extended Hamiltonian dynamics for alternate ensembles are discussed in the next section.

2.3 NVT and NPT dynamics

While the NVE framework lays the foundation for molecular-dynamics simulation, extensions to the Hamiltonian which allow for energy and volume fluctuations required the development of special mathematical tools, called *thermostats* and *barostats*. A thermostat attempts to restrict the dynamics of a system to a constant temperature, which results in a canonical (NVT) ensemble. The addition of a barostat to restrict a system to constant pressure results in an isothermal-isobaric (NPT) ensemble.

2.3.1 Thermostats for NVT dynamics

The canonical (NVT) ensemble is the probability distribution of constant particle number N, volume V, and temperature T. For the temperature to be held constant in MD simulations, methods ranging from simple velocity rescaling algorithms to the extended Hamiltonian of Nosé [12, 13] and its modifications [14, 15] were developed.

The original Nosé Hamiltonian introduces a new dynamical unitless variable s with conjugate momentum π_s and Nosé mass Q. The actual units for π_s and Q are energy $\times$ time and energy $\times$ time^2, respectively. The Nosé mass Q can be related to a timescale of energy fluctuations τ_{fluc} by the equation $Q = gk_BT\tau_{fluc}^2$, where k_B is Boltzmann's constant and g is a parameter that is one greater than the number of degrees of freedom of the system. Particle momenta p_i are scaled to Nosé momenta $\tilde{p}_i$ by $p_i = \tilde{p}_i/s$. The Nosé Hamiltonian is

$$H_{\text{Nosé}} = \sum_i \frac{\tilde{p}_i^2}{2m_i s^2} + U(q) + \frac{\pi_s}{2Q} + gk_BT\ln s \tag{2.11}$$

It is the variable s that determines whether the instantaneous temperature is higher or lower than the target temperature and scales velocities accordingly. Inconveniently, the intrinsic Nosé time τ is dynamically rescaled and related to the real time t by $\frac{d\tau}{dt} = s$. The Nosé equations of motion in τ are

$$\dot{q}_i = \frac{\tilde{p}_i}{m_i s^2} \tag{2.12}$$

$$\dot{\tilde{p}}_i = -\frac{\partial U(q_i)}{\partial q_i} \tag{2.13}$$

$$\dot{s} = \frac{\pi_s}{Q} \tag{2.14}$$

$$\dot{\pi}_s = \sum \frac{\tilde{p}_i^2}{2m_i s^3} - \frac{g k_B T}{s} \tag{2.15}$$

Because integrators typically use fixed timestep, using the dynamic Nosé time τ is cumbersome. Further modifications by Hoover [14] resulted in the Nosé-Hoover equations of motion, which retain evenly distributed points in real time. Applying the transformations $\eta = \ln s$ and $\dot{\eta} = \xi$ yields

$$\dot{q}_i = \frac{p_i}{m_i} \tag{2.16}$$

$$\dot{p}_i = -\frac{\partial U(q_i)}{\partial q_i} - \xi p_i \tag{2.17}$$

$$\dot{\xi} = \frac{1}{Q}\left(\sum_i \frac{p_i^2}{m_i} - g k_B T\right) \tag{2.18}$$

2.3.2 Barostats for NPT dynamics

The isothermal-isobaric (NPT) ensemble is the probability distribution of constant particle number N, pressure P, and temperature T. Dynamics in the NPT ensemble require not only a thermostat, but also a barostat, which ensures that the average internal pressure of the system equals the applied external pressure. Thus, volume is taken as a dynamic variable in phase space, an idea which is supported by the work-virial theorem [10]. Presented here is an overview of the original method of

Andersen [16], which begins with the scaling transformations

$$\hat{\mathbf{q}}_i = V^{-1/3}\mathbf{q}_i \tag{2.19}$$

$$\hat{\mathbf{p}}_i = V^{1/3}\mathbf{p}_i \tag{2.20}$$

which make coordinates and momenta explicitly dependent on volume. Incorporating these scaled values, pressure, volume, and the volume momentum p_V into the Hamiltonian results in

$$H_{\text{Andersen}} = \sum_i \frac{V^{-2/3}\hat{\mathbf{p}}_i^2}{2m_i} + U(V^{1/3}\hat{\mathbf{q}}) + \frac{p_V^2}{2W} + PV \tag{2.21}$$

where $W = gk_BT\tau_{\text{b}}^2$ and τ_{b} is a timescale for volume fluctuations, with similar function as the Nosé mass. The units of p_V and W are energy $\times$ time and energy $\times$ time^2, respectively. Applying Hamilton's equations and unscaling the particle coordinates and momenta yields

$$\dot{\mathbf{q}}_i = \frac{\mathbf{p}_i}{m_i} + \frac{\dot{V}}{3V}\mathbf{q}_i \tag{2.22}$$

$$\dot{\mathbf{p}}_i = -\frac{\partial U}{\partial \mathbf{q}_i} - \frac{\dot{V}}{3V}\mathbf{p}_i \tag{2.23}$$

$$\dot{V} = \frac{p_V}{W} \tag{2.24}$$

$$\dot{p}_V = \frac{1}{3V}\sum_i \left[\frac{\mathbf{p}_i^2}{m_i} - \frac{\partial U}{\partial \mathbf{q}_i}\cdot\mathbf{q}_i\right] - P \tag{2.25}$$

as the equations of motion for the Andersen Hamiltonian. Combining the Andersen and Nosé-Hoover Hamiltonians produces a Hamiltonian capable of sampling the NPT distribution.

For the molecular-dynamics simulations of the aluminum–gallium and ethylene–methanol systems presented in this work, the LAMMPS simulation package from Sandia National Laboratories was used [9]. To control the temperature in the MD simulations, the `fix nvt` command is used, in which both a target temperature and a damping factor τ_{damp} are specified. The Nosé mass Q relates to τ_{damp} by the equation $Q = gk_BT\tau_{damp}^2$. Of note, the LAMMPS `fix nvt` command invokes an extension of the Nosé-Hoover thermostat called Nosé-Hoover Chains [17], in which $M > 1$ thermostats are introduced. Only η_1 interacts with the N particles, and each η_i interacts with η_{i-1} for $2 < i < M$, resulting in the chain of thermostats. Dynamics for unconstrained (non-rigid) systems are performed with $M = 3$, and rigid-body dynamics are performed with $M = 10$. For isothermal-isobaric dynamics, the `fix npt` command is used, which adds a target pressure and barostat damping factor. This command invokes the Nosé-Hoover barostat [18], an extension of the Andersen barostat.

2.4 Hard-sphere dynamics

The description of dynamics in the previous sections is universally valid for systems with smooth, continuous interparticle interactions, but fail when discontinuities are introduced. An example of such a failure might be a velocity-Verlet timestep

which moves particles from a configuration where the energy is finite to one where the energy is infinite; that is, ΔU is uncontrollably large for Δt. Because the interaction energy in a system of hard spheres is defined as either zero or infinity at all separations, an alternative framework for the dynamics of the system must be adopted. Generally speaking, the integration algorithm is based on *events*, rather than *timesteps*, so that the elastic hard-sphere collisions can be resolved instantaneously, whenever they might occur [5]. The times of potential future collision events are calculated, and the system is advanced to the earliest upcoming event. The event is resolved by calculating the new momenta based on the momenta at collision, after which future events for the collision pair must be recalculated. These protocol steps and some optimization techniques are detailed in the following subsections.

2.4.1 Collision times

A hard-sphere collision is defined to occur when the distance between the centers of two spheres i and j becomes equal to their average diameter $\sigma_{ij} = (\sigma_i + \sigma_j)/2$. Times of collision can be calculated from the relative position $\mathbf{r}_{ij} = \mathbf{r}_i - \mathbf{r}_j$ and relative velocity $\mathbf{v}_{ij} = \mathbf{v}_i - \mathbf{v}_j$ of the collision pair by solving for times t_c in the future when $\mathbf{r}_{ij} = \sigma_{ij}$. The collision time $t_{ij} = t_c - t_0$ for pair i and j, relative to some reference time t_0, is the amount of time the spheres will travel unobstructed before collision. Thus, a collision occurs at

$$\left|\mathbf{r}_{ij}(t_0) + t_{ij}\mathbf{v}_{ij}(t_0)\right| = \sigma_{ij} \tag{2.26}$$

which can be converted to a quadratic equation by squaring

$$v_{ij}^2 t_{ij}^2 + 2b_{ij}t_{ij} + r_{ij}^2 - \sigma_{ij}^2 = 0 \tag{2.27}$$

where $b_{ij} = \mathbf{r}_{ij} \cdot \mathbf{v}_{ij}$. Eq. 2.27 has no real solutions for $b_{ij} > 0$, indicating that the spheres are moving away from one another. Given $b_{ij} < 0$, a solution is found if the discriminant is nonnegative

$$b_{ij}^2 - v_{ij}^2(r_{ij}^2 - \sigma_{ij}^2) \geq 0 \tag{2.28}$$

and the collision time is given by the smaller (earlier) solution

$$t_{ij} = \frac{-b_{ij} - \sqrt{b_{ij}^2 - v_{ij}^2(r_{ij}^2 - \sigma_{ij}^2)}}{v_{ij}^2} \tag{2.29}$$

The earliest of all future collision times for all possible collision pairs is chosen, and all spheres are advanced forward in time until the collision occurs. Based on the velocities at collision, new velocities for the collision pair are calculated.

2.4.2 Collision mechanics

The outcome of a collision of hard spheres of equal mass is a change in velocities that conserves energy and linear momentum

$$v_i^2 + v_j^2 = v_i'^2 + v_j'^2 \tag{2.30}$$

$$\mathbf{v}_i + \mathbf{v}_j = \mathbf{v}'_i + \mathbf{v}'_j \tag{2.31}$$

for initial and final velocity vectors $\mathbf{v}$ and $\mathbf{v}'$. This requires that the change in relative velocity be precisely along the line connecting the sphere centers. Thus, the initial and final relative velocites are related by

$$\mathbf{v}'_{ij} \cdot \mathbf{r}_{ij}(t_c) = -\mathbf{v}_{ij} \cdot \mathbf{r}_{ij}(t_c) \tag{2.32}$$

and the changes in particle velocities are

$$\Delta\mathbf{v}_i = -\Delta\mathbf{v}_j = -\frac{b_{ij}(t_c)}{\sigma_{ij}}\mathbf{r}_{ij}(t_c) \tag{2.33}$$

where b_{ij} is recalculated at the time of collision. At this point, the collision information can be recorded for use in calculating other properties of interest, such as the pressure, and the algorithm cycles back to determining the time to the next collision. One notable feature of the calculation of collision times and mechanics is that the equations used are exact, and thus yield exact simulation trajectories within machine precision.

Artificial "events" occuring between collisions can be added to the simulation algorithm. For example, regular output of all of the particle positions might be scheduled for post-processing. In such cases, the event is added to the list of future events and occurs when it is the next event in line, but only after the particle positions are updated to the new event time.

2.4.3 Algorithm optimization

The majority of the computational effort in a hard-sphere dynamics program goes into calculating, storing, and retrieving the *time* that events will occur; updating the system as a result of an event is quick and straightforward. The two primary optimization techniques for hard-sphere dynamics code are the use of a cell subdivision scheme and and event calendar.

The cell subdivision scheme allows one to calculate more efficiently future collision times by ignoring potential collision partners that are too far separated. For systems with smooth, continuous potential energy interactions, such a determination of near versus far is implemented with a neighbor list using a radial distance cutoff. For a HS system, interactions only occur one pair at a time, and a more optimal scheme is to divide the entire simulation cell into smaller subcells. If the edges of the cubic subcell are at least the size of the hard sphere diameter, then collisions are guaranteed to occur only between spheres occupying adjacent subcells. Collision times can thus be calculated between partners in a localized volume. While tracking subcell occupancy requires additional effort, the overall workload is reduced by considering vastly fewer collision pairs. Subcell boundary crossings can be treated in the same way as a periodic boundary crossing. When a sphere crosses a boundary, new collision times are calculated based on the updated subcell adjacency.

Proper management of the vast number of boundary crossings and collision events is vital for efficient dynamics code. Such an *event calendar* contains the constantly updated event information, and in this application it takes the form of a

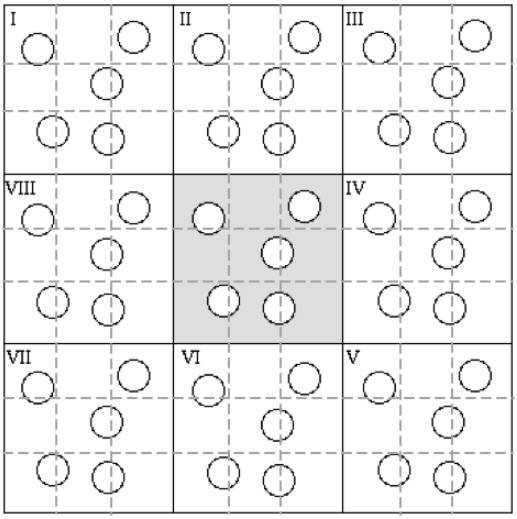

Figure 2.1: Subcell scheme example in two dimensions. The center simulation cell is shown with its periodic images I–VIII, separated with solid, black lines. The cell is divided into nine subcell units, separated by dashed, gray lines. The side length of each subcell greater than the sphere diameter, thus potential collision events are considered only between spheres in neighboring subcells. Figure reproduced from private correspondence with R. L. Davidchack.

binary event tree [19, 20]. The dynamics code may operate on the event tree by adding new events, deleting existing events, or retrieving the earliest event. When a collision event is retrieved and processed, all existing events involving either collision partner must be deleted, and the event tree is reorganized. Similarly, when it is time to add a new event, it must be possible to navigate the tree and insert the event at the appropriate tree position, or node. Practically, this is accomplished by parent/descendant pointers and circularly linked lists. An example event tree is shown in Fig. 2.2, and further details along with the pertinent functions/subroutines can be found in Ref. [7].

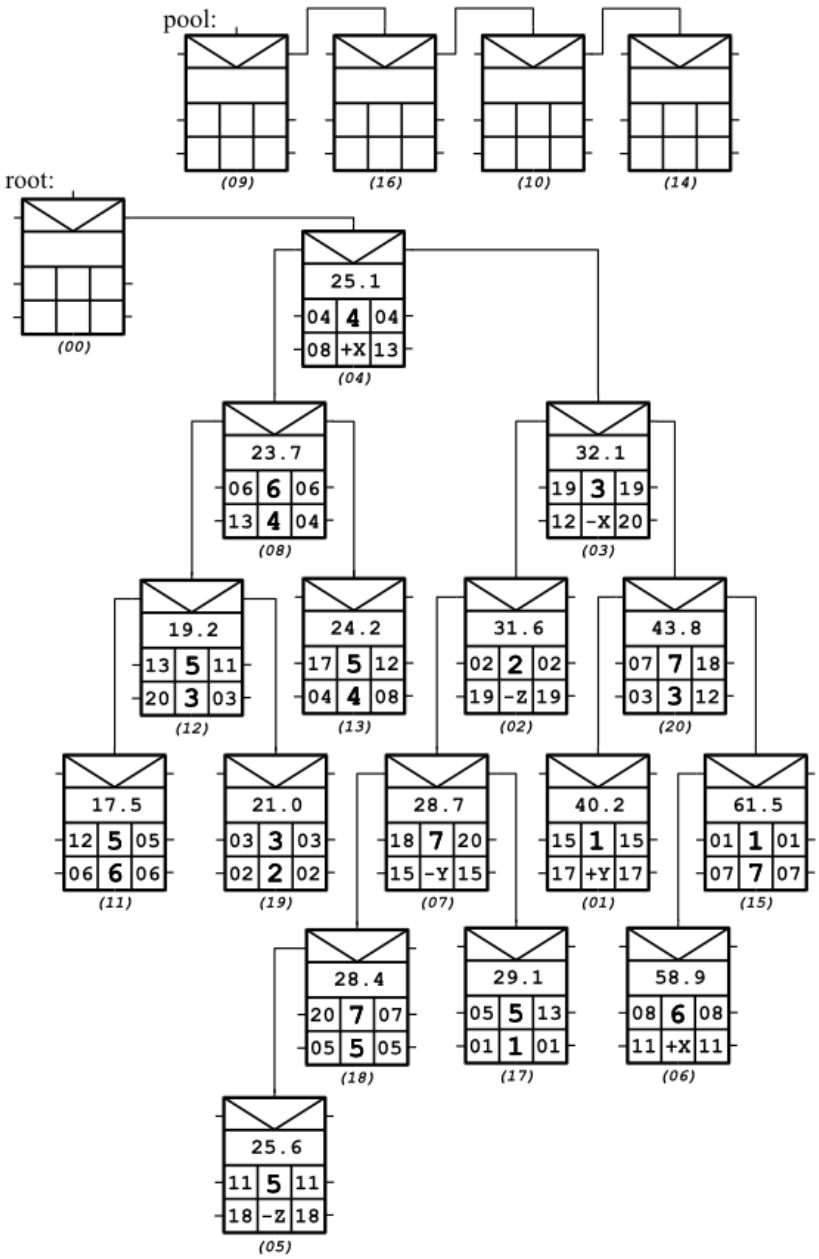

Figure 2.2: Miniature event calendar example. Each node on the tree stores the event time, sphere ID, and collision partner ID or subcell face crossing information. Below each node is a pointer address. The numbers on the left and right of the nodes represent pointers for navigating the circular lists. Figure reproduced from Reference [7].

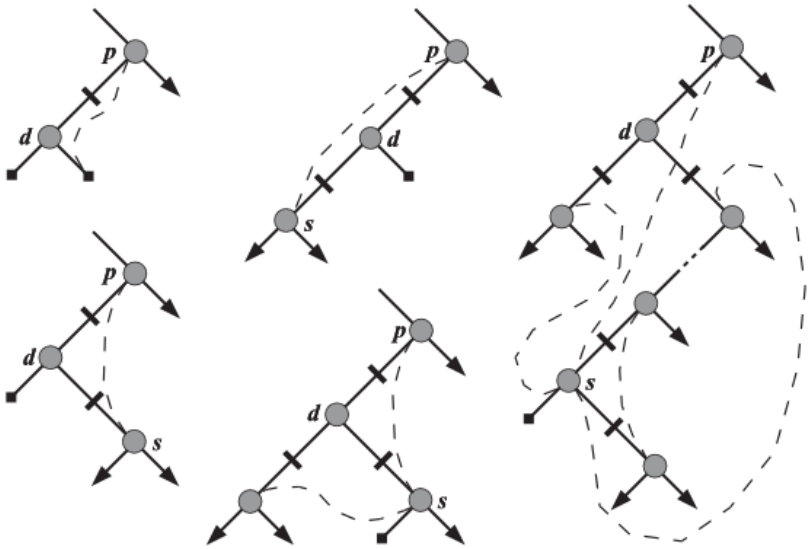

Figure 2.3: Depictions of pointer rearrangements. Pointers are continually updated as events are added or removed from the tree. Deleted nodes are indicated by d, and a pointer is added from p to s. Other alterations may also occur. Figure reproduced from Reference [7].

Chapter 3

Monte Carlo simulation methods

Chapter 2 presented molecular-dynamics (MD) methods for sampling the phase-space distributions of statistical-mechanical ensembles. The dynamic framework is intuitively motivated by classical mechanics, but dynamic sampling is unnecessary for sampling equilibrium ensemble properties. A sampling technique known as the Monte Carlo (MC) method [21, 22], as its name implies, is driven by chance. In computer simulations, chance is implemented by using random number generators to produce a *pseudo*-random, unbiased collection of numbers for use in MC sampling algorithms. Sampling refers to the estimation of a parameter of a population by observing a smaller, representative group (the sample) within the population. Such a thermodynamic population might be an ensemble of N gas-phase atoms, and one might use Monte Carlo simulation to sample some finite number of N atom positions. Measurements can be made on these samples for estimating the properties of the ensemble.

One common pedagogical example of Monte Carlo is the estimation of π by generating trial points within a circle of radius 1 inscribed within a 2×2 square. The ratio of the area of the circle to the area of the square is $\pi/4$, and thus the probability that a single point generated randomly within the square (denoted as a trial) also lies within the circle (denoted as a success) is $\pi/4$. For a sufficiently large number of trials, the ratio of successes to trials can approximate π out to arbitrary precision

$$\frac{\text{Area of circle}}{\text{Area of square}} = \frac{\pi}{4} \approx \frac{N_{\text{Successes}}}{N_{\text{Trials}}} \tag{3.1}$$

One method of sampling trials is to generate independently the set of N_{Trials} ordered pairs (x_i, y_i). This is known as direct sampling. Another method is to choose a starting point, and generate N_{trials} displacements $(\Delta x_i, \Delta y_i)$ from the current position. The probability of generating a new configuration at trial $i+1$ depends only on the preceding configuration at trial i and not on any earlier configurations; it is said that the process is *memoryless*. This defines what is known as Markov-chain sampling. A comparison between these two sampling methods is illustrated in Fig. 3.1. Note that direct sampling trivially forms a Markov chain, because the process is indeed memoryless, up to and including the current state. Markov-chain sampling is an important foundational concept for the Metropolis Monte Carlo algorithm, which is further discussed in Section 3.1.

Molecular dynamics and Monte Carlo are complementary techniques. MD is a deterministic approach that yields an actual system trajectory based on molecular mechanics. Thermodynamic and transport information can be extracted from

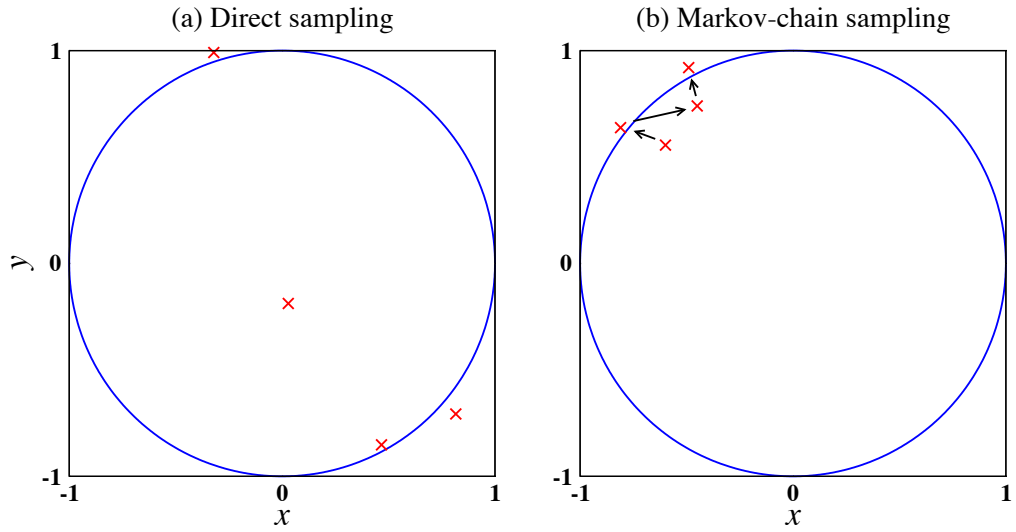

Figure 3.1: Comparison of (a) direct versus (b) Markov-chain sampling of the estimation of π. Trial coordinates (x_i, y_i) are generated independently in direct sampling. For Markov-chain sampling, each new trial depends on the current position. While each trial in the direct method can sample from the entire available area, many trials are required in the Markov-chain method to traverse the square. Given a sufficient number of trials, both methods will provide a successful estimation of π.

the trajectory and used to describe the state of the system. However, due to the deterministic nature of MD, one might find the lack of freedom to control the simulation parameters to be a drawback. The stochastic nature of MC simulation can allow for much greater flexibility in choosing the kinds of "moves" that describe the behavior of the system. For example, one might decide to add or remove particles during a simulation, allowing the number of particles to fluctuate. In the grand canonical (μVT) ensemble, for example, the instantaneous particle number is not held constant and is instead determined by the external chemical potential μ. In the Gibbs ensemble, the phase-space distribution of a system of two

or more distinct regions in equilibrium internally and with one another, particles can be moved between separate simulation cells. Grand Canonical Monte Carlo (GCMC) and Gibbs Ensemble Monte Carlo (GEMC) are further discussed in Sections 3.3 and 3.4.

3.1 Metropolis Monte Carlo

The Metropolis algorithm, proposed by Metropolis, *et al.*, in 1953 [22] forms the foundation for the efficient use of Monte Carlo methods in molecular simulation. In the original Monte Carlo method, configurations are uniformly and directly sampled and assigned Boltzmann weights of e^{-E/k_BT}. In contrast, configurations in Metropolis Monte Carlo are sampled with probability e^{-E/k_BT} and weighted uniformly. The benefit is apparent when one considers the direct sampling of dense systems, wherein a great many high-energy (hence, low-weight) configurations will be generated for each low-energy configuration. For hard-core interactions as in a hard-sphere fluid, the unfavorable configurations would have zero weight, and the computational effort put into generating the configuration goes entirely wasted.

This approach is implemented by first initializing the molecular system in some configuration. Using the rules of Markov-chain sampling, a displacement from the current configuration is chosen. For example, in an atomic system, one atom is chosen at random, and its position is changed by some amount $(\nu_1\Delta_{max}, \nu_2\Delta_{max}, \nu_3\Delta_{max})$ for $\nu_i \in (-1, 1)$ and maximum displacement Δ_{max}. The difference in energies $\Delta E = E_f - E_i$ is calculated, and the transition probability

$T(f \leftarrow i)$ becomes $\min[1, e^{-\Delta E/k_B T}]$. That is, a move resulting in a decrease in energy is always accepted, but a move which increases the energy is accepted $e^{-\Delta E/k_B T}$ of the time. When a move is rejected, the system is reverted back to its initial configuration, and this repeat configuration is considered an additional occurrence in the simulation trajectory for the purpose of computing ensemble averages. Note that the role of temperature in Monte Carlo simulation is to influence the acceptance probabilities and has no direct meaning as a measure of kinetic energy.

One other feature critical to Monte Carlo is that of detailed balance [22]. The detailed balance condition is sufficient to ensure that the process is microscopically reversible and unbiased. Considering two states a and b, detailed balance means the transition probability $T(b \leftarrow a)$ of the move from a to b must be the same as $T(a \leftarrow b)$ of the move from b to a. The transition probability $T(b \leftarrow a)$ can be thought of as the product of three terms: $p(a)$, the probability of being in state a; $\pi(b \leftarrow a)$, the probability of generating the trial move from a to b; $acc(b \leftarrow a)$, the probability of accepting the trial move from a to b. Thus,

$$T(b \leftarrow a) = T(a \leftarrow b) \tag{3.2}$$

$$p(a)\pi(b \leftarrow a)acc(b \leftarrow a) = p(b)\pi(a \leftarrow b)acc(a \leftarrow b) \tag{3.3}$$

As the probability of being in any state is given by the Boltzmann factor $e^{-E/k_B T}$, substitution and rearrangement of Eq. 3.3 results in

$$\frac{acc(b \leftarrow a)}{acc(a \leftarrow b)} = \frac{\pi(a \leftarrow b)p(b)}{\pi(b \leftarrow a)p(a)} = \frac{\pi(a \leftarrow b)}{\pi(b \leftarrow a)} \times e^{-(E_b - E_a)/k_B T} \tag{3.4}$$

The Metropolis acceptance rule $\min[1, e^{-\Delta E/k_B T}]$ is recovered by setting $\pi(a \leftarrow b) = \pi(b \leftarrow a)$. This implies that the probability of *attempting* $b \leftarrow a$ must be the same as that of $a \leftarrow b$ in order to ensure proper sampling.

3.2 Canonical MC

In the canonical ensemble, the particle number N, volume V, and temperature T are fixed. For this closed, rigid system, the only allowed Monte Carlo moves are displacements of the N particles. This would simply be single-particle displacements for an atomic system. The handling of molecular species would require the inclusion of all possible intra-molecular rearrangements, e.g., bond and angle perturbations in flexible water. The acceptance rule for a single-particle move will take the form of $\min[1, e^{-\Delta E/k_B T}]$, as the probability to be in any canonical state is the Boltzmann factor $e^{-E/k_B T}$.

3.3 Grand Canonical MC

The primary use of Grand Canonical Monte Carlo (GCMC) [23, 24] is to simulate systems which are open to material exchange with the surroundings. This ensemble allows for density fluctuations at fixed volume V and temperature T by allowing particles to be inserted into and deleted from the system according to an external chemical potential μ. For bulk systems, NPT simulation is generally considered to be more efficient at sampling these density fluctuations, but μVT simulation

has become a favored method for sampling open systems at interfaces or under confinement. Unfortunately, the efficiency of GCMC becomes low for dense or ordered systems as a result of low insertion/deletion rates due to large values of ΔE.

In addition to the moves allowed in canonical MC, particle insertions and deletions are introduced to allow N to fluctuate with respect to μ. Some derivation [10] from the grand partition function Ξ gives the probability p of being in configuration q^N at V and T as

$$p(N,q^N) \propto \frac{(zV)^N e^{-E(q^N)/k_BT}}{N!} \tag{3.5}$$

where the activity $z = \exp(\mu/k_BT)/\Lambda^3$, $\Lambda = \sqrt{\frac{h^2}{2\pi m k_B T}}$ is the thermal wavelength of the particle, and h is Planck's constant. This results in the insertion and deletion acceptance rules

$$acc(N+1 \leftarrow N) = \min\left[1, \frac{p(N+1)}{p(N)}\right]; \quad \frac{p(N+1)}{p(N)} = \frac{zVe^{-\Delta E/k_BT}}{N+1} \tag{3.6}$$

$$acc(N-1 \leftarrow N) = \min\left[1, \frac{p(N-1)}{p(N)}\right]; \quad \frac{p(N-1)}{p(N)} = \frac{Ne^{-\Delta E/k_BT}}{zV} \tag{3.7}$$

which, when taken with the single-particle rules, form the basics of the GCMC method [6, 10].

In order to obey detailed balance, one must ensure that the probabilities of attempting insertions and deletions are equal and do not depend on the current number of particles. Acceptable move probabilities might be 60%, 20%, and 20%

for single-particle moves, insertion, and deletion, respectively. If a single-particle move is chosen, the probability to move each particle becomes $1/N$.

In this manuscript, GCMC is used to fill a silica mesopore assumed to be in contact with a saturated mixture of ethylene and methanol as the surroundings. A prerequisite for performing these simulations is knowledge of the chemical potentials of ethylene and methanol at saturation (vapor-liquid coexistence). Therefore, a method capable of determining phase equilibria is required.

3.4 Gibbs Ensemble MC

Gibbs Ensemble Monte Carlo (GEMC) simulations [25,26] are the preferred choice for phase-equilibrium calculations involving liquids and gases. These simulations involve fixed particle number, volume, and temperature; however, the particles are separated into two (or more) non-interacting boxes that comprise the total volume. The basic GEMC moves are particle displacements, volume changes, and transfers of a particle from one box to another.

The introduction of a multi-box simulation allows for direct modeling of phase coexistence such as vapor-liquid equilibrium (VLE). Based on the number of components and phases present, the Gibbs phase rule [27] is used to determine the degrees of freedom of the system. Practically, for example, one degree of freedom results in NVT-GEMC for the calculation of pure component VLE, but two degrees of freedom results in NPT-GEMC for binary mixture VLE.

Two Monte Carlo moves present in GEMC that have not yet been introduced are volume changes and particle transfers [10]. The volume-change move differs between NVT and NPT implementations. For boxes A and B, NVT-GEMC conserves the total volume $V_{tot} = V_A + V_B$, and the volume move will increase the volume of one box by ΔV and decrease that of the other by the same amount. The NPT equivalent move only attempts volume changes of a single box and accepts the volume change in accordance with the specified external pressure. The form of the single-box (NPT) volume move acceptance rule is

$$\begin{aligned} acc(V + \Delta V \leftarrow V) &= \min\left[1, \frac{p(V+\Delta V)}{p(V)}\right]; \\ \frac{p(V+\Delta V)}{p(V)} &= \frac{(V+\Delta V)^N}{V^N} \times e^{-\beta(\Delta E + P\Delta V)} \end{aligned} \tag{3.8}$$

whereas the coupled-box (NVT) volume move acceptance rule is

$$\begin{aligned} acc((V_A + \Delta V, V_B - \Delta V) \leftarrow (V_A, V_B)) &= \min\left[1, \frac{p(V_A+\Delta V, V_B-\Delta V)}{p(V_A, V_B)}\right]; \\ \frac{p(V_A+\Delta V, V_B-\Delta V)}{p(V_A, V_B)} &= \frac{(V_A+\Delta V)^{N_A}(V_B-\Delta V)^{N_B}}{V_A^{N_A} V_B^{N_B}} \times e^{-\beta(\Delta E_A + \Delta E_B)} \end{aligned} \tag{3.9}$$

where V_α, N_α, and ΔE_α are the volume, particle number, and energy change in box α. Volume moves are computationally expensive. Because each particle must be scaled to a new position, all pair potentials must be recomputed to find ΔE. For this reason, the probability of choosing a volume move is often set near one or two percent. The acceptance rule for a particle transfer can be derived in a similar

fashion as the GCMC particle insertion/deletion rule and takes the form

$$\begin{aligned} acc((N_A+1,N_B-1) \leftarrow (N_A,N_B)) &= \min\left[1, \frac{p(N_A+1,N_B-1)}{p(N_A,N_B)}\right]; \\ \frac{p(N_A+1,N_B-1)}{p(N_A,N_B)} &= \frac{N_B V_A}{(N_A+1)V_B} \times e^{-\beta(\Delta E_A+\Delta E_B)} \end{aligned} \tag{3.10}$$

and thus the basic GEMC method is complete. In the implementation of both GCMC and GEMC in this work, the MCCCS Towhee package from Sandia National Labs is used [28].

Chapter 4

Binary hard-sphere fluid at a hard wall

In this chapter, simulation details, system details, and results from molecular-dynamics (MD) simulation of a number of binary hard-sphere fluids at a structureless hard wall are discussed. The mixtures are characterized by the ratio of the diameters of the two sphere types, the composition (mole fractions) within the mixture, and packing fraction of the fluid. Equations for pressure P, chemical potentials μ_i, and interfacial free energy γ are derived from the White Bear II (WBII) theory free-energy density Φ for binary mixtures. Values of γ are determined using an extension of Gibbs-Cahn Integration to a multicomponent fluid [29–33]. Agreement between MD results and the WBII theory predictions is generally great, with significant deviations occuring at only the highest packing fractions [34].

4.1 Introduction

The interfacial free energy γ is the primary property governing the thermodynamics of solid-liquid interfaces. For chemically heterogeneous interfaces, in which the solid and liquid have a large difference in composition, an important reference system is the hard-sphere (HS) fluid confined at a structureless hard wall (HW). The simple, but non-trivial, nature of such systems is well suited for the evaluation and development of theories for inhomogeneous fluids, especially integral-equation methods or classical density-functional theories (cDFT). In addition, some real polymer and colloid systems can be modeled quantitatively as hard-spheres. One example is that poly-*N*-isopropylacrylamide (PNIPAM) spheres in a solvent with appropriate charge screening reproduce results from previous calculations on the pure HS system [35]. There has been considerable theoretical and computational work focused on the HS/HW system; however, the vast majority of such studies have focused on single-component HS fluids, with significantly less work examining confined multi-component HS fluids. In this work, we examine the interfacial thermodynamics of a binary hard-sphere fluid at a structureless hard wall using molecular-dynamics simulation. The need for highly accurate molecular-dynamics (MD) results for hard-sphere systems is two-fold. First, these results provide physical insight into the fundamental material properties of systems in which the interactions are nearly entirely repulsive. Second, these results, when compared to theoretical predictions from cDFT, for example, can demonstrate where the theory can be refined for better accuracy.

Density-functional theory (DFT) is a powerful approach for predicting thermodynamic quantities of a system by considering them as functionals of the equilibrium single-particle density $\rho_0(\mathbf{r})$. While DFT was originally proposed for quantum-mechanical systems by Hohenberg and Kohn [36], it has since been generalized to classical fluids [37]. The extension of DFT to classical systems, cDFT, is an approach capable of predicting bulk and interfacial structure, thermodynamics, and phase transitions using $\rho(\mathbf{r})$. By minimizing a free energy functional Ω with respect to particle density, $\partial\Omega/\partial\rho_0(\mathbf{r}) = 0$, fluid properties of interest corresponding to $\rho_0(\mathbf{r})$ can be derived. Fundamental-Measure Theory (FMT) is a successful theory for treating mixtures within cDFT. Originally, Rosenfeld used the Percus–Yevick (PY) equation of state as the underlying description of a bulk fluid to determine a free-energy density functional. Since then, FMT has been improved by using more accurate bulk fluid equations of state to determine the functional [38]. FMT has been used in previous studies as a comparison with hard-sphere thermodynamics values calculated using molecular dynamics.

Although theoretical estimates from Scaled Particle Theory (SPT) have been in existence since the 1960s [39, 40], the first simulations to calculate γ for a single component HS/HW system were those of Henderson and Van Swol [41], who obtained γ by integrating the excess surface stress obtained from molecular-dynamics simulation. Subsequently, a number of higher precision calculations were reported using thermodynamic integration (TI) [42–44]. Mechanical methods [45] can also be used, but require considerable computational effort in order to achieve acceptable precision. Laird and Davidchack used the cleaving-wall method

[46] and Gibbs-Cahn Integration [29, 30] to obtain very high precision results for this system that are useful in evaluating theoretical predictions, such as that from SPT [39] and recent cDFT results from FMT [47] and its extensions [38, 48].

There have been a number of cDFT studies of the structure and interfacial thermodynamics of the binary HS/hard wall system [38, 48–51]. FMT has been shown to accurately describe inhomogeneous hard-sphere fluids, including structure, excess adsorption and interfacial free energy at a planar hard wall. By basing new density functionals on more accurate equations of state, the performance of FMT is improved. Other developments in FMT are based on changing the relation between the geometric weighted densities and the free-energy density functional [38]. Curiously, the most noticeable (though still minor) discrepancies between FMT and MD occur for pure HS systems at high densities and mixtures with significant size asymmetries [51]. Simulation studies on HS mixtures have unfortunately been limited to evaluations of structure through the calculation of density profiles [52, 53]. This has made it difficult to quantitatively evaluate the thermodynamic predictions of the theoretical studies. In this work, we present results from molecular-dynamics simulation for the interfacial thermodynamics of a variety of binary hard-sphere fluids at a structureless hard wall. In these simulations, the interfacial free energy γ is determined using an extension of the Gibbs-Cahn Integration [29–33] technique to a multicomponent fluid at a static, structureless solid wall. The results are compared to recent results based on the White Bear II (WBII) cDFT [38, 51].

4.2 System

The system of interest is a binary hard-sphere fluid mixture confined in a slit-pore geometry (i.e., between two planar hard walls). The interparticle and wall-particle potentials ϕ and ϕ_w are

$$\phi(r) = \begin{cases} \infty & r < \sigma_{ij} \\ 0 & r \geq \sigma_{ij} \end{cases} \tag{4.1}$$

$$\text{and} \quad \phi_w(z) = \begin{cases} \infty & z < \sigma_i/2 \\ 0 & z \geq \sigma_i/2 \end{cases} \tag{4.2}$$

where σ_i is the diameter of spheres of type $i \in \{1,2\}$, σ_{ij} is the arithmetic mean of σ_i and σ_j, r the distance between the centers of two spheres, and z the distance between sphere center and wall. Defined in this manner, the sphere-wall collision occurs at the surface of the sphere, not the center.

The system consists of N_1 type 1 spheres with diameter σ_1 and N_2 type 2 spheres with diameter σ_2 in a volume V, giving a total number density ρ of

$$\rho = \frac{N_1 + N_2}{V} = \rho_1 + \rho_2 \tag{4.3}$$

where ρ_i is the number density of species i. Without loss of generality, $\sigma_1 > \sigma_2$ is assumed. The mole fraction of each species is $x_i = \rho_i/\rho$, with $x_1 + x_2 = 1$. The total packing fraction η for the mixture is $\eta = \eta_1 + \eta_2$, where $\eta_i = \frac{\pi}{6}\sigma_i^3\rho_i$. For a given α, the system is completely described by specifying x_1 and η. This is in

contrast with a pure system, in which case one needs only to use η to completely define the system.

4.3 Gibbs-Cahn Integration

In this work, the mixture-wall interfacial free energy is calculated from MD simulations using the Gibbs-Cahn Integration method, which is based on Cahn's extension [54] of the surface thermodynamics of Gibbs [55]. This method has been applied to the calculation of γ for one- and two-component crystal-melt interfaces [31–33] and for single-component fluids at static walls [29, 30], where it was shown to have considerably less computational overhead than competing methods without sacrificing precision. The derivation of the Gibbs-Cahn adsorption equation specifically for a fluid at a static wall is discussed in Ref. [29] and is outlined here. Consider an r-component fluid at a static surface. The total Gibbs free energy G for this system is

$$G = E - TS + PV \tag{4.4}$$

where E, T, S, and P are the internal energy, temperature, entropy, and pressure, respectively. The Gibbs free energy of the bulk fluid G^{f} is

$$G^{\mathrm{f}} = \sum_{i=1}^{r} \mu_i N_i \tag{4.5}$$

where μ_i is the chemical potential of species i and superscript "f" denotes bulk fluid quantities. The interfacial free energy is defined as the difference per unit

area between the free energy of the fluid at the interface and the bulk fluid.

$$\gamma A = G - G^{\mathrm{f}} = E - TS + PV - \sum_{i=1}^{r} \mu_i N_i \tag{4.6}$$

where A is the interfacial area. The differential of this quantity is

$$d(\gamma A) = -SdT + VdP - \sum_{i=1}^{r} N_i d\mu_i \tag{4.7}$$

This equation and the Gibbs-Duhem equation for the bulk fluid

$$-S^{\mathrm{f}} dT + V^{\mathrm{f}} dP - \sum_{i=1}^{r} N_i^{\mathrm{f}} d\mu_i = 0 \tag{4.8}$$

then form a system of two simultaneous linear equations connecting the differentials. Cramer's rule from linear algebra can then be used to eliminate one of the differential terms on the right-hand side of Eq. 4.7, giving

$$A\, d\gamma = -[S/X]\, dT + [V/X]\, dP - \sum_{i=1}^{r} [N_i/X]\, d\mu_i \tag{4.9}$$

where X can be any variable conjugate to a differential dx in Eq. 4.9 and the notation $[Y/X]$ is defined as

$$[Y/X] \equiv \frac{1}{X^{\mathrm{f}}} \begin{vmatrix} Y & X \\ Y^{\mathrm{f}} & X^{\mathrm{f}} \end{vmatrix} \tag{4.10}$$

In Eq. 4.10, the quantities with superscript "f" are measured in a region of the system far enough away from the interface to be considered bulk fluid, whereas the unscripted quantities are measured in a region that wholly encompasses the interface and associated interfacial fluid. The form of Eqs. 4.9 and 4.10 ensures that one of the $[Y/X]\,dx$ terms in Eq. 4.9 can be eliminated by setting $X = Y$.

For a hard-sphere system, such as the one studied here, the temperature dependence of γ is a trivial linear scaling [56], so the dT term in Eq. 4.9 can be neglected. Thus, for a binary (two-component) hard-sphere fluid at a hard wall, the Gibbs-Cahn adsorption equation (Eq. 4.9) becomes

$$A\,d\gamma = [V/X]\,dP - [N_1/X]\,d\mu_1 - [N_2/X]\,d\mu_2 \tag{4.11}$$

The application of Eq. 4.11 requires a specific choice for X, which is equivalent to defining a Gibbs Dividing Surface (GDS) [57] such that the excess surface value of the quantity X is zero. For example, one possible choice is $X = N_1$ yielding

$$\begin{aligned} d\gamma &= \frac{1}{A}[V/N_1]\,dP - \frac{1}{A}[N_2/N_1]\,d\mu_2 \\ &= v_{N_1}\,dP - \Gamma_{2|N_1}\,d\mu_2 \end{aligned} \tag{4.12}$$

where v_{N_1} and $\Gamma_{2|N_1}$ are the excess volume and excess number of type 2 particles per unit volume using a GDS defined such that the surface excess number of type 1 particles is zero. Similarly, one can choose $X = N_2$ or V; however, for this study, it was found most convenient to choose X to be the total particle number,

$N = N_1 + N_2$. To do this, Eq. 4.7 for the binary hard-sphere system is rewritten as

$$\begin{aligned} A\,d\gamma &= V\,dP - N_1 d\mu_1 - N_2 d\mu_2 \\ &= V\,dP - N_1 d(\mu_1 - \mu_2) - N d\mu_2 \\ &= V\,dP - N_1 d\Delta\mu - N d\mu_2 \end{aligned} \tag{4.13}$$

where $\Delta\mu = \mu_1 - \mu_2$. Equation 4.11 then becomes

$$A\,d\gamma = [V/X]\,dP - [N_1/X]\,d\Delta\mu - [N/X]\,d\mu_2 \tag{4.14}$$

Setting $X = N$ then gives

$$d\gamma = v_N\,dP - \Gamma_{1|N}\,d\Delta\mu \tag{4.15}$$

where v_N and $\Gamma_{1|N}$ are the excess V and excess N_1 for a GDS defined such that the excess total number of particles is zero. The choice of $X = N$ was used in the current work because it gives significantly smaller statistical error than the other possible choices for similar computational effort, and the value of $\Delta\mu$ can be calculated easily using a particle-swap method.

We calculate γ by integrating Eq. 4.15 with respect to pressure at fixed x_1, recognizing that $\gamma(P = 0) = 0$. The resulting expression can be written as

$$\gamma(P;x_1) = \int_0^P \left[v_N(P';x_1) - \Gamma_{1|N} \left(\frac{d\Delta\mu}{dP'} \right)_{x_1} \right] dP' \tag{4.16}$$

In this work, we evaluate this integral numerically at fixed x_1 as a function of η for the system, as identity and number of particles are far easier to control than pressure and $\Delta\mu$. We use reduced units throughout with energy and length scales of kT and σ_1, respectively, giving the following reduced quantities: $\rho_i^* = \rho_i\sigma_1^3$, $\gamma^* = \gamma\sigma_1^2/k_BT, P^* = P\sigma_1^3/k_BT, v_N^* = v_N/\sigma_1, \Gamma_{1|N}^* = \Gamma_{1|N}\sigma^2$ and $\mu_i^* = \mu_i/k_BT$. For simplicity, in what follows, the "*" superscript is omitted and all quantities are assumed to be in reduced units, unless otherwise specified.

4.4 Simulation details

Molecular-dynamics simulations are performed on a HS mixture between two structureless hard walls in a slit-pore geometry. The MD simulations were implemented using the linked-cell-list algorithm of Rapaport [7]. The spheres are initialized in a face-centered cubic (fcc) crystal with the lattice constant based on the desired mole fraction x and packing fraction η. The size of the simulation box is fixed at approximately $L_x \times L_y \times L_z = 33\sigma_1 \times 33\sigma_1 \times 38\sigma_1$ for most systems; at higher packing practions, the volume is reduced such that the total number of spheres does not exceed 50000. The z-axis is defined as being normal to the walls, and periodic boundary conditions are employed in the x and y directions. The distance between the walls (L_z) is chosen such that there is a significant bulk fluid in the center of the simulation box. Diameter ratios of $\alpha = 0.7, 0.8, 0.9$ were chosen for this study, as the phase diagrams in this range of α are well characterized [58–60]. For each α, we examined systems of mole fraction $x_1 = 0.25, 0.50, 0.75$ in the range $\eta < 0.5$.

This range of η was chosen because it corresponds to the fluid region of the phase diagrams.

Each system equilibrates for $1000\,\tau$, where $\tau = \sigma_1\sqrt{m/k_BT}$ is the natural time unit for hard-sphere dynamics. Equilibrium averages of P, $\Delta\mu$ and the individual density profiles, $\rho_1(z)$ and $\rho_2(z)$, are collected for each system studied over a total time of $20\,000\,\tau$, divided into 20 blocks of $1000\,\tau$ each. Bulk values such as density and mole fraction are determined by averaging over the bulk region. Using the density profiles, we determined that defining the bulk region to consist of all particles more than $7\sigma_1$ away from either wall was sufficient for all systems studied. Pressures are calculated using the equation

$$\beta P = \rho^{\mathrm{f}} + \frac{1}{3V^{\mathrm{f}}\Delta\tau}\left\langle \sum \vec{r}_{ij}\cdot\vec{v}_{ij}\right\rangle \tag{4.17}$$

where $\beta = 1/k_BT$, V^{f} is the volume of the bulk region, $\Delta\tau$ is the time over which collisions are summed in the bulk fluid, $\vec{r}_{ij}$ is the vector between the centers of two spheres upon collision, and $\vec{v}_{ij}$ is the difference of the velocities of two spheres upon collision. Fig. 4.1 shows examples of the density profiles calculated for $\alpha = 0.9$ at a reduced pressure of 1.6627 and a mole fraction of $x_1 = 0.25$.

The chemical potential difference ($\Delta\mu$) is calculated in a manner similar to the Widom insertion method [61], in which individual chemical potentials (μ_i) are calculated by inserting test particles into the system. To calculate $\Delta\mu$, the Widom insertion method is modified by replacing particle insertions with particle swaps [62, 63]. The advantage of the particle swap method is that it determines

$\Delta\mu$ directly, without the need to separately calculate the individual μ_i, which is difficult at large η. Dividing $\Delta\mu$ into an ideal-solution component and an excess component yields

$$\Delta\mu = \Delta\mu_{\text{ideal}} + \Delta\mu_{\text{excess}} \tag{4.18}$$

where

$$\Delta\mu_{\text{ideal}} = \ln\left(\frac{x_1}{1-x_1}\right) \tag{4.19}$$

and, for the hard-sphere binary system, the excess component is given by

$$\Delta\mu_{\text{excess}} = \ln\left[\frac{\mathscr{P}(\sigma_{2\leftarrow 1})}{\mathscr{P}(\sigma_{1\leftarrow 2})}\right] \tag{4.20}$$

where $\mathscr{P}(\sigma_{j\leftarrow i})$ is the probability that changing the identity of a randomly chosen particle from type i to type j will not result in a particle overlap. [Note: for the hard-sphere mixtures considered here, $\mathscr{P}(\sigma_{2\leftarrow 1})$ is identically 1.]

The values of v_N and $\Gamma_{1|N}$ as functions of pressure (or η) are calculated by numerically integrating their representations as integrals over the density profiles:

$$v_N(P) = \int_0^\infty \left[1 - \frac{\rho(z;P)}{\rho^{\text{f}}(P)}\right] dz \tag{4.21}$$

$$\Gamma_{1|N}(P) = \int_0^\infty \left[\rho_1(z,P) - x_1^{\text{f}}(P)\rho(z,P)\right] dz \tag{4.22}$$

Because the density profiles approach step functions in the low density (pressure) limit, the values of $v_N(P=0)$ and $\Gamma_{1|N}(P=0)$ can be determined analytically to

be $[x_1 + \alpha(1-x_1)]/2$ and 0, respectively. Examples of the density profiles in the zero-pressure limit are shown in Fig. 4.1.

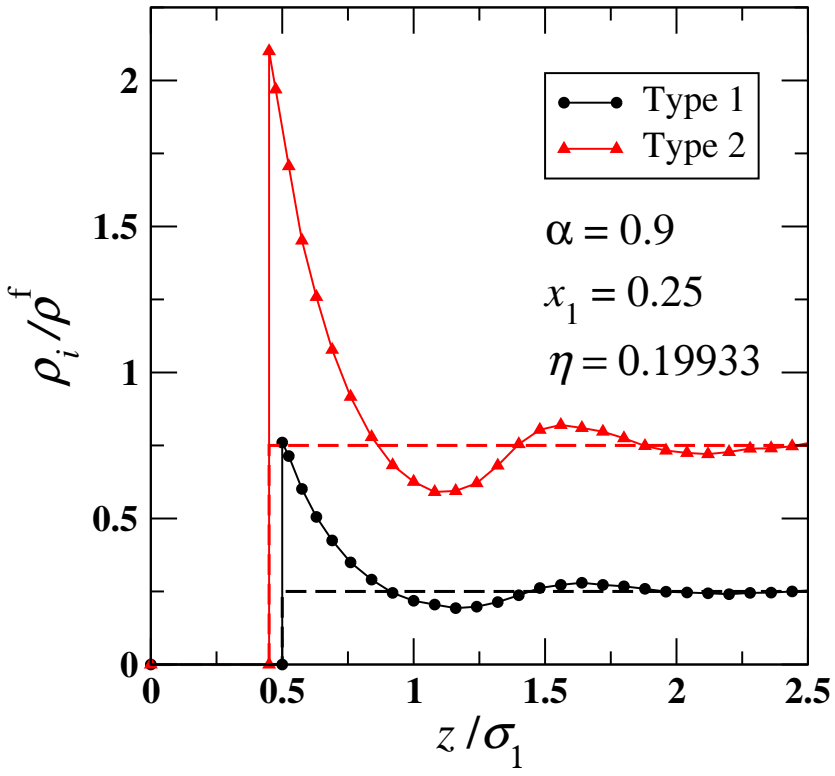

Figure 4.1: Sample density profiles for a mixture at a hard wall. The mixture has diameter ratio $\alpha = 0.9$, mole fraction $x_1 = 0.25$, and packing fraction $\eta = 0.19933$. Zero-pressure (ideal) limits are given by the dashed lines.

4.5 Results

For each of the diameter ratios studied here ($\alpha = 0.7, 0.8$ and 0.9), the system is examined at mole fractions x_1 = 0.25, 0.50 and 0.75, each for packing fractions

in the range $\eta < 0.5$. This range of η was chosen because it corresponds approximately to the fluid region of the phase diagrams [58–60], in order to avoid the freezing transition. Because of differential adsorption of one species over the other at the interface, the mole fraction and density of the bulk fluid region can change slightly from that of the initial configuration as the system equilibrates. Before taking averages, particles of the requisite type are added, removed, or swapped to ensure that the relative deviations from the desired bulk values are less than 10^{-4} in the final equilibrated system.

The observed pressures in the simulation are in good agreement with pressure values obtained using both the Mansoori-Carnahan-Starling-Leland (MCSL) equation of state [64] or the more accurate Carnahan-Starling mark III (CSIII) equation of state [38] for HS mixtures. Calculated pressures from the MD simulations are plotted with the CSIII predictions, along with the percent deviation between the two methods, in Figs. 4.2–4.4. Percent deviation is determined using the expression $(P_{MD} - P_{CSIII})/P_{CSIII} \times 100\%$. The agreement between the two methods is excellent, within 0.4% for all systems studied here. The maximum deviation is seen near $\eta = 0.35 - 0.4$ for all systems. For each diameter ratio, the shapes of the curves for the three mole fractions are very similar to one another. This suggests that a proposed correction term to the CSIII equation of state might reasonably be treated as independent of mole fraction. For greater size mismatch (lower α), increased negative deviation in the low-density regime is observed. Above $\eta = 0.4$, the measured deviations no longer vary smoothly, which may prompt need for higher-precision simulations to be performed in the future.

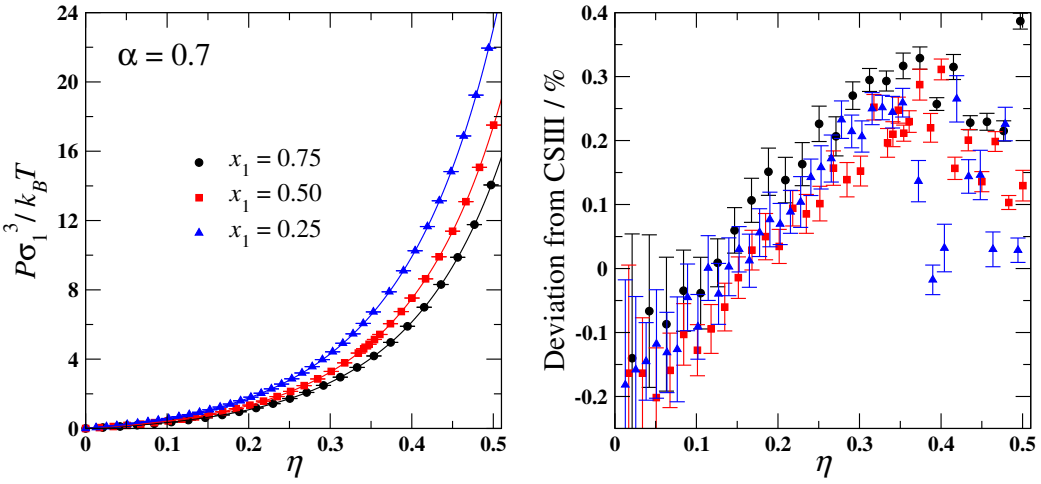

Figure 4.2: Pressure summary for the $\alpha = 0.7$ hard-sphere mixtures at three mole fractions. The symbols are the MD results, and the solid lines are the CSIII equation of state.

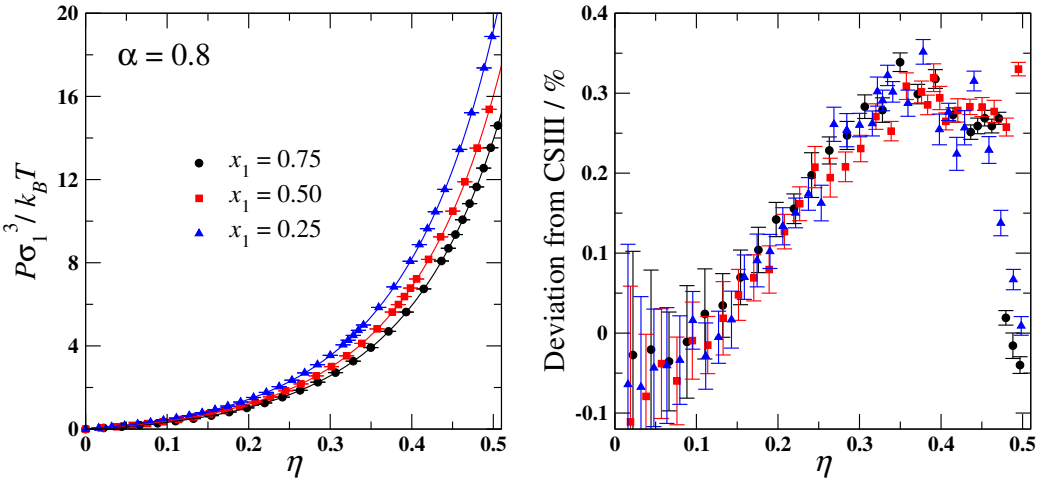

Figure 4.3: Pressure summary for the $\alpha = 0.8$ hard-sphere mixtures at three mole fractions. The symbols are the MD results, and the solid lines are the CSIII equation of state.

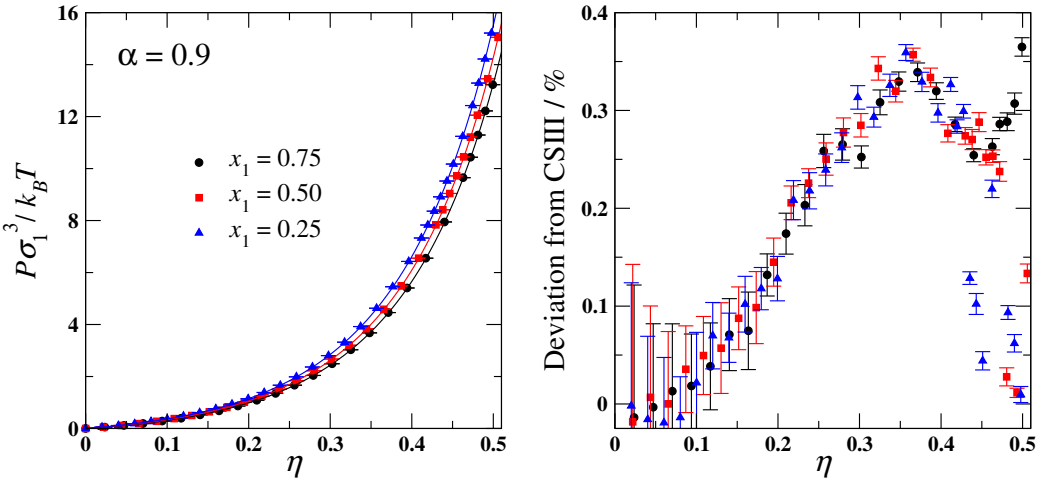

Figure 4.4: Pressure summary for the $\alpha = 0.9$ hard-sphere mixtures at three mole fractions. The symbols are the MD results, and the solid lines are the CSIII equation of state.

The observed chemical potential differences are in good agreement with the approximate WBII predictions (derived in Appendix A.1). Calculated and predicted chemical potentials, along with percent deviation, are shown in Figs. 4.5–4.7. Percent deviation is determined using the expression $(\Delta\mu^{ex}_{MD} - \Delta\mu^{ex}_{WBII})/\Delta\mu^{ex}_{WBII} \times 100\%$. The ideal-solution component is removed because it contributes identically to the predicted and measured values, and this also allows the deviation to be calculated without potential sign changes in the denominator across the range of packing fractions.

The maximum deviation is seen as η approaches 0, where $\Delta\mu^{ex}$ approaches 0. As η increases, this positive deviation decays rapidly until it becomes approximately 0 near $\eta = 0.2$. For $\alpha = 0.9$ and all x_1, great agreement is seen for all $\eta > 0.2$, as is the case with $\alpha = 0.7, 0.8$ and $x_1 = 0.50, 0.75$. However, a strange

feature is observed for $\alpha = 0.7, 0.8$ and $x_1 = 0.25$ at high η. A discontinuity is introduced as a sudden negative deviation of around -5% and -2% for the 0.7 and 0.8 diameter ratios, respectively. This would seem to indicate that a phase change of some sort has occurred for these systems, although no evidence of this is observed in the density profiles.

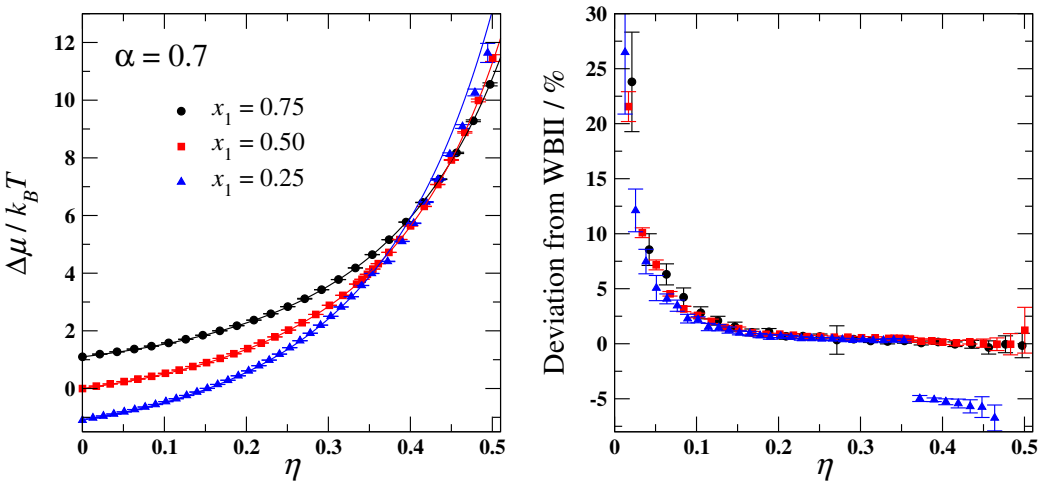

Figure 4.5: Chemical potential summary for the $\alpha = 0.7$ hard-sphere mixtures at the three mole fractions. The symbols are the MD results, and the solid lines are the approximate predictions from the WBII bulk theory.

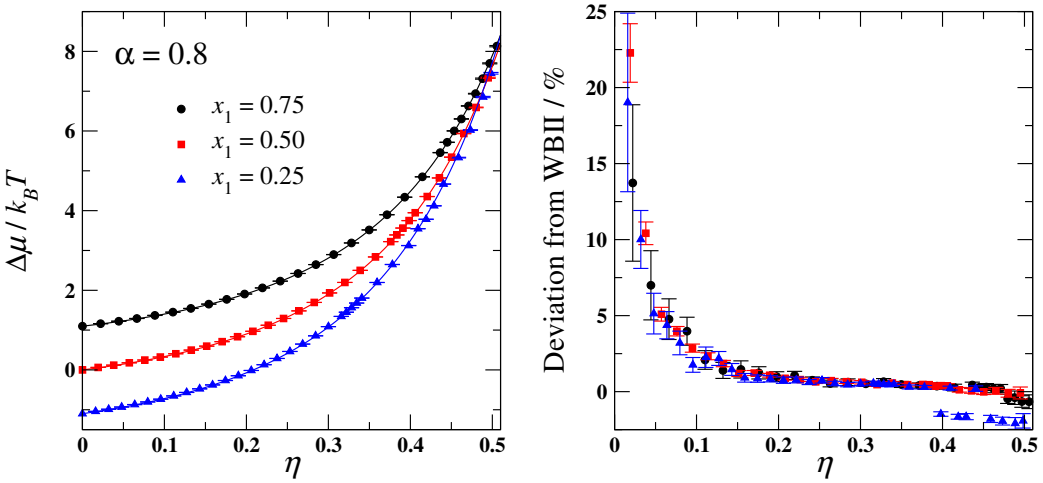

Figure 4.6: Chemical potential summary for the $\alpha = 0.8$ hard-sphere mixtures at the three mole fractions. The symbols are the MD results, and the solid lines are the approximate predictions from the WBII bulk theory.

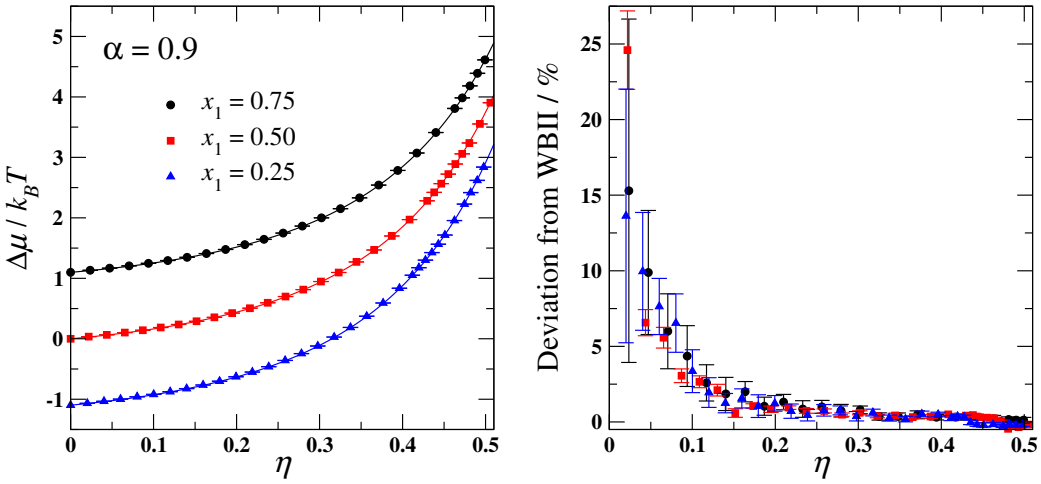

Figure 4.7: Chemical potential summary for the $\alpha = 0.9$ hard-sphere mixtures at the three mole fractions. The symbols are the MD results, and the solid lines are the approximate predictions from the WBII bulk theory.

Figures 4.8–4.10 show the results for the excess volume, v_N, for $\alpha = 0.7, 0.8$ and 0.9, respectively. For comparison, the excess volume as determined from the White Bear II bulk theory (Appendix A.1) is also shown. For low and intermediate packing fractions, the WBII expressions are in excellent agreement with the simulation results, although some deviation is seen at the highest packing fractions ($\eta > 0.45$). Interestingly, the deviations are seen primarily in the pure systems (x_1 = 0 or 1), although the deviations are present for $\alpha = 0.9$ and all three compositions. Because $\alpha = 0.9$ is a minor size mismatch, it is perhaps unsurprising that the WBII and MD results for $\alpha = 0.9$ systems suffer the same kinds of discrepancies as the pure HS fluids at high densities [51].

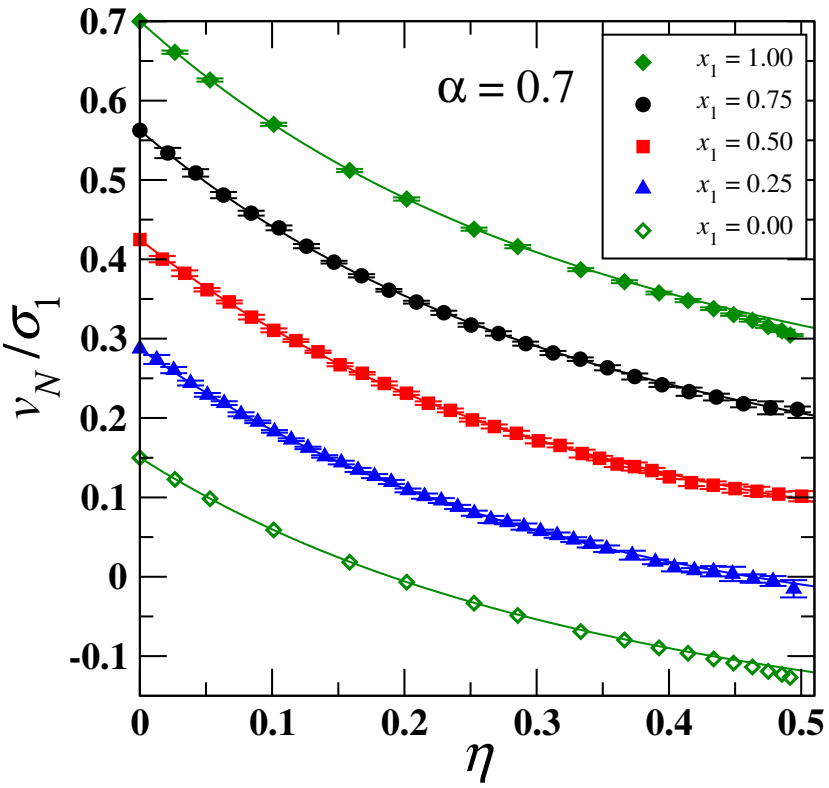

Figure 4.8: Excess volume per unit area, v_N, as a function of packing fraction for the $\alpha = 0.7$ mixtures. Results for the pure system (original and scaled) from Laird and Davidchack (Ref. [29]) are included as the diamond symbols. For clarity, the $x_1 = 1.00$ data has been shifted by $+0.2$ on the v_N-axis, the $x_1 = 0.75$ data by $+0.1$, the $x_1 = 0.25$ data by -0.1, and the $x_1 = 0.00$ data by -0.2. The solid lines are the predictions from the WBII bulk theory.

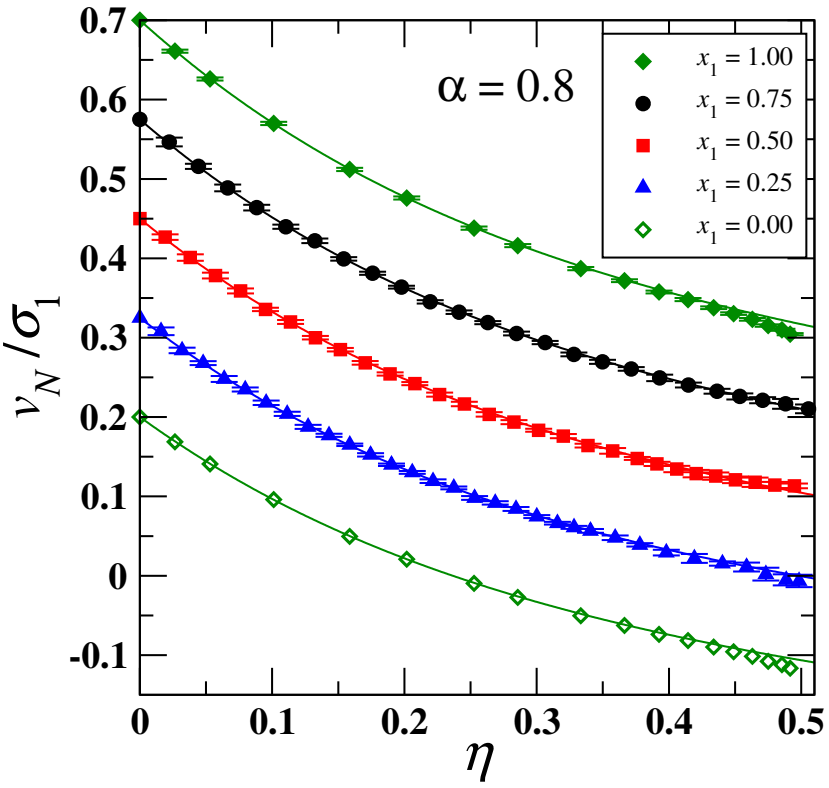

Figure 4.9: Excess volume per unit area, v_N, as a function of packing fraction for the $\alpha = 0.8$ mixtures. Same conventions as Fig. 4.8.

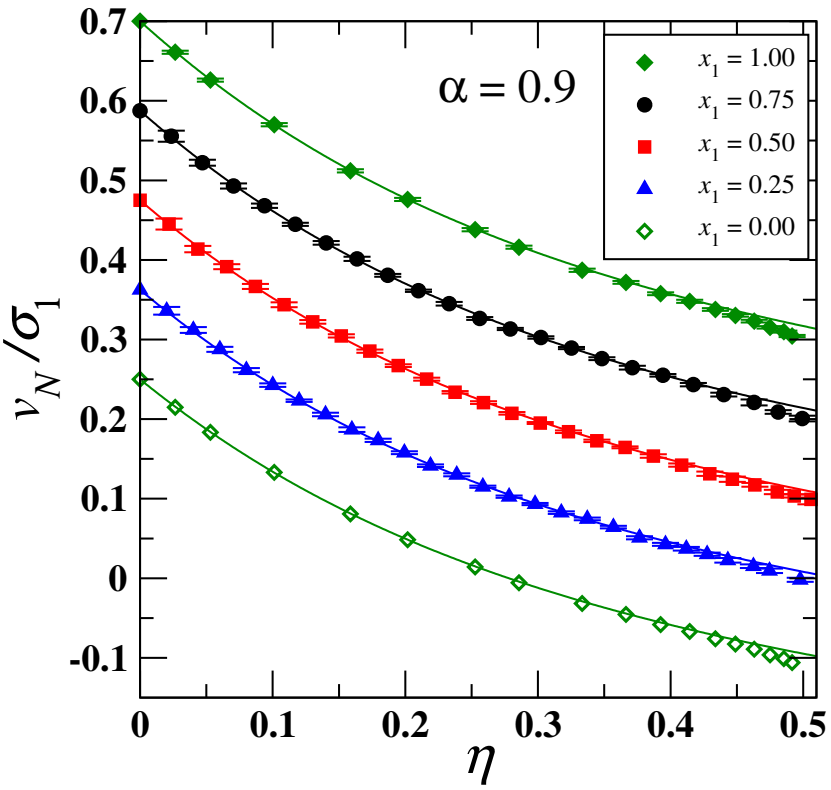

Figure 4.10: Excess volume per unit area, v_N, as a function of packing fraction for the $\alpha = 0.9$ mixtures. Same conventions as Fig. 4.8.

Because the excess adsorption $\Gamma_{1|N}$ for these systems is relatively small, it is difficult to get high relative precision for this quantity in reasonable simulation time. This is especially true at the higher packing fractions where the calculation of the $\Gamma_{1|N}$ involves numerical integration over highly oscillatory density profiles. The results for $\Gamma_{1|N}$ for $\alpha = 0.7, 0.8$ and 0.9 are shown in Figs. 4.11–4.13, respectively. Also shown in Figs. 4.11–4.13 are the corresponding predictions from WBII. Except at low packing fractions, the scatter in the data is large–due to the sampling issues discussed above–however, the contribution of $\Gamma_{1|N}$ to the value of γ through the integration of Eq. 4.16 is also quite small (Figs. 4.14–4.16), so the scatter in the $\Gamma_{1|N}$ data does not significantly affect the precision of the calculation of γ. At low packing fractions where the simulated $\Gamma_{1|N}$ is well converged, there is good agreement with the WBII expressions.

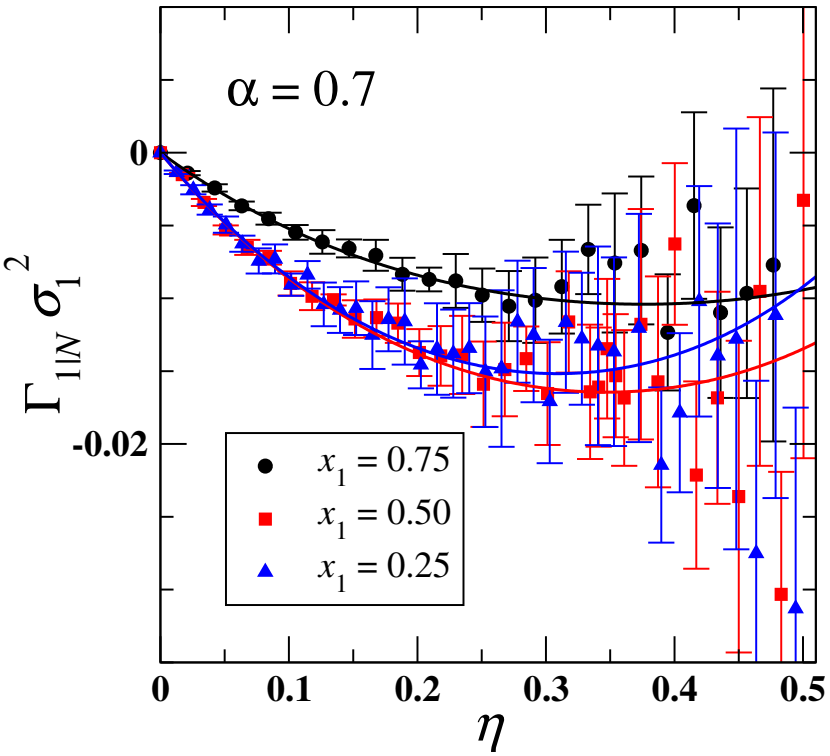

Figure 4.11: Interfacial excess particle number $\Gamma_{1|N}$ as a function of packing fraction for the $\alpha = 0.7$ systems. The corresponding predictions from the WBII bulk theory are shown as solid lines.

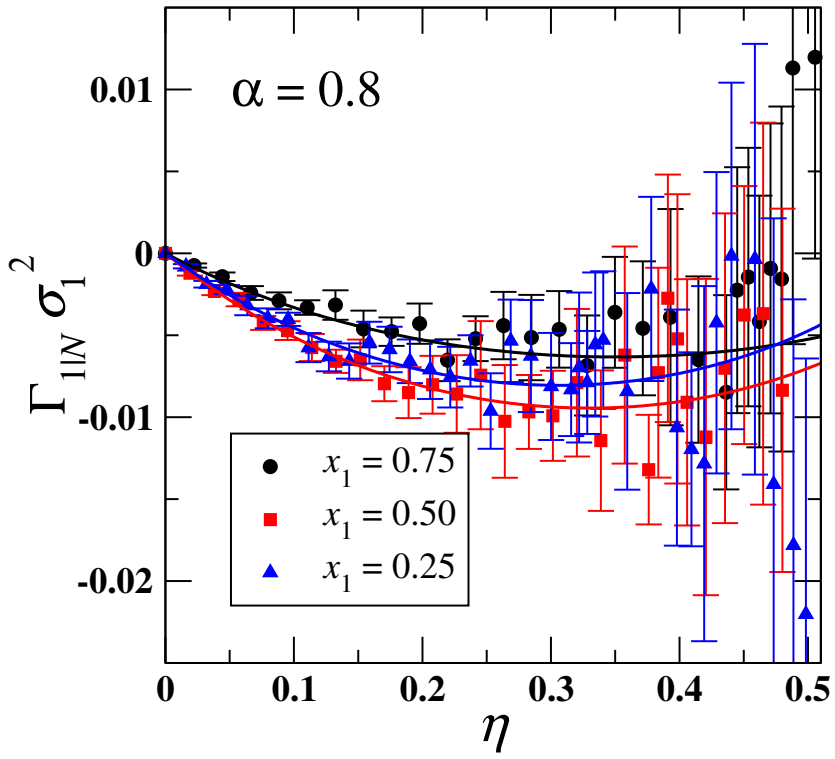

Figure 4.12: Same as Fig. 4.11, except for $\alpha = 0.8$.

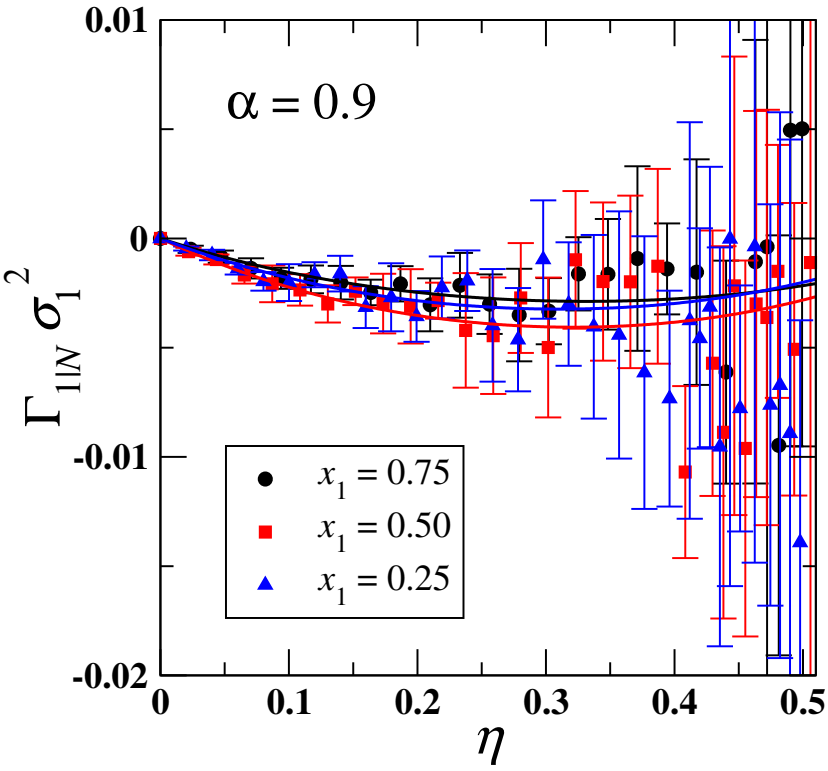

Figure 4.13: Same as Fig. 4.11, except for $\alpha = 0.9$.

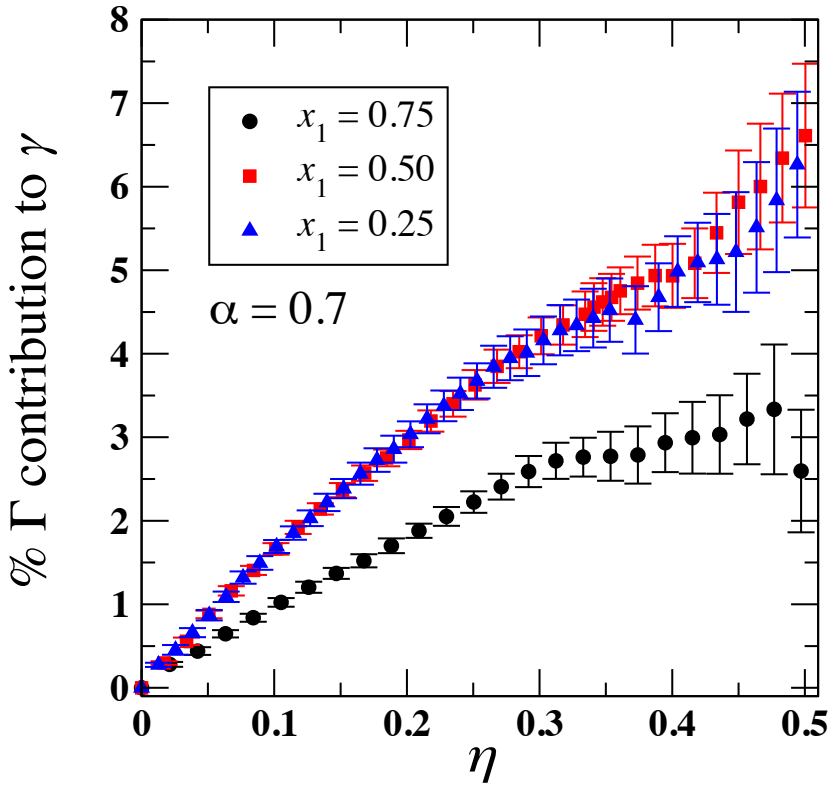

Figure 4.14: Excess adsorption contribution to γ for $\alpha = 0.7$ mixtures.

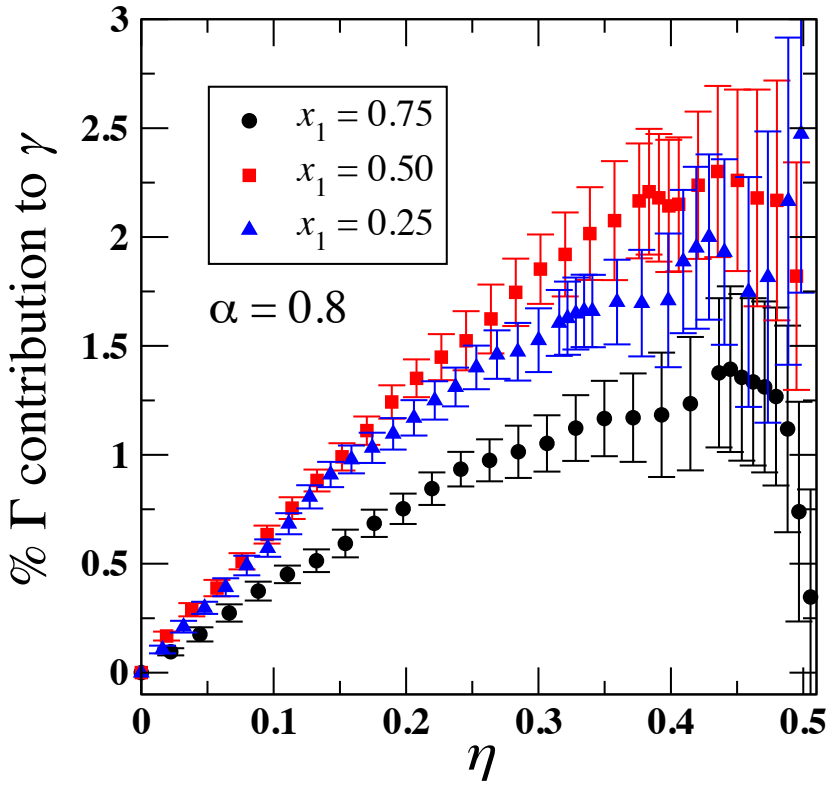

Figure 4.15: Excess adsorption contribution to γ for $\alpha = 0.8$ mixtures.

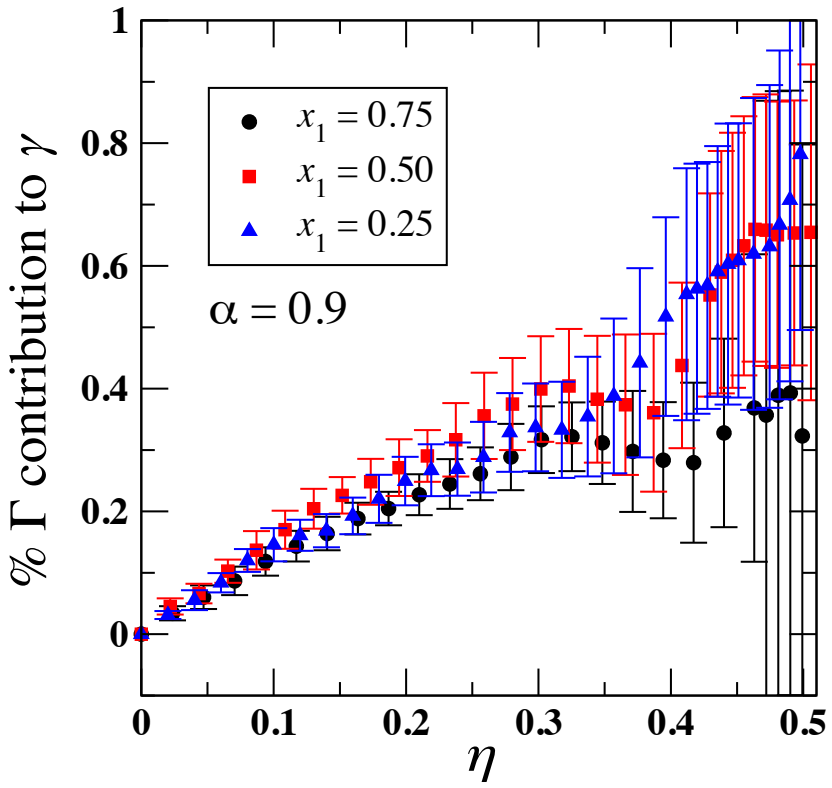

Figure 4.16: Excess adsorption contribution to γ for $\alpha = 0.9$ mixtures.

The interfacial free energy γ is then calculated from the data for v_N and $\Gamma_{1|N}$ by numerically integrating Eq. 4.16 using the trapezoid rule. Based on error analysis, the numerical error from the trapezoid rule is significantly smaller than the corresponding statistical error. The results for γ are plotted in Figs. 4.17–4.19. Also plotted in Figs. 4.17–4.19 are the predictions from the WBII bulk theory. The WBII predictions are in excellent agreement with the simulation data, except for overestimations at the highest packing fractions ($\eta > 0.45$).

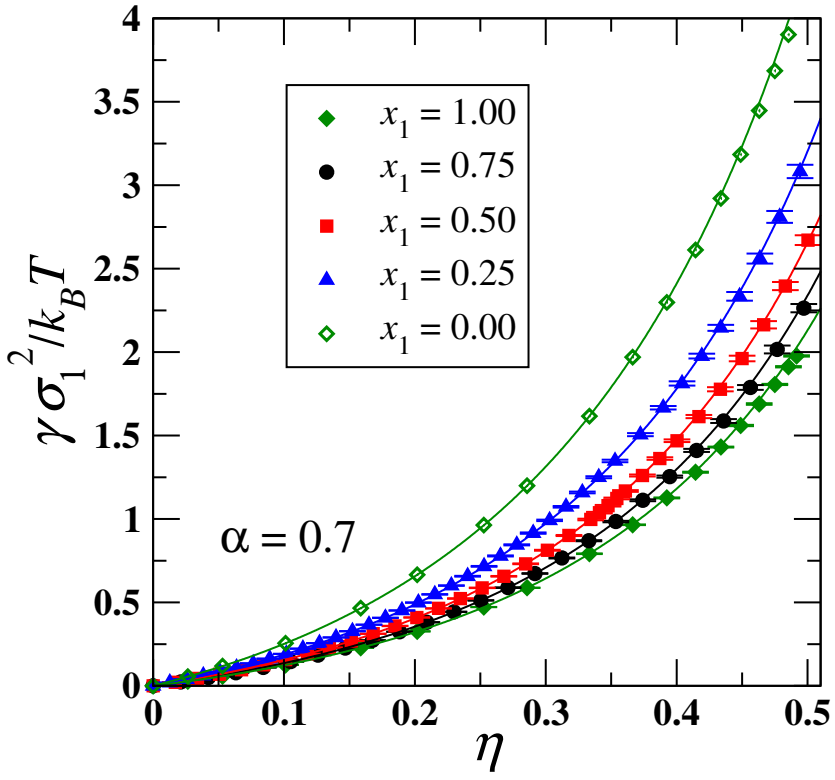

Figure 4.17: Interfacial free energy per unit area, γ, as a function of packing fraction for the $\alpha = 0.7$ mixtures. Results for the pure system from Laird and Davidchack [29] are included as the diamond symbols. Curves indicate γ_{WBII}. The inset is included to show better resolution at the higher pressures.

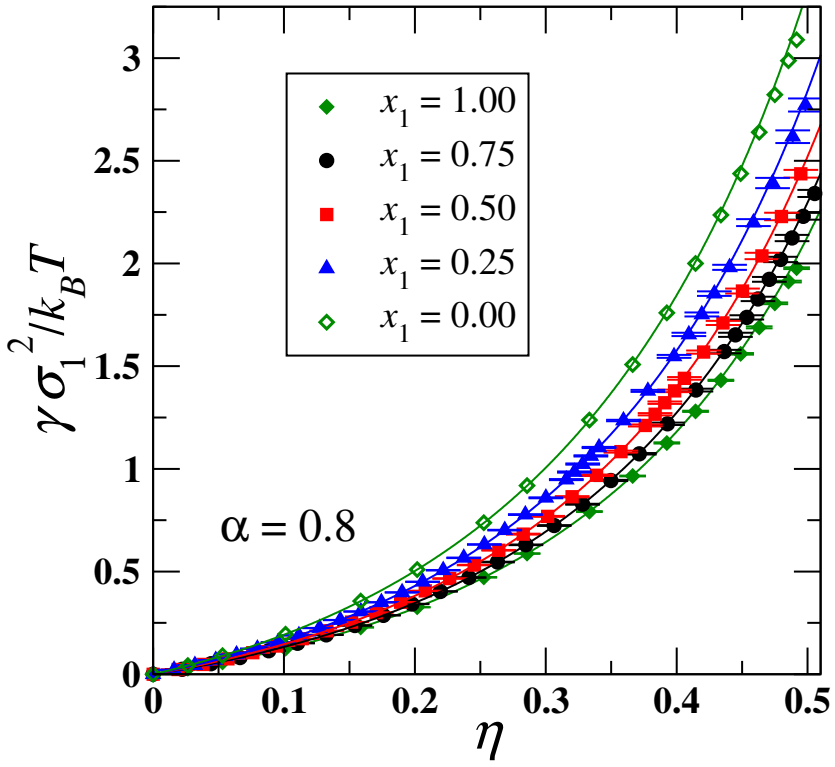

Figure 4.18: Same as Fig. 4.17, except for $\alpha = 0.8$.

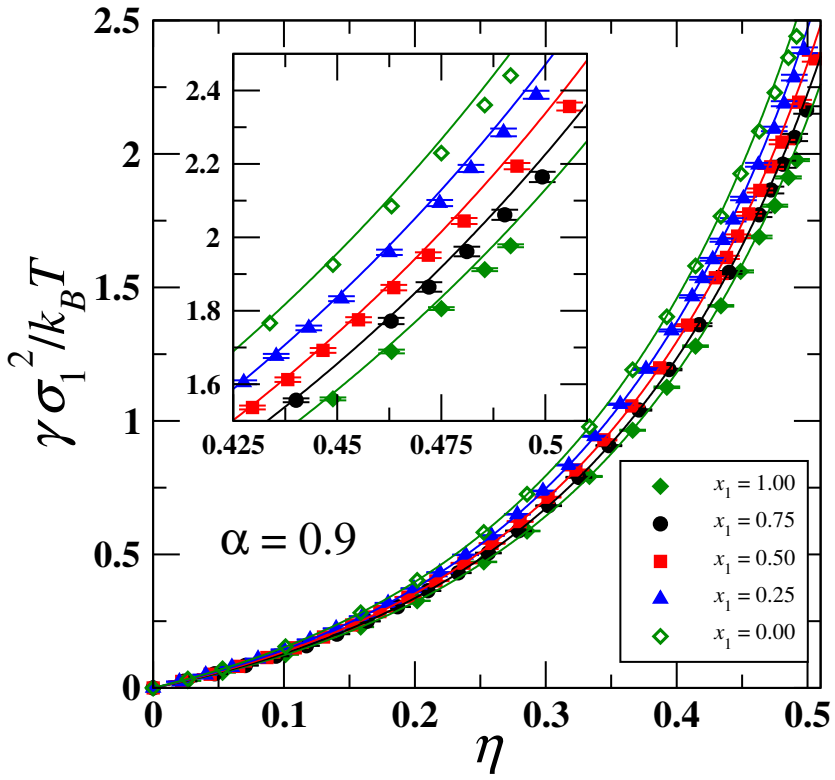

Figure 4.19: Same as Fig. 4.17, except for $\alpha = 0.9$.

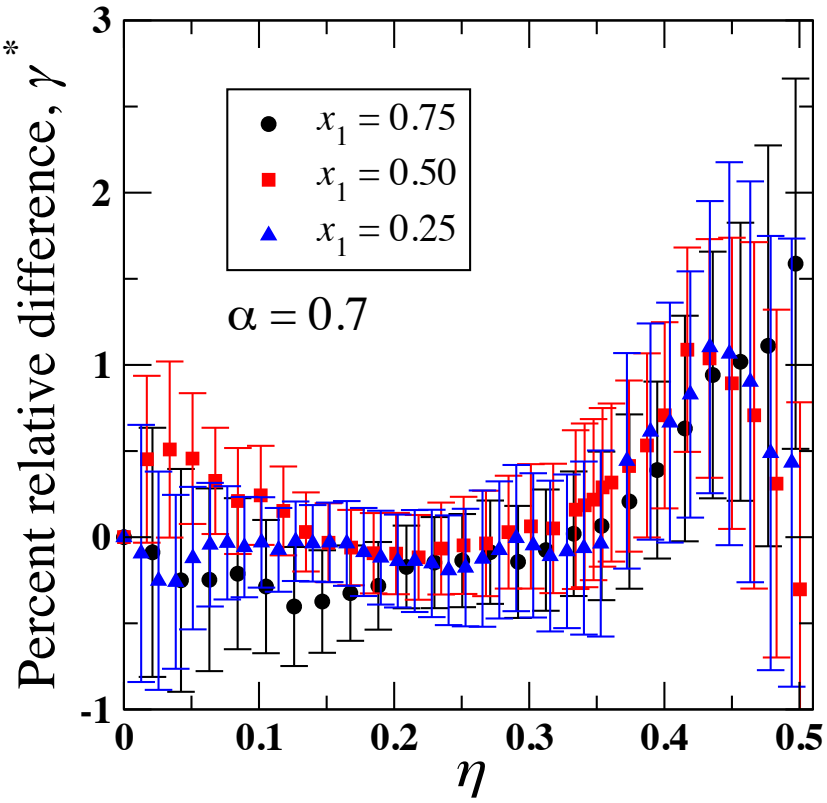

Figure 4.20: Percent relative difference between simulated values and WBII theory values for γ for the $\alpha = 0.7$ systems.

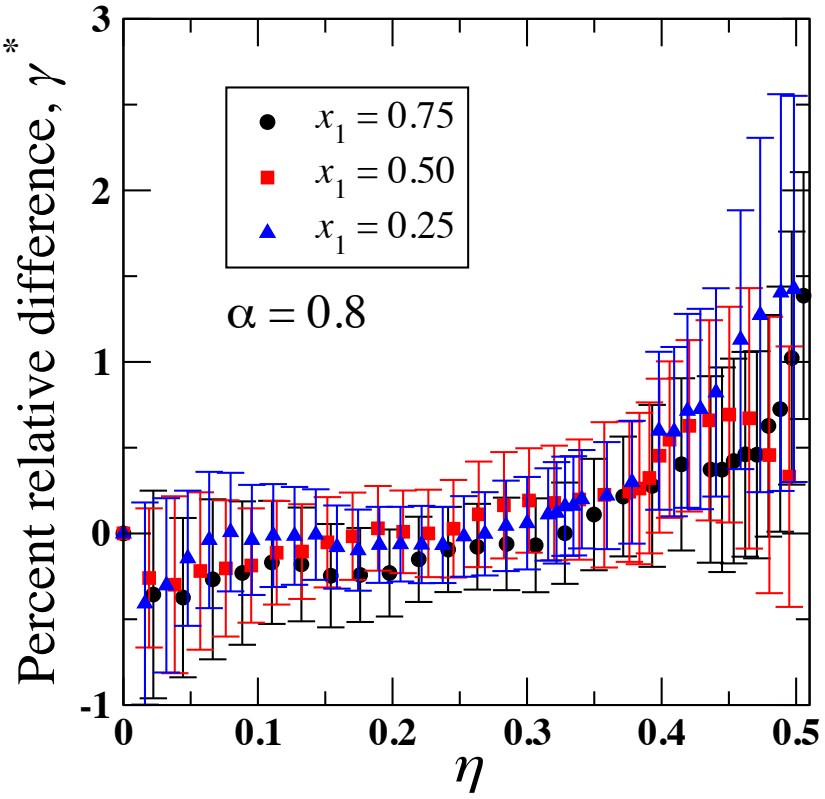

Figure 4.21: Percent relative difference between simulated values and WBII theory values for γ for the $\alpha = 0.8$ systems.

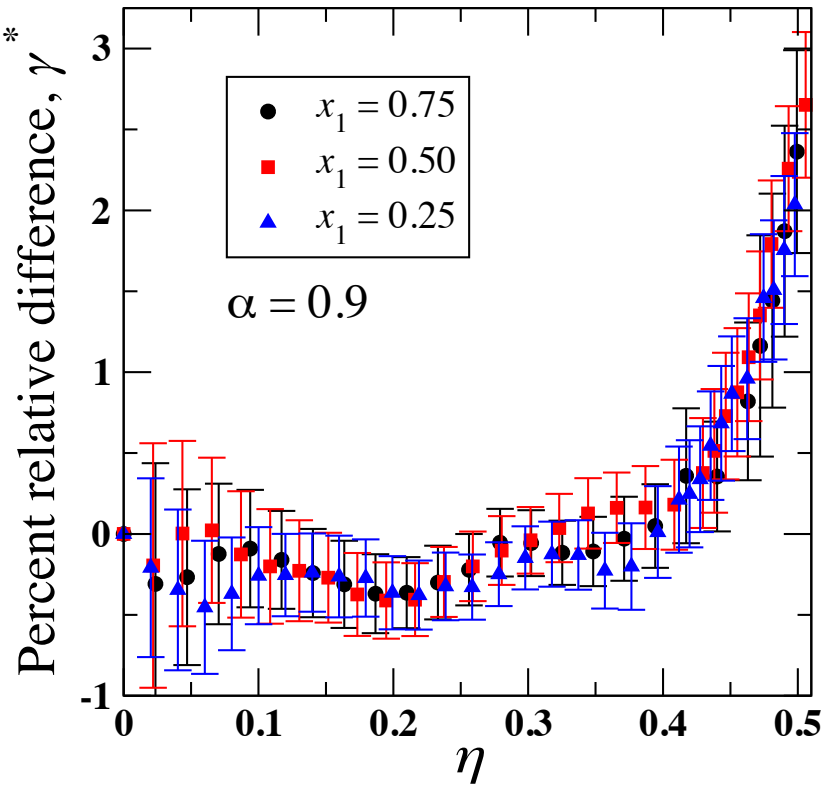

Figure 4.22: Percent relative difference between simulated values and WBII theory values for γ for the $\alpha = 0.9$ systems.

From the γ versus η data presented in Figs. 4.17–4.19, it is difficult to assess directly the dependence of γ on mole fraction. To better illustrate the composition dependence of the interfacial free energy, γ is shown as a function of composition (x_1) in Fig. 4.23 for selected fixed values of η. The corresponding plots for $\alpha = 0.8$ and 0.9 are shown in Figs. 4.24 and 4.25, respectively. The data for Figs. 4.23–4.25 were generated from the γ versus η data using quadratic interpolation (Appendix A.2). The simulation results show a significant negative deviation from linear dependence, which is well fit by the corresponding WBII results (also shown). The White Bear II theory predicts deviation from strict linear dependence, and we observe such deviation to a slightly greater extent than predicted. This deviation increases with increasing η and is maximum near $x_1 = 0.50$. One reason for the negative deviation from linear x_1 dependence might be that packing against the wall is enhanced by introducing particles of mismatched size. More efficient packing would decrease the value of v_N, and its contribution to γ would also decrease.

Tabulated results for the major findings of this work can be found in Appendix A.3.

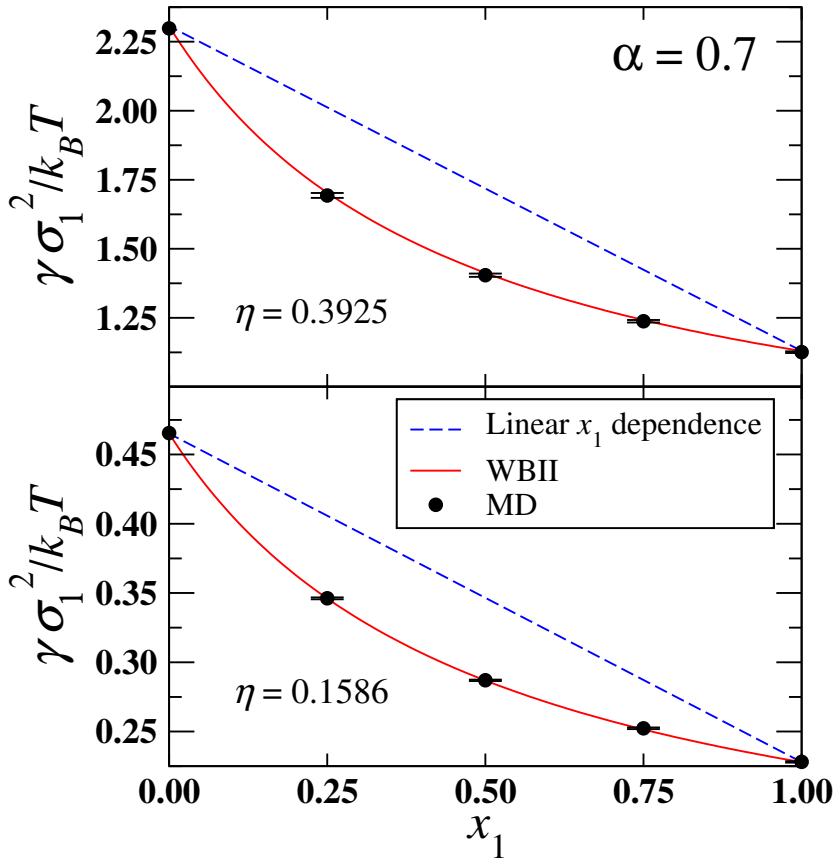

Figure 4.23: Interfacial free energy per unit area, γ, as a function of x_1 for $\alpha = 0.7$ mixtures. Values at these approximate η were obtained by interpolation.

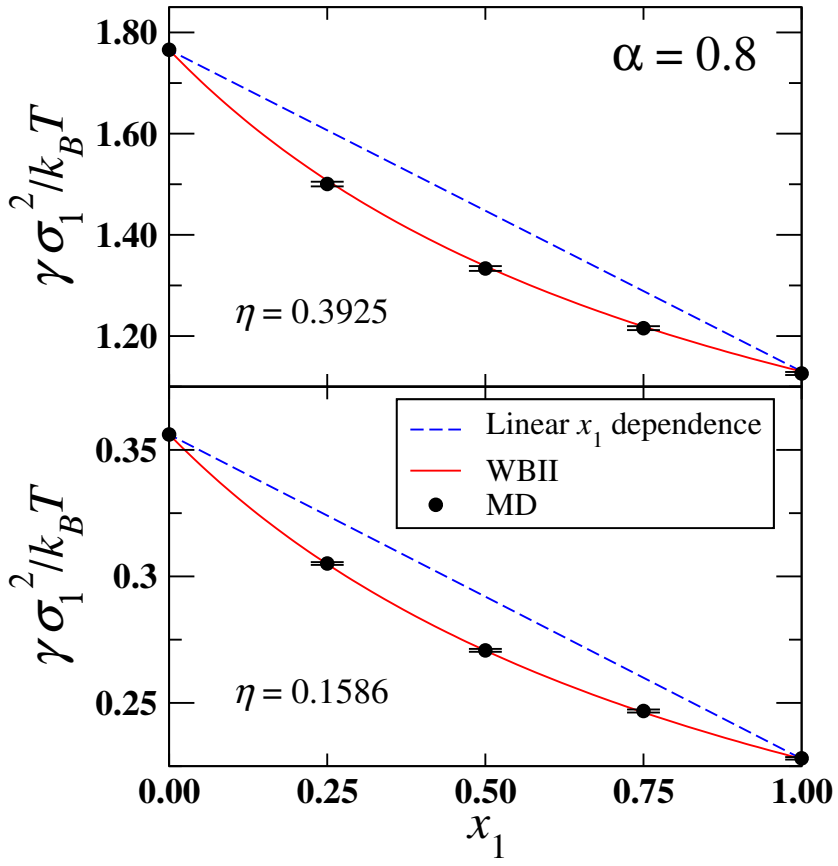

Figure 4.24: Interfacial free energy per unit area, γ, as a function of x_1 for $\alpha = 0.8$ mixtures. Values at these approximate η were obtained by interpolation.

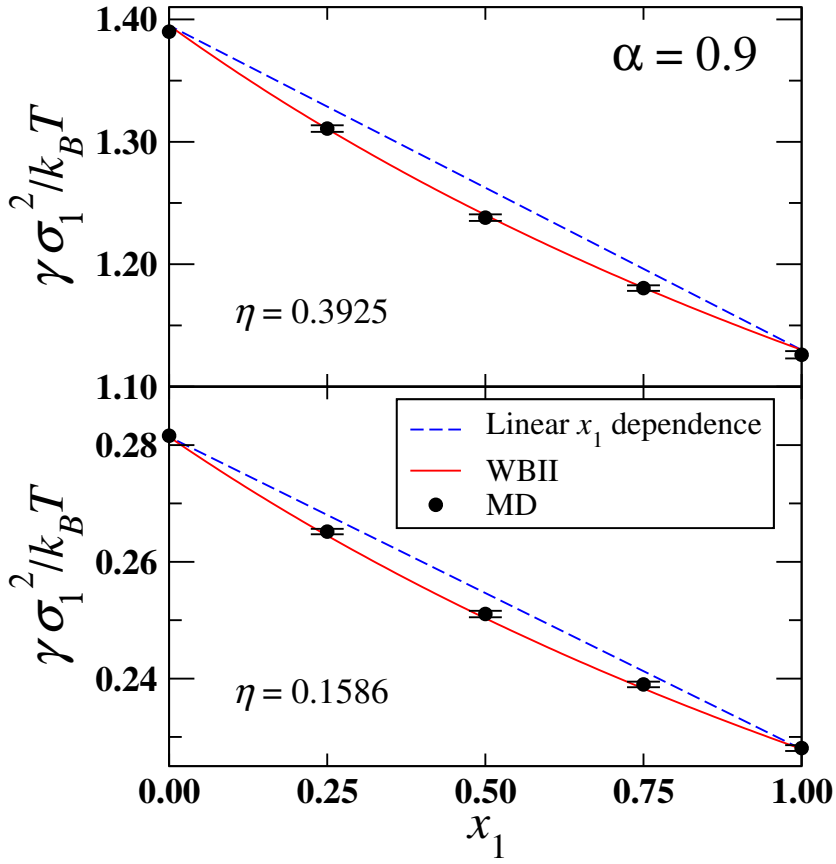

Figure 4.25: Interfacial free energy per unit area, γ, as a function of x_1 for $\alpha = 0.9$ mixtures. Values at these approximate η were obtained by interpolation.

4.6 Summary

The solid-liquid interfacial free energy, γ, plays a central role in a variety of surface phenomena. Much of the attention devoted to understanding the microscopic nature of γ has been given to molecular simulation of interfacial systems, due to the difficulty of performing accurate experimental measurements. The hard-sphere/hard-wall (HS/HW) model can be used to approximate systems in which particle interactions are governed primarily by repulsion or molecular geometry and in which the solid and liquid phases are strongly heterogeneous. The binary HS fluid is of particular interest because many technologically relevant interfacial systems involve multiple components. While binary HS/HW systems have been the subject of classical density-functional theory studies [38, 48–51], high-precision simulation results had yet to be obtained.

In this work, molecular-dynamics simulation is used to determine the interfacial thermodynamics of hard-sphere fluid mixtures at a hard wall as functions of density (or packing fraction) and composition (x_1) for diameter ratios $\alpha = 0.7$, 0.8 and 0.9. The interfacial free energies for the systems studied are determined by first determining the excess interfacial volume v_N and adsorption $\Gamma_{1|N}$ for each α, composition (x_1) and packing fraction studied and then obtaining γ by numerically integrating a Gibbs-Cahn adsorption equation. Comparison with the predictions from the White Bear II (WBII) density functional [38] show that the WBII theory is in excellent agreement with the simulation data, except for small deviations at the highest packing fractions ($\eta > 0.45$). The results show that the contribution to

γ from the adsorption $\Gamma_{1|N}$ is very small compared to that from the excess volume (v_N) for the diameter ratios studied. For this reason, high precision values of γ were obtained at all packing fractions and compositions despite the large statistical errors in the measured values of the adsorption $\Gamma_{1|N}$.

Extensions of this research to other relevent model systems are numerous. One diameter ratio of theoretical interest is $\alpha = 0.414$, wherein a "NaCl" structure (interpenetrating fcc sublattices) with a maximum packing of 0.793 can be obtained [65]. Rigid geometries other than spheres might also be considered, such as ellipsoids [66], regular polyhedra [67], and symmetric/asymmetric dumbbells [68, 69].

Chapter 5

The Al–Ga solid–liquid interface

Liquid-metal embrittlement (LME) is the phenomenon wherein certain solid metals become fractured or weakened when in contact with a liquid metal. As a mechanism of material failure, there is practical economic and safety significance in studying and better understanding the microscopic behavior surrounding LME. A detailed understanding of interfaces requires probing behavior on the atomic scale, but for metal–metal systems, experimental study using standard spectroscopic techniques is difficult, and reliable results at the atomic scale are rare. In contrast, molecular-dynamics (MD) simulation provides a convenient alternative for the study of metal interfacial systems, where atomistic details of the system can be used to calculate properties of interest.

One example of a metal pair that undergoes LME is solid aluminum with liquid gallium. Using MD simulation and an embedded-atom model, we present a detailed characterization of the structural, thermodynamic, and transport properties of aluminum–gallium solid–liquid interfaces for the (100), (110), and (111) orienta-

tions by calculating density, potential energy, stress, and diffusion constant profiles as well as a two–dimensional Fourier analysis of the interfacial layers. We find that, for each crystal orientation, the liquid pre-freezes at the same lattice spacing as the solid at the sites corresponding to continuing the growth of the crystal.

5.1 Introduction

The determination of the structural and thermodynamic properties of chemically heterogeneous solid–liquid interfaces is important for understanding a number of technologically relevant processes such as wetting and nucleation [70]. Solid–liquid metallic interfaces are difficult to study experimentally because both phases are opaque to standard spectroscopic probes. As a result, much of our understanding of these interfaces come from atomistic simulation. Previous simulation studies on metal–metal interfaces include those on aluminum–copper, copper–lead, and aluminum–lead. Geysermans, *et al.*, [71] examined the interface between solid Cu and liquid Al at 1000 K and found that the Cu crystal induces significant liquid Al density layering at the surface. Palafox-Hernandez, *et al.*, [72] examined the interface between solid Cu and liquid Pb at 625 K and found that significant surface alloying occurs on the (100) interface. Additionally, they observed Pb prefreezing on the (111) Cu surface wherein the Pb layers are compressed by about 2% versus the expected bulk lattice constant and rotated by about 6° relative to the surface Cu layers. Yang, *et al.*, [73] examined the interface between solid Al and liquid Pb at 625K and found considerable anisotropy in the structural and transport properties

for the (100), (110), and (111) interfaces. At this temperature, the (111) interface is faceted, but the (100) and (110) interfaces are rough, with minor interlayer peaks in the density profile located between the first interfacial solid and liquid peaks. It was also observed [74] that this system has an interfacial premelting transition at higher temperatures.

In the present study, we employ atomistic simulations in a study of the chemically heterogeneous Al–Ga system. This system was chosen due to an interest in further understanding the phenomenon of liquid-metal embrittlement (LME), which this metal pair can undergo. LME is a pathway of degradation common to polycrystalline metals having a high melting point (e.g., Al, certain steel alloys) in contact with liquid metals having a low melting point (e.g., Ga, Hg). In LME, the liquid metal extrudes into the grain boundaries between crystallites, which can eventually reduce the strength and rigidity of the material. This embrittlement necessarily forms two solid–liquid interfaces where one grain-boundary interface used to be. The newly formed interfaces are thermodynamically stable if $2\gamma_{sl} < \gamma_{gb}$, where γ_{sl} is the interfacial free energy of one of the (created) solid–liquid interfaces and γ_{gb} is that of the (destroyed) grain boundary. As a result of widespread industrial use of aluminum, there is interest in developing a greater understanding of such polycrystalline aluminum under adverse conditions in order to improve the materials and reduce degradation.

The aluminum–gallium system is one example that undergoes LME. In particular, Al–Ga stands out from other systems that are susceptible to LME in that the process does not require the application of tensile stress to occur [75–77]. This

suggests that there is some characteristic specific to Al–Ga interfaces that encourages LME to a greater extent than in other systems. The mechanism of Al–Ga LME has been studied [78] using computational methods; however, a general characterization of Al–Ga interfaces has not been carried out, experimentally or computationally. While there exist X-ray/TEM techniques for observing Al–Ga LME, their resolution is poor, and they cannot look at the interface confined between bulk solid and bulk liquid. Computationally, it has been only recently that a viable force field for Al–Ga has been produced.

Nam and Srolovitz have developed an isotropic embedded-atom method (EAM) potential for Al–Ga binary systems [79]. They have used the potential to simulate Ga penetration into the $\Sigma 5$ symmetric tilt grain boundary of an Al bicrystal [78]. Despite the fact that their EAM model incorrectly predicts face-centered cubic (fcc) for the pure Ga ground-state crystal structure, the model is generally accepted for use under conditions wherein Ga is in the liquid state. However, it is an open question as to whether the model should be considered acceptable under those same conditions with the additional constraint of interfacial confinement, particularly if prefreezing were to occur. This concern is especially relevant for Ga, as additional anisotropic terms are necessary to accurately reproduce the covalent dimer nature of Ga. Regardless, we use this model in our characterizations of planar interfacial Al–Ga systems.

There are three distinct cases that have been observed for lateral structure of a liquid at a solid interface. (1) the intrinsic liquid structure is "locked in" at the interface, as in the case of Pb–Si(100) [80], (2) the most stable crystalline phase

of the liquid is observed, as in the case of Ga on diamond (111) [81], and (3) the solid substrate imposes a lateral symmetry on the liquid different than that of the liquid's intrinsic solid or liquid structure, as in the case of Bi on Cu(111) [82]. For Ga on diamond(111) at 300 K, a few (001) α-Ga planes of Ga_2 dimers are found between the hard diamond wall and the bulk supercooled Ga liquid. One possible explanation for this structure is that the introduction of a few crystalline dimeric layers of Ga decreases the abruptness of the transition from metallic bonding in liquid Ga to covalent bonding in diamond [81]. This suggests that Ga at a metallic interface should retain its metallic nature and not form many covalent bonds.

The structure and transport kinetics of the Al–Ga interface is characterized in this study through the calculation of profiles for density, stress, potential energy, and diffusion as a function of the distance normal to the interface (here defined to be z). These quantities are calculated at 368 K for the three interfacial orientations (100), (110), and (111) to examine interfacial anisotropy. To determine the structure parallel to the interfacial plane to atomic-level detail, we examine 2-D density maps and Fourier transform structure factors. Interfacial excess energy and excess stress are calculated from the profiles.

5.2 Simulation protocol

We used the EAM many-body potential of Ref. [79] to model the Al-Ga system. Using LAMMPS MD code [9], we created separate solid and liquid systems equilibrated at 368 K and 1 bar at the compositions stated in Ref. [78]. The crystal

is equilibrated at constant pressure ensuring that it is under negligible stress. The corresponding liquid is separately equilibrated at constant cross-sectional area A_{xy} in an $NP_zA_{xy}T$ simulation. The two phases are then placed side-by-side with a separation of a few Ångstroms and allowed to come together at constant $P_z = 1$ bar, and an equilibrium combined system length L_z is found. Finally, production data is collected in an NVT simulation at $V = A_{xy} \times L_z$.

Molecular-dynamics (MD) simulations are performed using the EAM potential of Nam and Srolovitz to model the Al–Ga system [78, 79]. This model was designed to reproduce the experimental phase diagram and subsequently used for the direct simulation of Ga penetration of Al grain boundaries [78, 83]. In order to study liquid Ga at a solid Al surface, we chose to simulate the systems at 368 K, corresponding to the first reported data point on the EAM potential phase diagram [78], and corresponding to a temperature of 63 K above the EAM fcc-Ga melting point, 305 K, as determined by NVE phase coexistence calculations.

We use the LAMMPS program from Sandia National Labs to perform the MD simulations [9]. All simulations were performed with a time step of 1.0 fs, at a temperature of 368 K, and a pressure of 1 bar in constant-pressure MD. To enforce constant temperature and/or constant pressure, we used a Nosé-Hoover thermostat with a 0.1 ps relaxation time and/or an Anderson barostat with a 1.0 ps relaxation time, respectively [6]. Periodic boundary conditions were applied for all three directions in all simulations, and the z-axis represents the direction normal to the interfacial plane.

Solid and liquid configurations are generated separately before creating the interfacial system. First, bulk crystals are equilibrated in the isothermal-isobaric NPT ensemble at mole fraction $x_{\mathrm{Ga}}^{\mathrm{sol}}(368\ \mathrm{K}) = 0.0904$. Using system snapshots nearest to the average volume, the average cross-sectional area A_{xy} is recorded, and a corresponding liquid simulation at mole fraction $x_{\mathrm{Ga}}^{\mathrm{liq}}(368\ \mathrm{K}) = 0.986$ is equilibrated in a constant-area $NP_zA_{xy}T$ simulation, where P_z is the pressure normal to the xy plane. To obtain a box size of approximately 80 Å per side, the number of atoms in the separate solid and liquid simulations was chosen to be approximately 30000 each. The solid and liquid are then conjoined by placing them in a simulation cell together at 4 Å separation and allowing them to come together using $NP_zA_{xy}T$ MD. The resulting equilibrium perpendicular box length L_z is then used in the final constant-volume NVT MD simulation for the calculation of equilibrium averages and density profiles. To avoid Brownian motion of the Al crystal slab, which can artificially broaden the calculated interfacial profiles, we subtract the linear momentum for the 2 innermost layers of the Al crystals during the NVT production simulations [84]. To improve the statistics, 5 independent 1 ns runs are chosen for these final NVT simulations for each crystal orientation. Because of periodic boundary conditions, we therefore have 10 independent interfaces from which to calculate interfacial properties.

5.2.1 Interfacial characterization

We determine a number of interfacial profiles showing how properties change as distance from the interface varies. Structural characterization is carried out by cal-

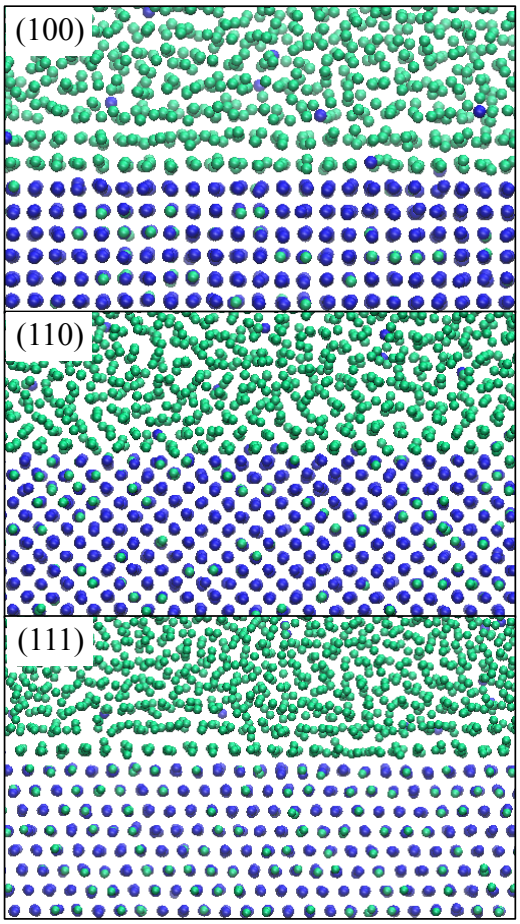

Figure 5.1: Snapshots of the equilibrated Al–Ga (100), (110), and (111) interfaces at 368 K. Blue atoms represent Al, and green atoms represent Ga. All three interfaces are faceted.

culating average density profiles for both species. Thermodynamic characterization is carried out by calculating average potential energy and stress profiles. We also calculate diffusion constants in the liquid layers in the interfacial region.

To calculate coarse-scale density, potential energy, and stress profiles, we filter the fine-scale profiles using a finite-impulse-response (FIR) smoothing algorithm [84]. The fine-scale interfacial profiles are calculated as follows:

- *Density profiles*: The density profiles across the interface, $\rho_i(z), i =$ Al or Ga, are computed as the average number of atoms in each discrete bin of spacing Δz divided by the volume of the bin, $V_z = A_{xy}\Delta z = L_x L_y \Delta z$

$$\rho_i(z) = \frac{\langle N_i \rangle_z}{V_z} \tag{5.1}$$

  where $\langle N_i \rangle_z$ is the average number of atoms of type i in the bin.

- *Potential energy profiles*: The potential energy profile, $U(z)$, is computed by averaging the potential energy in discrete bins and dividing by the volume of the bins

$$U(z) = \frac{\langle U \rangle_z}{V_z} \tag{5.2}$$

- *Stress profiles*: The stress profile, $S(z)$, is determined as the difference between the normal and transverse components of the pressure tensor, averaged within the bin

$$S(z) = P_{zz}(z) - \frac{1}{2}\left[P_{xx}(z) + P_{yy}(z)\right] \tag{5.3}$$

- *Diffusion constant profiles*: To determine the diffusion constant profiles we first assign the particles (at an initial time t_0) to coarse-grained bins in z, defined as the regions between the minima of the fine-grained density

profiles. The diffusion constant in each bin is then determined from the slope of the average mean-square displacement (MSD) as a function of time for the particles located in the bin at t_0

$$D(z) = \lim_{t>t_D} \frac{1}{6}\frac{d}{dt}\left\langle [\mathbf{r}(t) - \mathbf{r}(t_0)]^2 \right\rangle_z \tag{5.4}$$

where t_D is a time large enough that the dynamics is diffusive.

The FIR method is performed by taking a fine-scale profile f_n and applying the equation

$$\overline{f}_n = \sum_{k=-N}^{N} w_k f_{n+k} \tag{5.5}$$

to obtain the filtered components. The filter coefficients w_k have the form

$$w_k = Ae^{-(k/\varepsilon)^2}, \qquad k = -N, \ldots, N \tag{5.6}$$

where ε is a parameter chosen to minimize the quantity

$$S = \sum_n (\overline{f}_{n-1} - 2\overline{f}_n + \overline{f}_{n+1})^2 \tag{5.7}$$

and A is a normalization constant determined by the constraint $\sum w_k = 1$. For the value of $N = 200$ used here, the resulting ε was generally in the range of 75 ± 10.

5.2.2 Interfacial lateral structure and symmetry

For each orientation, we also examine the 2-D structure of the interfacial planes near the interface. Within these interfacial layers, we employ analysis on the average 2-D density map, $\langle \rho_{xy}(\mathbf{r}) \rangle$, where the average includes all particles found within a specific interfacial plane, defined using a bin width equal to the trough-to-trough distance between minima in the density profile. The time-averaged 2-D particle number density is calculated by averaging over 1000 configurations sampled over 1 ns. The underlying symmetries of the interfacial layers are examined by calculating the 2-D structure factor $F_{xy}(\mathbf{k})$[85]

$$F_{xy}(\mathbf{k}) = \left\langle |\rho_{xy}(\mathbf{k})|^2 \right\rangle \tag{5.8}$$

in which $\rho_{xy}(\mathbf{k})$ is the Fourier transform of the 2-D density function for each single configuration and the final average is taken over 1000 configurations.

5.2.3 Calculation of interfacial excess quantities

To calculate interfacial excess quantities, we will first define an imaginary surface which separates the solid and liquid phases. This Gibbs Dividing Surface (GDS) is commonly chosen such that the excess number of particles of one of the species is zero. Once a dividing surface is set, the interfacial excess for some extensive quantity Y is defined as

$$y_{excess} = \frac{1}{2A_{xy}}(Y - y_l V_l - y_s V_s) = \frac{1}{2}\left[\frac{Y}{A_{xy}} - y_l L_l - y_s L_s\right] \tag{5.9}$$

where y_l and y_s are the values of the quantity Y per unit volume in the bulk liquid and solid, respectively. The dividing surface defines the liquid and solid volumes V_l and V_s, and L_l and L_s are the corresponding z-direction lengths of the two phases. The factor of 2 is present because there are two independent interfaces in the simulation. In terms of total box length ($L_z = L_l + L_s$), we have

$$y_{excess} = \frac{1}{2}\left[\frac{Y}{A_{xy}} - y_l L_z - (y_s - y_l)L_s\right] \tag{5.10}$$

In this work, we chose a dividing surface in which the excess number of Al atoms is equal to zero:

$$\Gamma_{\mathrm{Al}} = \frac{N_{\mathrm{Al}}}{A_{xy}} - \rho^l_{\mathrm{Al}} L_z - (\rho^s_{\mathrm{Al}} - \rho^l_{\mathrm{Al}})L_s = 0 \tag{5.11}$$

where N_{Al} is the total number of particles of Al and ρ^l_{Al} and ρ^s_{Al} are the densities of Al in the liquid and solid, respectively. The position of the dividing surface is then determined by solving for the length of the solid

$$L_s = \left[\frac{N_{\mathrm{Al}}}{A_{xy}} - \rho^l_{\mathrm{Al}} L_z\right](\rho^s_{\mathrm{Al}} - \rho^l_{\mathrm{Al}})^{-1} \tag{5.12}$$

The three interfacial excess quantities that are calculated here are the excess energy, $e^{(\mathrm{Al})}$, excess stress, τ, and excess number of Ga atoms, $\Gamma^{(\mathrm{Al})}_{\mathrm{Ga}}$, where the superscript "(Al)" denotes that these quantities were calculated using a dividing surface where the excess number of of Al atoms is zero. $e^{(\mathrm{Al})}$ and $\Gamma^{(\mathrm{Al})}_{\mathrm{Ga}}$ are calculated according to Eq. (5.10), with Y being the total potential energy or number of Ga atoms, respectively. The interfacial excess stress τ is calculated

directly in the MD simulation from the components of the overall average pressure tensor [84, 86]

$$\tau = P_{zz} - \left(\frac{P_{xx} + P_{yy}}{2} \right) \tag{5.13}$$

Because the stress decays to zero away from the interface in both the bulk liquid and solid, the excess stress is independent of the dividing surface.

5.3 Results

5.3.1 Perpendicular and lateral structure

The fine-scale density profiles, $\rho_{\mathrm{Al}}(z)$ and $\rho_{\mathrm{Ga}}(z)$, are shown in Fig. 5.2 for the (100), (110), and (111) Al-Ga interfaces. In all profiles shown, the position of the Gibbs dividing surfaces ($\Gamma_{\mathrm{Al}} = 0$) corresponds to $z = 0$, with $z < 0$ the solid and $z > 0$ the liquid.

The profiles for the solid show peaks corresponding to the crystal planes, with spacing and widths corresponding to the geometry of the specific interfacial orientation. The Al peaks decrease in amplitude (and increase in width) as the interface is approached. All interfaces are faceted, and the solid and liquid density curves are well separated.

The liquid density profiles show peaks corresponding to the typical structural ordering of a liquid phase at a solid surface. For all interfaces, the liquid peaks nearest to the interface are spaced similarly to the corresponding solid. This similar

spacing is an indicator that the liquid is adopting the solid crystal structure for the pre-freezing layers.

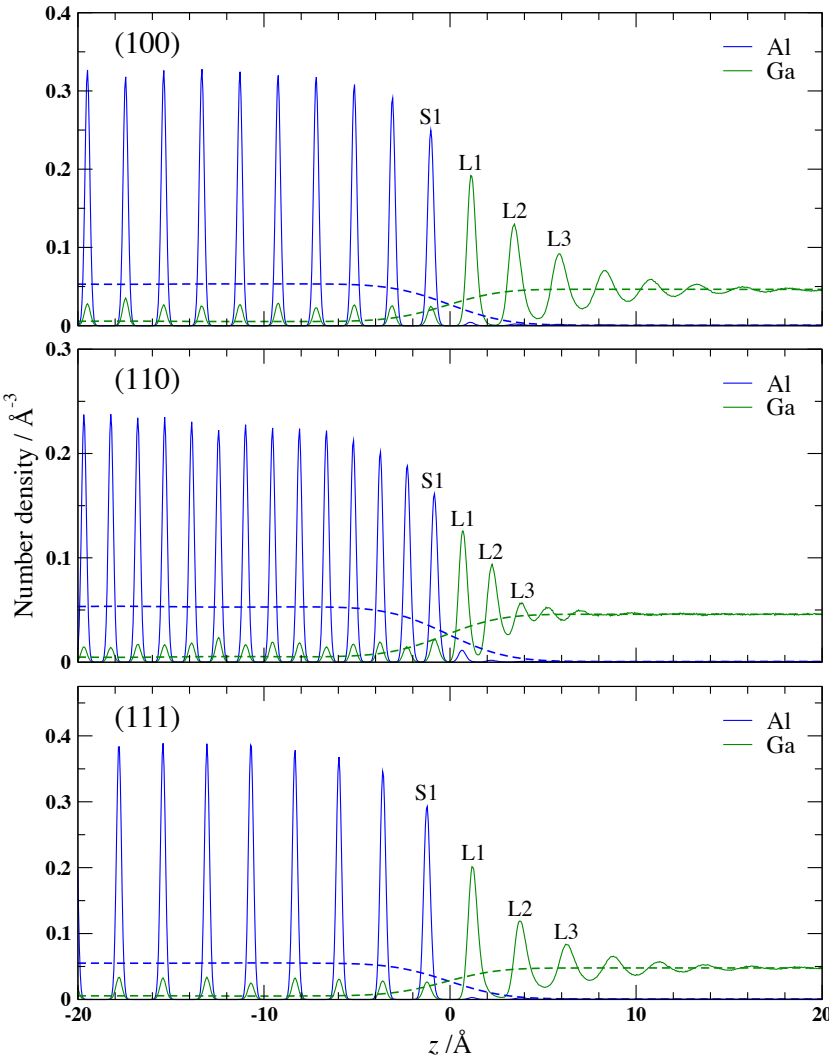

Figure 5.2: Average density profiles near the Al–Ga solid–liquid system for the (100), (110), and (111) interfacial orientations as determined by Eq. (5.1). The dashed lines represent smoothed density profiles obtained with the FIR method. The GDS is located at $z = 0$ in these three plots. Labels correspond to lateral structure factors shown in Fig. 5.3.

In order to further understand the structure at the interface, a 2-D Fourier structural analysis is applied to the interfacial planes, as shown in Fig. 5.3. As shown in the snapshots and density maps, the interfacial gallium atoms occupy the surface sites that continue the structure of the crystal. The 2-D Fourier structure factors reveal a more detailed analysis of the ordering. We observe that the surface Ga layers have a crystalline symmetry consistent with the surface orientation, including adopting the same compressed lattice constant as the substrate of 4.10 Å, versus 4.25 Å for fcc-Ga. This ordering extends out to at least the second liquid layer in all three cases.

5.3.2 Interfacial profiles and excess values of energy, stress, and composition

The smoothed interfacial energy and stress profiles for the (100), (110), and (111) interfacial orientations at 368 K are plotted in Figs. 5.4–5.5. The stress profiles in Fig. 5.5 show approximately zero stress in both the bulk liquid and the bulk solid. For a solid–liquid interface under hydrostatic stress, $S(z)$ measures the difference between the longitudinal and transverse average pressures, and zero stress in the bulk regions indicates that all interfaces have been properly equilibrated under hydrostatic conditions.

The different orientations have different stress profiles. While the (110) and (111) interfaces exhibit only a strong negative peak, the (100) shows a small

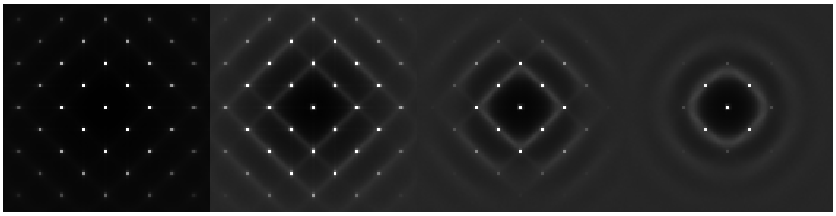

(a) (100) S1 (b) (100) L1 (c) (100) L2 (d) (100) L3

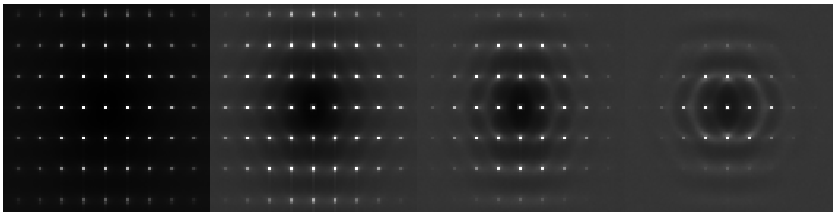

(e) (110) S1 (f) (110) L1 (g) (110) L2 (h) (110) L3

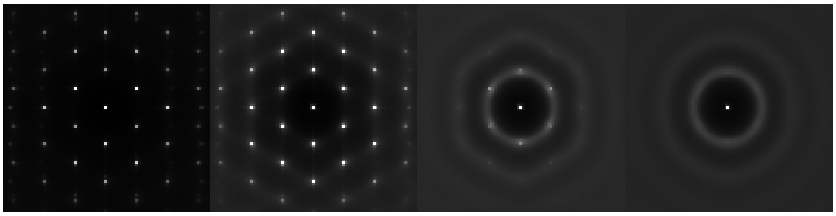

(i) (111) S1 (j) (111) L1 (k) (111) L2 (l) (111) L3

Figure 5.3: Average 2-D Fourier transform structure factors for the (100) (top), (110) (middle), and (111) (bottom) orientations, as determined by Eq. (5.8). Four structure factors are given, from left to right, for layers corresponding to the first interfacial solid peak and the first, second, and third liquid peaks from the density profile, as denoted in Fig. 5.2.

positive peak on the side of the solid and a modest negative peak on the side of the liquid. In contrast, the potential energy profiles in Fig. 5.4 show little anisotropy.

Interfacial excess values are tabulated in Table 5.1. For all orientations, the excess number of gallium atoms at the interface is positive. As a result, the total stress for all of the orientations is negative, which can be attributed to the modest to strong negative peaks in the stress profiles on the Ga-rich liquid side of the

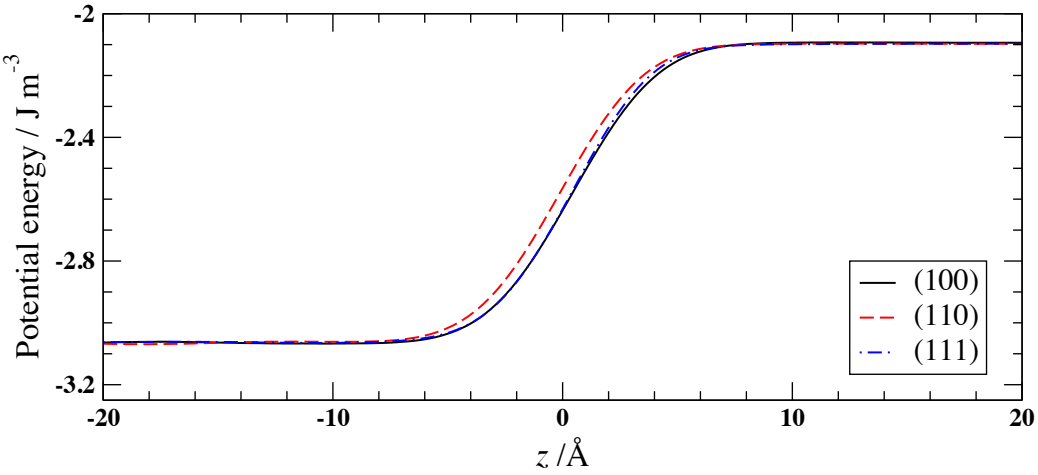

Figure 5.4: Average potential energy profiles for the 3 interfacial orientations as determined by Eq. (5.2).

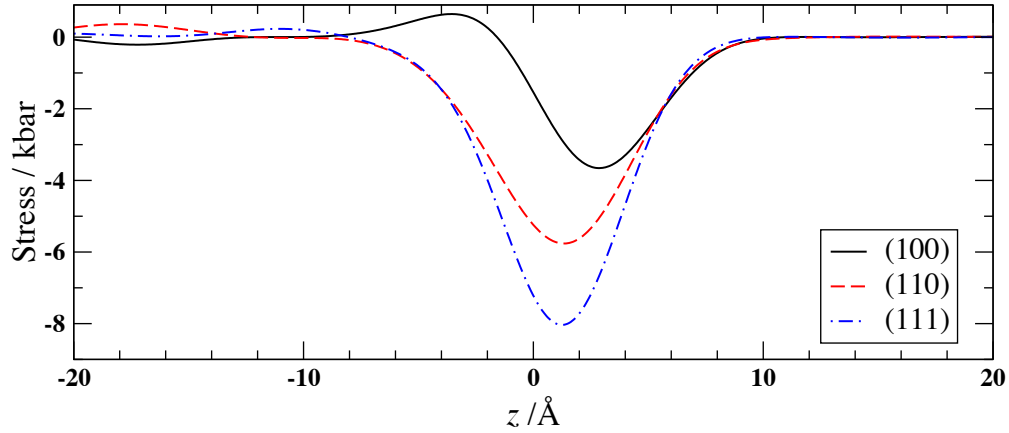

Figure 5.5: Average stress profiles for the 3 interfacial orientations as determined by Eq. (5.3). While the (110) and (111) orientations show a large negative peak (corresponding to compressive stress), the (100) orientation shows a small positive peak on the side of the solid and a moderate negative peak on the side of the liquid.

interfaces. Using the Gibbs-Cahn equation [31–33]

$$\frac{1}{A}\frac{d(\gamma A/T)}{dT} = -\frac{e}{T^2} + \frac{\tau}{AT}\frac{dA}{dT} \tag{5.14}$$

Table 5.1: Al–Ga interfacial parameters at 368 K. Determined from the FIR smoothed density profiles and Eqs. All parameters are averaged over 5 ns simulations treated as 5 statistically independent blocks.

	τ / J m^{-2}	$e^{(\mathrm{Al})}$ / J m^{-2}	$\Gamma_{\mathrm{Ga}}^{(\mathrm{Al})}$ / Å^{-2}
(100)	–0.172(9)	–0.70(5)	0.0121(12)
(110)	–0.433(4)	–1.37(3)	0.0288(2)
(111)	–0.511(9)	–0.75(3)	0.0082(3)

the excess stress, τ, and excess energy, e, can be used to calculate changes in the interfacial free energy, γ.

The average diffusion coefficients for the first seven liquid layers are shown in Figs. 5.6–5.8. The choice of seven layers is due to the observation that the maximum number of prominent peaks in the density profiles is seven, for (100). Additional simulations were performed for the diffusion calculations so that atomic positions could be output more frequently, every 100 fs. Averages for each layer are taken over 10 independent simulations of 10 ps each, with 20 diffusion coefficients determined from fitting mean-square displacements in the range 1–10 ps. For the (100) and (111) orientations, minor anisotropy in diffusion is seen out at the seventh liquid layer. Surprisingly, noticeable anisotropy is seen out to the seventh layer of the (110) orientation, despite there being only four prominent interfacial layers. This suggests significant in-plane heterogeneity in this region.

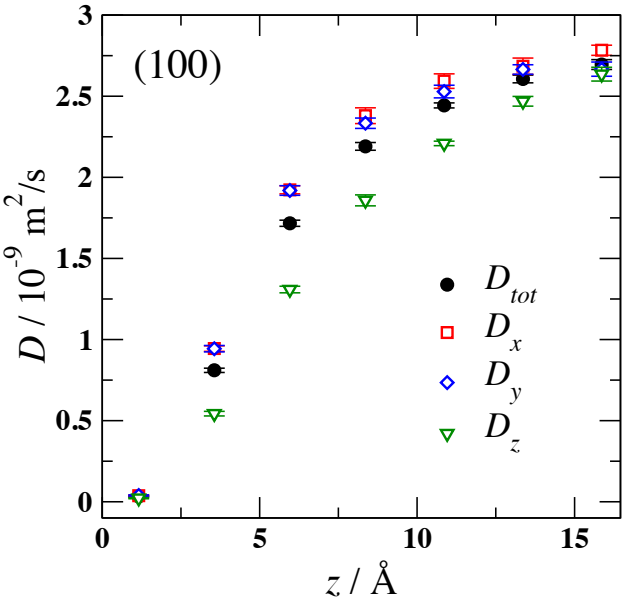

Figure 5.6: Average diffusion coefficients for the (100) interfacial orientation as a function of distance from the GDS as determined by Eq. (5.4).

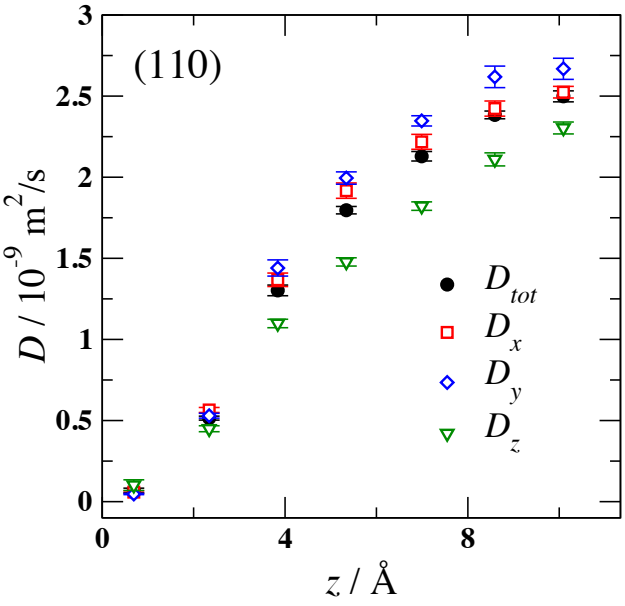

Figure 5.7: Average diffusion coefficients for the (110) interfacial orientation as a function of distance from the GDS as determined by Eq. (5.4).

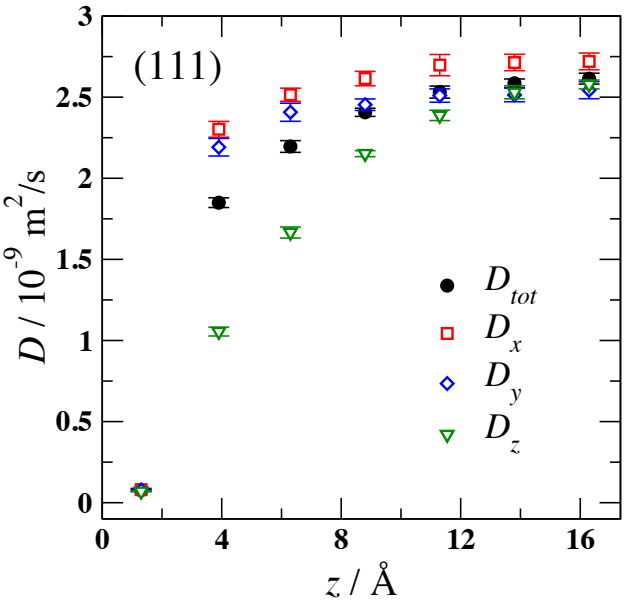

Figure 5.8: Average diffusion coefficients for the (111) interfacial orientation as a function of distance from the GDS as determined by Eq. (5.4).

5.4 Summary

Using an EAM potential and MD simulation, we have examined the chemically heterogeneous interface between solid Al and liquid Ga at 368 K. To determine the anisotropy of the properties of this interface, three different orientations were studied: (100), (110), and (111). For each of these orientations, the structure of the interface was characterized through the calculations of density profiles, as a function of distance along the interface normal, as well as 2-D Fourier analysis of the lateral interfacial planes within the interfacial region. Interfacial thermodynamics was studied through interfacial profiles of energy and stress, and diffusion constant profiles were determined to examine the dependence of transport properties on position relative to the interfacial dividing surface.

The results obtained here differ substantially from those of previous metal–metal solid–liquid interface studies. In contrast to the liquid interfacial structure of the Cu–Pb and Al–Pb systems, the liquid Ga atoms adsorb strongly onto the surface and adopt the structure of the underlying crystal, regardless of orientation. This results in significant compressive stress at the interface, and demonstrates that the stress observed in the direct simulation of Al–Ga LME [78] is not specific to the bicrystal system studied therein.

This study shows a number of pre-freezing gallium layers form on the solid surface of all three orientations. These layers adopt the lattice spacing of the solid substrate, leading to a large compressive stress felt by the gallium atoms. It is an open question as to whether this same pre-freezing structure and stress at the

interface would be seen using more physically accurate potentials or electronic-structure methods. In analogy to the diamond(111)–Ga system [81], it is plausible that the formation of any planes of α-Ga would be unfavorable, as it would introduce a region of covalent bonding that interferes with the metallic bonding in the remainder of the system. Therefore, a metallic structure might be anticipated, and our results reflect such a system.

Advances in imaging technology, such as high-precision aberration-corrected electron microscopy, may soon lead to direct observation of interfacial structure and dynamics. This technique was recently used to observe the direct diffusion of single cerium and manganese dopant atoms within bulk aluminum nitride crystals [87]. The atomic species selectivity, positional precision, and depth sensitivity of this method could provide a wealth of new information pertaining to solid–liquid interfaces that have previously escaped experimental characterization.

Chapter 6

Ethylene-expanded methanol in bulk and within amorphous silica mesopores

For chemical processing, gas-expanded liquids have found great success as reaction media. Under conditions near the critical point of ethylene, the enhanced solubility of ethylene into liquid mixtures involving methanol has recently been exploited in new catalytic processes. One of these processes is the epoxidation of ethylene within metal-doped silica mesopores. In order to better understand how mesoporous confinement affects the behavior of mixtures, we have used molecular simulation to model both the bulk and confined methanol/ethylene systems. First, we present a molecular-simulation study of the phase behavior, structure, and transport properties of mixtures of ethylene and methanol, wherein the ethylene mole fraction is controlled by changing the pressure. We report phase equilibria, volume expansion, liquid structure, and translational diffusion constants for the bulk ethylene-expanded methanol system. The bulk simulation results show excellent agreement with experimental values, where available, and the ethylene and

methanol models show promise for use in further studies on related liquid-state systems. Second, we present a molecular-simulation study of the filling of a number of silica mesopores models under bulk vapor-liquid coexistence conditions.

6.1 Introduction

The standard catalytic process for small olefin epoxidation uses a silver catalyst with molecular oxygen as oxidant, requiring high temperatures and generating moderate amounts of carbon dioxide. Researchers at the Center for Environmentally Beneficial Catalysis (CEBC) have recently been investigating alternative catalytic pathways which use cheaper/more abundant metals as catalyst and produce negligible amounts of carbon dioxide. One such process is epoxidation by H_2O_2 with a methyltrioxorhenium (MTO) catalyst. While the activity and selectivity of this reaction is high, economic analysis shows that there is no advantage when compared to the Ag process, primarily due to the cost of the rhenium catalyst [88]. More recently, CEBC researchers have demonstrated that amorphous silica mesopores functionalized with certain metals, such as niobium, tungsten, or cerium, show activity toward small olefin epoxidation by H_2O_2. The major advantage of the newer process is that it uses metals that are more abundant and less expensive than rhenium.

Gas-expanded liquids (GXLs) are a general class of liquid mixtures in which a compressed gas is added to a solvent. The properties of the GXL are modified from those of the neat solvent, and some GXLs, such as carbon-dioxide-expanded

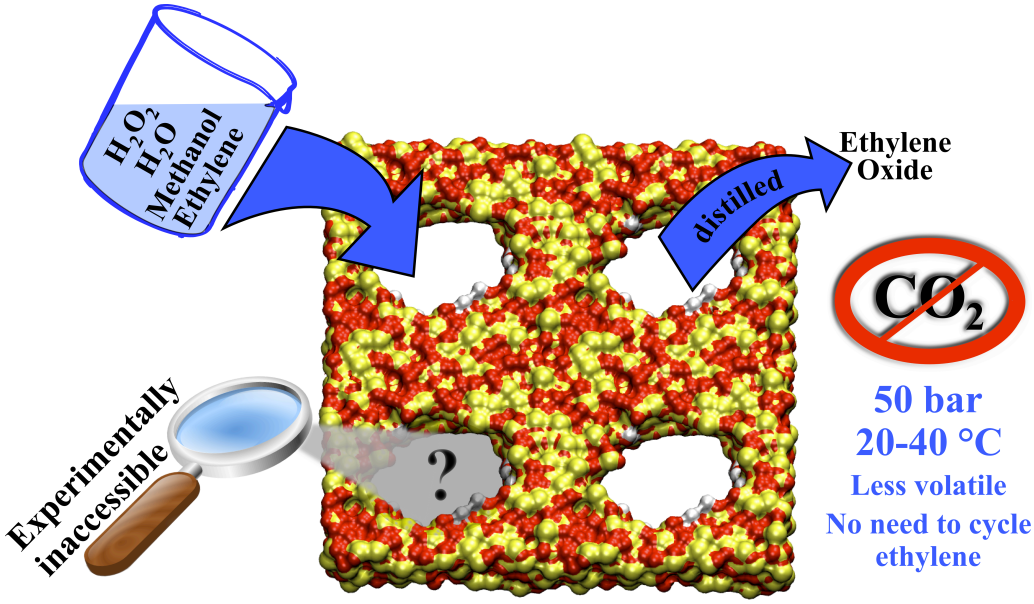

Figure 6.1: Cartoon illustration of epoxidation process. Ethylene and hydrogen peroxide with methanol and water co-solvents enter the metal-exchanged silica mesopore, where the epoxidation occurs. This process takes place under mild operating conditions and eliminates the direct burning of ethylene to form carbon dioxide versus the conventional silver-based process. Because the confined reaction environment is difficult to probe experimentally, molecular simulation is a useful tool in modeling properties such as phase behavior and transport within the pore.

liquids (CXLs), have found success as novel media for chemical processing. The general properties, industrial benefits, and broad range of applications of GXLs has been thoroughly reviewed [89, 90]. With the increased abundance of ethylene from hydraulic fracturing, and with the increasingly large market for ethylene oxide (EO), recent CEBC research has been focused on developing greener catalytic technologies for ethylene epoxidation [91, 92] that make use of gas expansion. In these processes, ethylene is in the solution phase at modest temperatures (20–40°C)

and pressures (up to 50 bar), which significantly lowers the risk of burning ethylene to form carbon dioxide.

While CXLs have recently received significant research attention, ethylene-expanded liquids for chemical processing are of more recent interest. As is the case for carbon dioxide, the critical point of ethylene is not so extreme (about 9.2°C and 50.4 bar [93]), and thus near-critical behavior can be exploited under relatively mild operating conditions. For processes in which ethylene is a reactant, an ethylene-expanded liquid has great utility because it has a relatively high concentration of ethylene and has more favorable transport properties than the unexpanded liquid due to decreased density. Ethylene-expanded methanol is a major component of a previously reported CEBC ethylene epoxidation process [92] in which ethylene is oxidized by hydrogen peroxide within a catalyst-doped silica mesopore. Because experimental studies on these confined systems are difficult, there is interest in computational modeling studies to elucidate the properties that give it such high catalytic activity. One major challenge preventing such studies is the validation of molecular potentials for reproducing mixture properties.

While computational studies on the entire mesoporous catalytic system is our goal, we are restricting our initial efforts to binary liquid mixtures. These studies will allow us both to establish force field compatibility with one another and to determine fundamental properties of the mixtures. We are first interested in validating mixtures of ethylene and methanol. In this chapter, we present the simulation protocol and results for molecular simulations of ethylene-expanded methanol. We have calculated phase diagrams and structural and dynamic properties of the

coexistence (saturated) liquid at temperatures from 20°C–40°C over a range of 5–55 bar, and our results are compared to existing experimental data to validate the potentials for further use. Preliminary results for the composition within the mesopore are also included, and the variation across different pores is discussed.

6.2 Methods

6.2.1 Methanol, ethylene, and silica pore models

The Transferable Potentials for Phase Equilibria-United Atom (TraPPE-UA) potential of Chen, *et al.* [94], was chosen for the methanol (MeOH) model. As phase coexistence calculations are of particular importance, this potential offers benefits over alternative methanol models that were not optimized for phase equilibria. This model consists of a methyl (CH_3) pseudo-atom, oxygen (O) atom, and hydrogen (H) atom. Charges are placed on the three (pseudo-)atom sites, and 12-6 Lennard-Jones (LJ) sites are placed on O and CH_3 atoms. The non-bonded (LJ + Coulomb) interactions $u(r_{ij})$ take the form

$$u(r_{ij}) = 4\varepsilon_{ij}\left[\left(\frac{\sigma_{ij}}{r_{ij}}\right)^{12} - \left(\frac{\sigma_{ij}}{r_{ij}}\right)^{6}\right] + \frac{q_i q_j}{4\pi\varepsilon_0 r_{ij}} \tag{6.1}$$

where r_{ij}, ε_{ij}, σ_{ij}, q_i, and q_j are, respectively, the internuclear separation, LJ well depth, LJ size, and charges on atoms i and j. Lorentz-Berthelot combining rules

[95, 96] are used to determine parameters for dissimilar ($i \neq j$) LJ interactions.

$$\sigma_{ij} = \frac{\sigma_{ii} + \sigma_{jj}}{2} \tag{6.2}$$

$$\varepsilon_{ij} = \sqrt{\varepsilon_{ii}\varepsilon_{jj}} \tag{6.3}$$

The non-bonded potentials from Eq. (6.1) describe only interactions between atoms belonging to different molecules. The cutoff distance for the non-bonded interactions is 14 Å, at which an analytic tail correction [5, 97] is applied and after which interactions are no longer calculated. The bond lengths r_{CO} and r_{OH} are held fixed at 1.430 and 0.945 Å, respectively. An angular potential of the form $\frac{1}{2}k_\theta(\theta - \theta_0)^2$ is employed to allow the molecule to bend, with $\theta_0 = 108.5^\circ$ and $k_\theta/k_B = 55400$ K/rad^2, where k_B is the Boltzmann constant.

While there exists a TraPPE-UA potential [98] for ethylene (C_2H_4), preliminary calculations indicated that it is incompatible with TraPPE-UA MeOH for our purposes. Because TraPPE-UA ethylene lacks an explicit quadrupole, we found that the solubility of TraPPE-UA ethylene in TraPPE-UA methanol was significantly underestimated. Therefore, we have chosen the quadrupolar ethylene potential of Weitz and Potoff [99] (referred to here as qC_2H_4), which, in addition to improved electrostatics, gives excellent vapor-liquid equilibria results, on par with TraPPE-UA ethylene. This model consists of two positively charged methylene (CH_2) pseudo-atoms bonded to a massless center-of-mass (COM) dummy atom, where a negative charge is placed to mimic the electron density located in the double bond.

The charges were chosen to give the model the observed quadrupole moment of ethylene in the gas phase [99, 100]. The bond length is held rigid at all times.

Structures for the silica mesopores were taken from those created by Gulmen and Thompson using a cylindrical resist method [101]. These pores were previously used in the study of ethylene glycol [102], acetonitrile [103–105], and an ethanol-solvated fluorophore [106] under confinement. Force field parameters are similar to the silica potential of Brodka and Zerda [107], with minor modifications made to some of the LJ and Coulomb parameters. In this work, ten mesopores approximately 2.4 nm in diameter and of varying structure, roughness, and number of silanol groups are used. A visualization of Pore #1 is shown in Fig. 6.2; the other pore structures are included in Appendix A.4. Framework Si and O_{Si} atoms are held fixed. Surface hydroxyl moieties O_H–H are held at a rigid bond length of 0.950 Å but allowed to move with respect to the Si–O harmonic bond stretch of the form $\frac{1}{2}k_r(r-r_0)^2$ with $r_0 = 1.663$ Å and $k_r/k_B = 157200$ K and harmonic Si–O–H bend with $\theta_0 = 118.5^\circ$ and $k_\theta/k_B = 12330$ K/rad^2. In the case of surface geminal ($Si(OH)_2$) groups, an additional harmonic O–Si–O bending term is considered with $\theta_0 = 118.0^\circ$ and $k_\theta/k_B = 19200$ K/rad^2. Force field parameters for the silica pore, ethylene, and methanol are summarized in Table 6.1.

6.2.2 Gibbs Ensemble Monte Carlo simulations

Using MCCCS Towhee [28], we employ the Gibbs Ensemble Monte Carlo (GEMC) simulation method [25, 26] for the calculation of phase equilibria and volume expansion. For the vapor-liquid equilibrium (VLE) of the pure substances, canonical

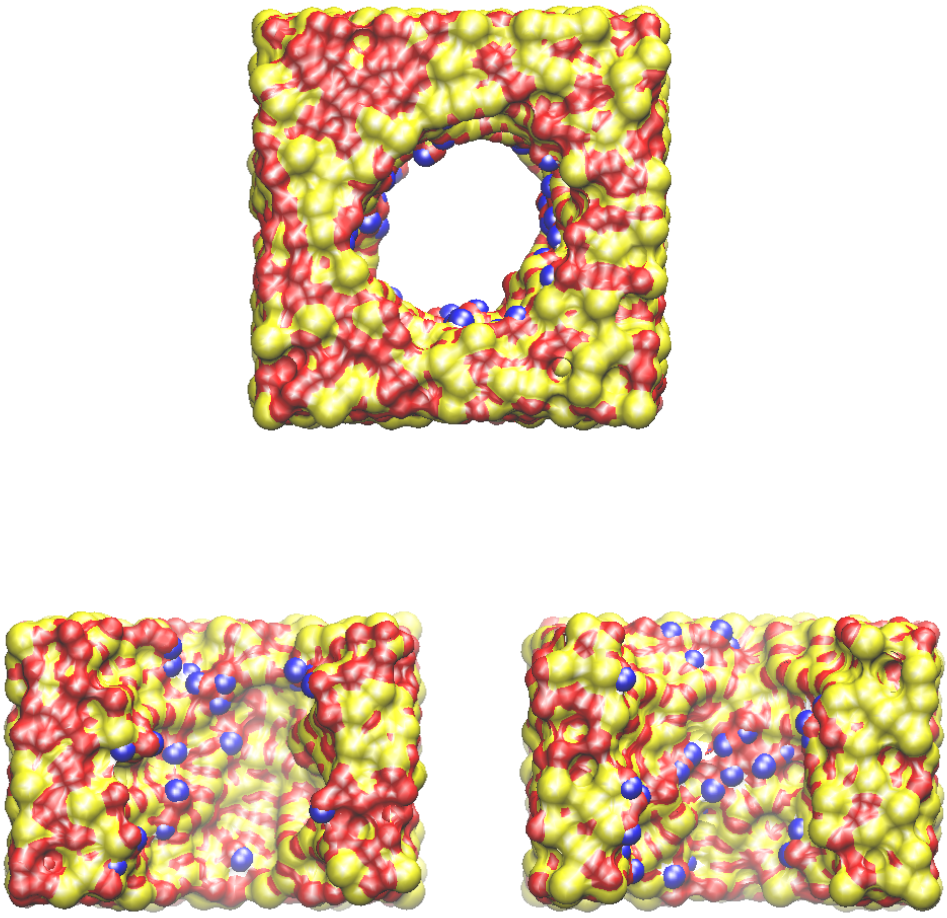

Figure 6.2: Sample silica mesopore, top-down and inside views. The silica (yellow) and oxygen (red) atom locations are indicated by a colored surface, and silanol hydrogen (blue) sites are indicated by spheres. Because of their amorphous nature, each of the pores has a unique structure, most notably, varying surface roughness and number of OH groups.

(*NVT*-)GEMC is used, and for mixture VLE, isothermal-isobaric (*NPT*-)GEMC is used, due to the Gibbs phase rule [27]. In both cases, the two simulation boxes

Table 6.1: Force field parameters for TraPPE-UA methanol, quadrupolar ethylene, and the silica mesopore model. Bond lengths are given in Å, harmonic bond potentials are given in K / Å^2, angles are given in $^\circ$, and harmonic angular potentials given in K / rad^2.

	$q/\|e\|$	σ / Å	ε/k_B / K	Bonds	Angles
CH_3	0.265	3.750	98.0	$r_{CO} = 1.430$	$\theta_{COH} = 108.5$
O	–0.700	3.020	93.0	$r_{OH} = 0.945$	$k_{\theta_{COH}}/k_B = 55400$
H	0.435	0.0	0.0		
CH_2	0.850	3.720	83.0	$r_{CC} = 1.330$	
COM	–1.700	0.0	0.0		
Si	1.28	2.500	0.0503	$r_{SiO} = 1.663$	$\theta_{SiOH} = 118.5$
O_{Si}	–0.64	2.700	230.0	$k_{r_{SiO}}/k_B = 157200$	$k_{\theta_{SiOH}}/k_B = 12330$
O_H	–0.74	3.070	85.5	$r_{OH} = 0.950$	$\theta_{OSiO} = 118.0$
H	0.42	1.295	0.184		$k_{\theta_{OSiO}}/k_B = 19200$

equilibrate to a coexistence state with the vapor and liquid phases having identical temperature, pressure, and chemical potentials for each species. Average vapor and liquid densities are calculated for the VLE of the pure substances, and average ethylene mole fractions are calculated for mixture VLE.

The experimentally determined phase diagrams are available [108–110], and we use these data to validate our two molecular models. To reduce computational time, we initialize our systems to the approximate experimental densities (for NVT-GEMC) or mole fractions (for NPT-GEMC) for a given thermodynamic state. The systems are then equilibrated for 500,000 MC cycles (1 cycle = $N_{molecules}$ steps). Production results are for 1,000,000 MC cycles, which are statistically treated in independent blocks of 100,000 MC cycles each. MC move probabilities are as follows: 0.01 volume change, 0.19 inter-box configurational-bias swap, 0.40 molecule translations, and 0.40 molecule rotations.

6.2.3 Grand Canonical Monte Carlo simulations

In order to carry out the filling of silica pores with the methanol/ethylene mixture, Grand Canonical Monte Carlo (GCMC) simulations are performed using MCCCS Towhee. Initially, the simulation cell is comprised of an empty silica pore, of which all atoms will remain fixed in space. Ethylene and methanol molecules are then allowed to be inserted or deleted with respect to the specified external chemical potential, determined for each species using a Gibbs-Duhem integration method from results of the binary GEMC simulations. The insertion and deletion moves are carried out using a configurational-bias algorithm. The probabilities of all of the possible MC moves are 0.3 insertions/deletions, 0.35 translations, and 0.35 rotations, with equal probability of choosing ethylene or methanol for the move.

In an effort to discern which features of the pore have a major impact on the equilibrium filled pore composition, two different sets of alterations are made to the silica model, and the three pore models are compared to the each other and to the bulk results. The first alternate model is simply the original with all charges removed. The second alternate model is the original with the charges of silanol O_H and H atoms set to zero, with the former charges added to the anchoring silicon atom to maintain charge neutrality. The original, fully charged model is referred to here as "hydrophilic"; the fully uncharged model, "hydrophobic"; and the uncharged OH model, "*pseudo*-hydrophobic".

6.2.4 Molecular-dynamics simulations

After coexistence (saturation) conditions have been determined from our GEMC simulations, we obtain transport properties for the binary mixture using micro-canonical (NVE) simulations, carried out using LAMMPS from Sandia National Laboratories [9] We first initialize the bulk system in a crystal structure at the average liquid phase number densities, as calculated from the GEMC simulations. The system is then melted and heated to the desired temperature. Methanol and ethylene molecules are held rigid using a symplectic quaternion method [111]. For computational simplicity, the (usually flexible) methanol bond angle is held rigid, so that all molecules can be held entirely rigid over the course of the MD simulations. This approximation is validated by the observation that the harmonic angular potential is quite high, and the distribution of angles around the equilibrium position is narrow, $\pm 4^{\circ}$. The average equipartition temperatures of all production trajectories were confirmed to be within 1°C of the target temperature.

MD simulation is also used to generate several independent configurations of the fluid molecules within an approximately equilibrated silica pore. After at least 600 million MC steps have been used to fill the pore using GCMC, the final Towhee configuration is recorded and converted to a LAMMPS input file. MD configurations are then recorded after 0.5, 1.0, 1.5, 2.0, and 2.5 ns, which are used as starting points for GCMC simulations, effectively parallelizing the calculation of equilibrium mole fraction.

6.2.5 Calculation of transport properties

Transport properties are calculated from the MD trajectories $\{\mathbf{r}_i(t)\}$. Snapshots from the MD trajectory are recorded every 100 fs over the course of 10 ns. A translational diffusion coefficient D_t is calculated from mean-square displacements

$$D_t = \frac{1}{6}\frac{\partial}{\partial t}\lim_{t\to\infty}\left\langle(\mathbf{r}(t)-\mathbf{r}(t_0))^2\right\rangle \tag{6.4}$$

where the average is performed over all molecules of a given type and for numerous independent time origins. Fitting to the linear (diffusive) regime is performed from 50–100 ps. Diffusion coefficients may also be obtained from velocity autocorrelation functions using the Green–Kubo relation

$$D_t = \frac{1}{3}\int_0^\infty \langle \mathbf{v}(t)\cdot\mathbf{v}(0)\rangle\, dt \tag{6.5}$$

where $\mathbf{v}$ is a velocity vector.

6.2.6 Peng-Robinson equation of state

We have compared our binary phase equilibria simulation results with those calculated using the Peng-Robinson equation of state (PREOS) [112]

$$P = \frac{RT}{v-b} - \frac{a}{v^2+2bv-b^2} \tag{6.6}$$

where P, R, T, and v are the pressure, gas constant, temperature, and molar volume, respectively. For component i, parameters a_i and b_i are given by

$$a_i = 0.457235 \frac{(RT_{c,i})^2}{P_{c,i}} \left[1 + m_i \left(1 - \sqrt{\frac{T}{T_{c,i}}} \right) \right]^2 \tag{6.7}$$

$$b_i = 0.077796 \frac{RT_{c,i}}{P_{c,i}} \tag{6.8}$$

where $T_{c,i}$ and $P_{c,i}$ are the critical temperature and pressure of component i. The m_i term has the form

$$m_i = \begin{cases} 0.37464 + 1.54226\omega_i - 0.26992\omega_i^2 & ;\omega_i \leq 0.49 \\ 0.379642 + 1.48503\omega_i - 0.164423\omega_i^2 + 0.016666\omega_i^3 & ;\omega_i > 0.49 \end{cases} \tag{6.9}$$

where ω_i is the acentric factor of component i. Using conventional mixing rules, mixture parameters a and b are determined by

$$a = \sum_i \sum_j x_i x_j a_{ij} \tag{6.10}$$

$$a_{ij} = (1 - k_{ij}) \sqrt{a_i a_j} \tag{6.11}$$

$$b = \sum_i \sum_j x_i x_j b_{ij} \tag{6.12}$$

$$b_{ij} = \frac{b_i + b_j}{2} \tag{6.13}$$

Table 6.2: Parameters for PREOS modeling. Critical temperatures (in Kelvin) and pressures (in bar) and acentric factors from Ref. [93]. Binary interaction parameter from Ref. [113].

	Ethylene	Methanol
T_c / K	282.4	512.6
P_c / bar	50.4	80.9
ω	0.089	0.556
$k_{12} = 0.010$		

The critical temperatures, critical pressures, and acentric factors are 282.4 K, 50.6 bar, and 0.089 for ethylene and 512.6 K, 80.9 bar, and 0.556 for methanol [93], and the binary interaction parameter k_{12} is 0.010 [113].

Calculations of VLE are performed by equating the fugacities of each component in the liquid and vapor phases

$$\phi_i^L x_i P = \phi_i^V y_i P \tag{6.14}$$

where ϕ_i is the fugacity coefficient of component i obtained from the PREOS. We have the additional material constraint of mole fraction sums

$$\sum_{i=1}^{2} x_i = 1 \text{ and } \sum_{i=1}^{2} y_i = 1 \tag{6.15}$$

for the liquid and vapor phases. For a fixed temperature and pressure, VLE calculations are carried out using the Newton-Raphson method [114] to obtain coexistence mole fractions. Critical points, acentric factors, and binary interaction parameter for ethylene and methanol are summarized in Table 6.2.

6.2.7 Gibbs-Duhem determination of chemical potentials

A method of determining chemical potentials is required to perform the GCMC simulations to fill the silica mesopore. Typically, chemical potentials can be calculated directly in gases using the Widom insertion method [61]. We find that Widom's insertions fail to give reliable estimations of the chemical potential of methanol at high pressures. Thus, we turn to a Gibbs-Duhem relationship, wherein we can use a more precise estimation of chemical potential at a lower pressure and numerically integrate to find the chemical potential at higher pressures. For species 1 and 2 in coexistence in phases α and β, one can derive

$$\left(\frac{\partial \mu_2}{\partial P}\right)_{coex} = \frac{\left(\frac{\overline{V}}{N_1}\right)_\alpha - \left(\frac{\overline{V}}{N_1}\right)_\beta}{\left(\frac{x_2}{x_1}\right)_\alpha - \left(\frac{x_2}{x_1}\right)_\beta} \tag{6.16}$$

and the corresponding equation for species 1 is obtained by swapping all species indices. The advantage of using this technique is that the molar volume $\overline{V}$, particle numbers N_i, and mole fractions x_i fluctuate much less drastically in comparison to the chemical potential and can be monitored over the course of the GEMC simulations. The integration was carried out using the trapezoid rule, using the Widom's method chemical potential at 20 bar as a starting point, as it generally had the lowest error across all Widom's measurements. The error in μ_i/k_B introduced by the integration is insignificant, at a few Kelvin per integration step.

6.3 Results and discussion

6.3.1 Phase equilibria in pure ethylene and methanol

To validate our methods and the chosen potentials for C_2H_4 and MeOH, we first test their ability to predict liquid–vapor coexistence in the pure systems. Our NVT-GEMC results for the liquid–vapor phase diagram for ethylene are given in Fig. 6.3(a). Both the liquid and vapor densities are in good agreement with experiment [108], save for temperatures closest to the critical temperature. Results for methanol are given in Fig. 6.3(b), shown with experimental data [109].

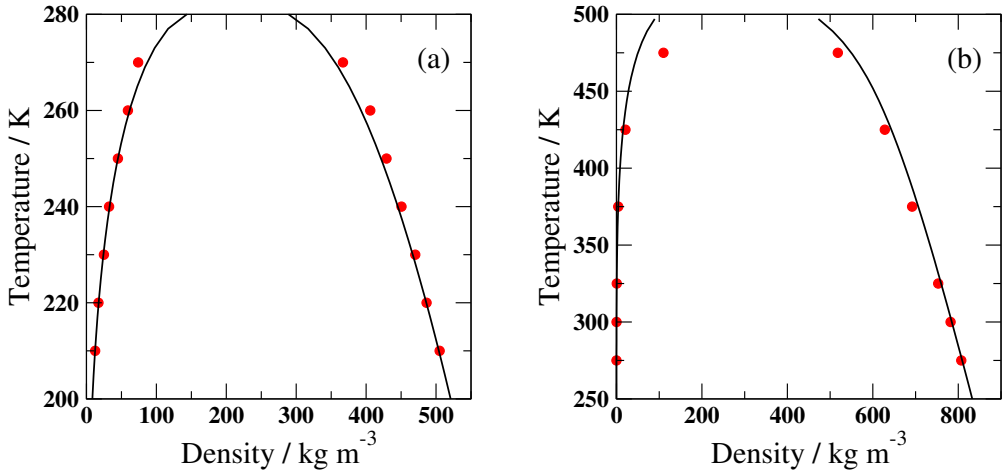

Figure 6.3: Pure VLE diagrams for (a) ethylene and (b) methanol. The qC2H4 ethylene and TraPPE-UA methanol model NVT-GEMC results are shown as red circles, and the corresponding experimental densities [108, 109] are shown as black curves.

6.3.2 Binary phase equilibria in C_2H_4-expanded MeOH

For the two-component vapor–liquid equilibria, we compare our *NPT*-GEMC results with experimental phase diagrams [110] at 25°C and 40°C. Our computational results at pressures of 5, 10, 20, 30, 40, 50, and 55 bar are given in Fig. 6.4, compared to the experimental values and Peng-Robinson equation of state (PREOS) predictions. At 40°C, our results and PREOS estimate the liquid composition fairly well, but at 25°C our simulations perform substantially better than the PREOS. This suggests that our simulations account for near-critical behavior in this system better than the PREOS, demonstrating the utility and accuracy of molecular simulations. Of course, it is possible that alternative Peng-Robinson parameters or other equations of state might give results more accurate than the current simulations.

6.3.3 Volume expansion

One common experimental measure of vapor–liquid phase behavior is the volume expansion of the solvent with increasing pressure at fixed temperature. The practical benefits of using an expanded liquid is enhanced transport and less solvent use versus the unexpanded reaction media. Volume expansion is quantified by the expansion ratio, V/V_0, where V_0 is the volume of a sample of neat solvent at 1 atm and the chosen temperature. The degree of expansion is highly dependent on system and conditions. For example, experimental and computational studies

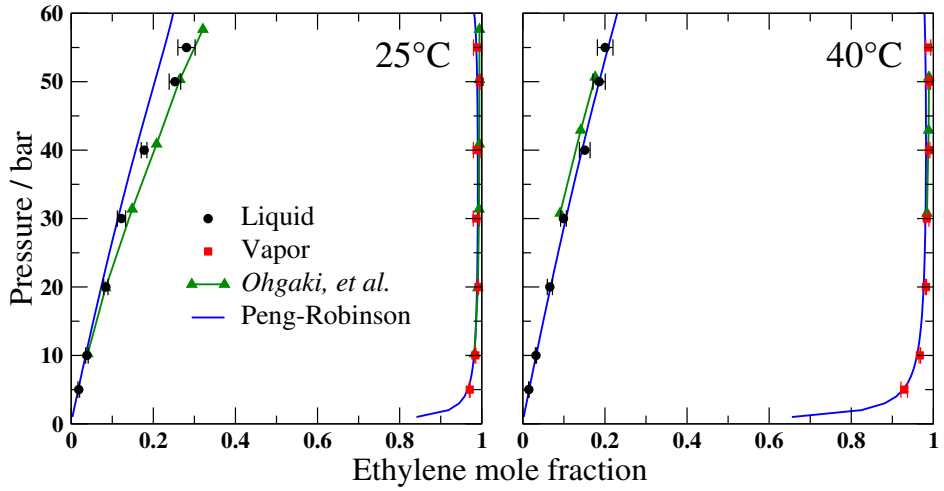

Figure 6.4: Mixture phase diagrams for methanol/ethylene at 25°C and 40°C. The qC2H4 ethylene and TraPPE-UA methanol model results are shown as symbols (black circle = liquid; red square = vapor), and the corresponding experimental densities [110] are shown as green triangles connected by lines. Also included are PREOS predictions, given by solid blue curves.

[115] of carbon-dioxide-expanded acetonitrile found expansion ratios near 3 at the relatively mild conditions of approximately 25°C and 45 bar.

From the binary vapor–liquid coexistence simulations, one can also measure the volume expansion of the solvent with increasing pressure. As the pressure is increased, the volume of the liquid increases due to dissolution of ethylene. Expansion factors for the methanol/ethylene binary are shown in Fig. 6.5, compared to expansion experiments [91] performed at 20°C, 30°C, and 40°C. While the calculated results differ quantitatively from the experimental results, the super-linear dependence on the pressure at higher pressures is retained, particularly nearer to the ethylene critical temperature.

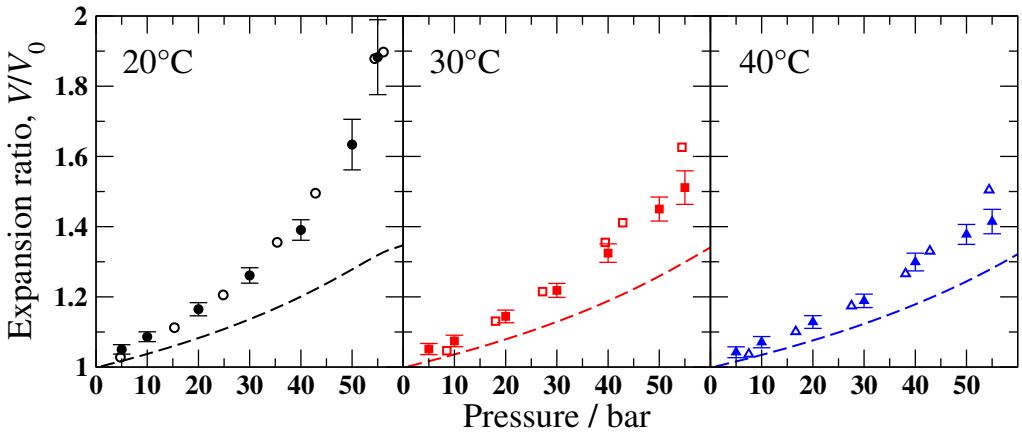

Figure 6.5: Volume expansion ratios for methanol/ethylene saturated liquid mixtures at 20°C, 30°C, and 40°C. Model results are shown as closed symbols, experimental results [91] as open symbols, and Peng-Robinson predictions as dashed curves.

6.3.4 Local liquid structure

Radial distribution functions (RDFs) $g(r)$ and coordination number $n(r)$ plots for ethylene COM–COM, ethylene COM–methanol O, and methanol O–O are shown in Fig. 6.6. Interestingly for COM–COM, as pressure increases the height of the first $g(r)$ peak (near 4.4 Å) decreases while that of the second (near 8.4 Å) increases. In the first coordination shell (within 6.7 Å), the average number of ethylene ranges from 0.4 at 5 bar to 6.0 at 55 bar. Increasing the pressure also shifts the second g(COM–COM) peak outward, from about 8.2 to 8.6 Å, which may be attributed to the liquid density decrease.

The G(COM–O) distributions have one weak peak located near 5.0 Å. In this coordination shell (within 6.4 Å), the average number ranges from 14.8 at 5 bar to 7.1 at 55 bar.

The g(O–O) distributions have peaks located near 2.8 and 4.9 Å. The first peak is sharp, and the corresponding n(O–O) in that range is a nearly flat plateau. As pressure is varied, there is no noticeable change in the first peak, and thus the coordination number in the first shell (within 3.5 Å) remains constant, around 2. This suggests that the strong intermolecular (hydrogen-bonding) interactions between methanol molecules mitigate changes in methanol solvation/aggregation due to density change.

While the RDFs demonstrate that the local liquid structure does not change much across the pressure range, this result is not unexpected. In previous work [116] on CO_2-expanded acetonitrile, the only RDF that showed a substantial change with pressure was for N–N. This was attributed to the orientational segregation of nearby molecules, which preferentially adopted parallel, perpendicular, or antiparallel relative orientations depending on the pressure. This same phenomenon does not occur for the ethylene in this system, due to its zero dipole moment.

6.3.5 Translational diffusion

Translational diffusion for ethylene was determined using both mean-square displacement (MSD) and velocity auto-correlation function (VACF) relations. MSDs were calculated every 100 fs out to 100 ps using 10 ns trajectories separated into 10 blocks. We performed linear fitting on MSDs in the 50–100 ps range. Due to the volumetric expansion as pressure is applied, diffusion is enhanced at higher pressures. The ethylene diffusion coefficient D_t is near 4×10^{-9} m^2 s^{-1} at 5 bar and increases considerably to over 9×10^{-9} m^2 s^{-1} at 55 bar.

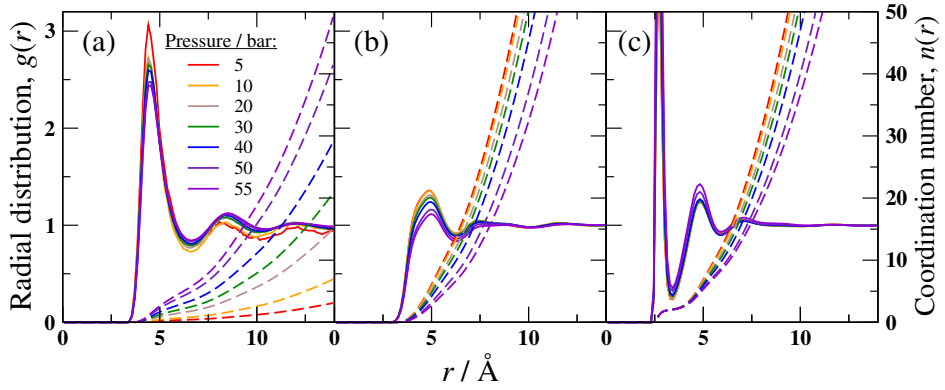

Figure 6.6: Radial distribution functions for methanol/ethylene mixtures as a function of temperature. (a) COM–COM, (b) COM–O, (c) O–O. No significant changes to the local liquid structure are observed. The O–O coordination number in the first solvation shell is constant across the pressure range, suggesting that hydrogen bonding between methanol molecules is unaffected by changes in pressures and corresponding compositions between 5 and 55 bar.

Based on center-of-mass dummy atom velocities, ethylene VACFs were calculated every 10 fs out to 5 ps using 0.5 ns trajectories. The 5 ps cut-off was chosen because all VACFs are decayed to zero within error bars by that time. Integration on the VACFs was performed using the trapezoid rule. At 5 and 10 bar, the VACF results for the ethylene diffusion coefficient agrees quantitatively with the MSD results. At 20 bar and above, the VACF method overestimates D_t, with a maximum deviation of less than 10% versus the MSD method. In principle, the MSD and VACF routes to D_t are equivalent, but the slowly decaying nature of the VACFs can render the Green–Kubo relation unreliable for calculations over short times and costly for calculations over long times. That the VACF results agree with the MSD results better at lower pressures can be attributed to the fact that the VACF

should decay more quickly with increasing density (or decreasing pressure for these expanded liquids).

Because of the difficulty in determining the center-of-mass velocity of methanol molecules, diffusion coefficients for methanol were not calculated using the VACF method for a number of reasons. First, determining the the center-of-mass velocity of methanol molecules is difficult. Second, we are only currently interested in qualitative results, and the MSD and VACF methods give qualitative agreement for ethylene. We assume that MSD results alone will be sufficient. Results for translational diffusion are summarized in Figs. 6.7–6.8.

6.3.6 Chemical potentials at phase coexistence

Chemical potential measurements for ethylene and methanol were collected during the *NPT*-GEMC production blocks using the Widom's insertion method [61]. Because of the difficulty in converging the calculation, a Gibbs-Duhem relationship (Eq. 6.16) was used to find the chemical potentials at various pressures, integrating from 20 bar, where convergence was generally best.

6.3.7 Composition within mesopore

Results for the pore-filling simulations were collected in collaboration with Dr. Krista Steenbergen. Using the chemical potentials from the *NPT*-GEMC simulations, GCMC was used to fill a series of ten silica mesopores at 20°C and 5–55 bar. The "hydrophilic" (fully charged), "hydrophobic" (fully uncharged), and

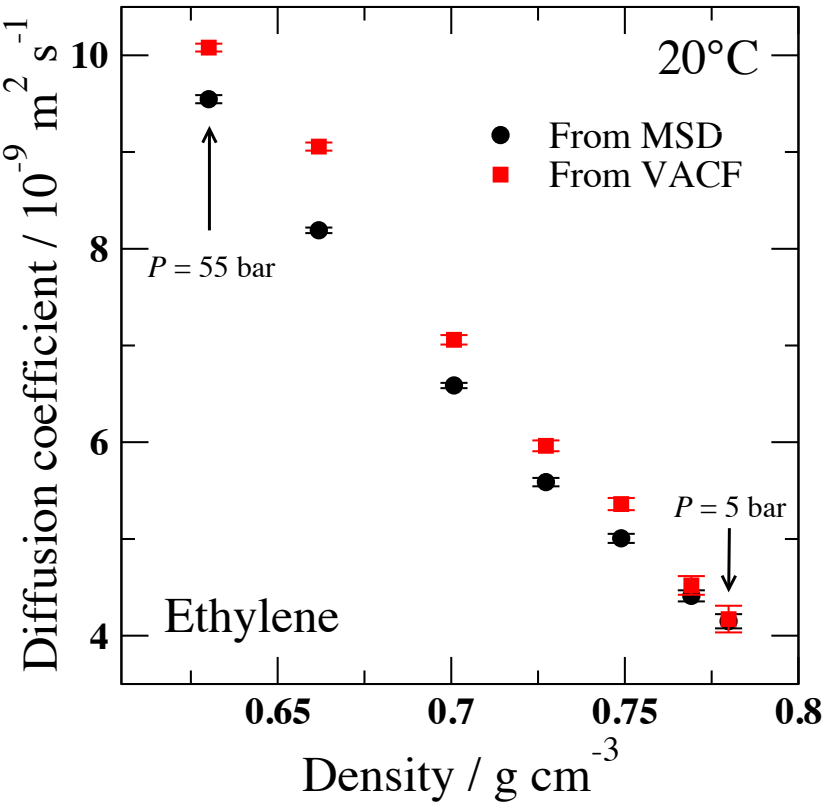

Figure 6.7: Ethylene translational diffusion coefficients D_t as a function of density, as calculated from MSD and VACF data, for the saturated bulk liquid mixtures at $T = 20°C$ and $P = 5, 10, 20, 30, 40, 50, 55$ bar.

"*pseudo*-hydrophobic" (uncharged OH) pore models show different amounts of uptake. While there is minor variance in the ethylene mole fraction across the many pores for each model, there are no significant outliers (Figs. 6.10–6.11).

In order to examine trends among the different pore geometries, we present the mixture composition within the pore versus the number of OH groups. Figures 6.13–6.14 show the pore-filling results for the nine pores that have been modeled as both hydrophilic and *pseudo*-hydrophobic. It was expected that the number of OH

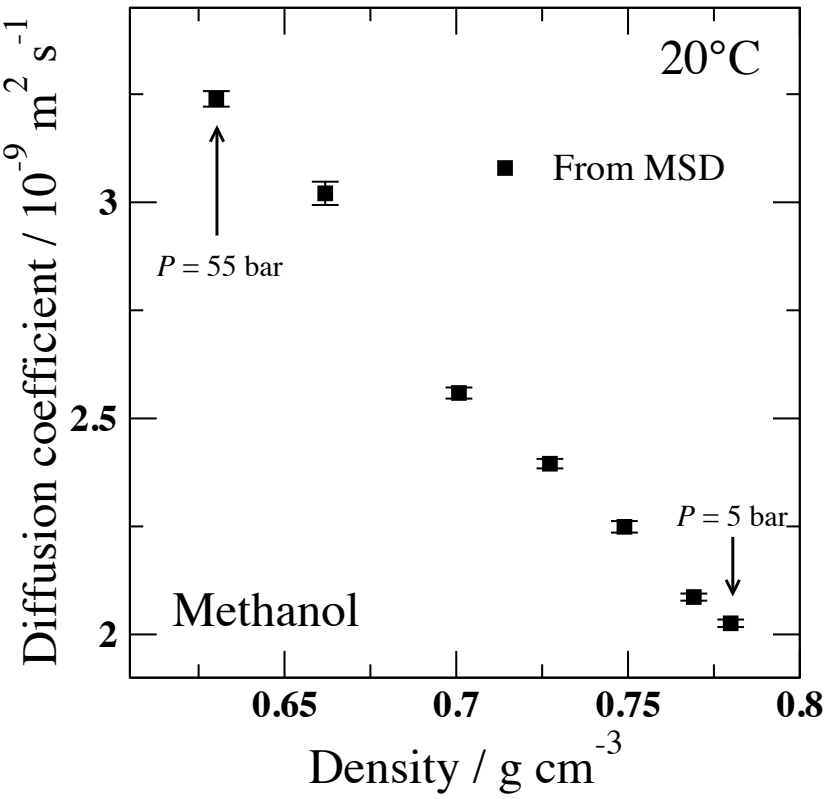

Figure 6.8: Methanol translational diffusion coefficients D_t as a function of density, as calculated from MSD data, for the saturated bulk liquid mixtures at $T = 20°\text{C}$ and $P = 5, 10, 20, 30, 40, 50, 55$ bar.

groups present in the pore would have a significant effect on ethylene uptake when the OH charges are on and less of an effect when the charges are off. However, for both hydrophilic and *pseudo*-hydrophobic models and across all pressures, there is a clear trend of decreasing ethylene mole fraction with more OH groups. It is also observed that there is not a significant dependence of the total number of molecules adsorbed within the pores on the number of OH groups (not shown).

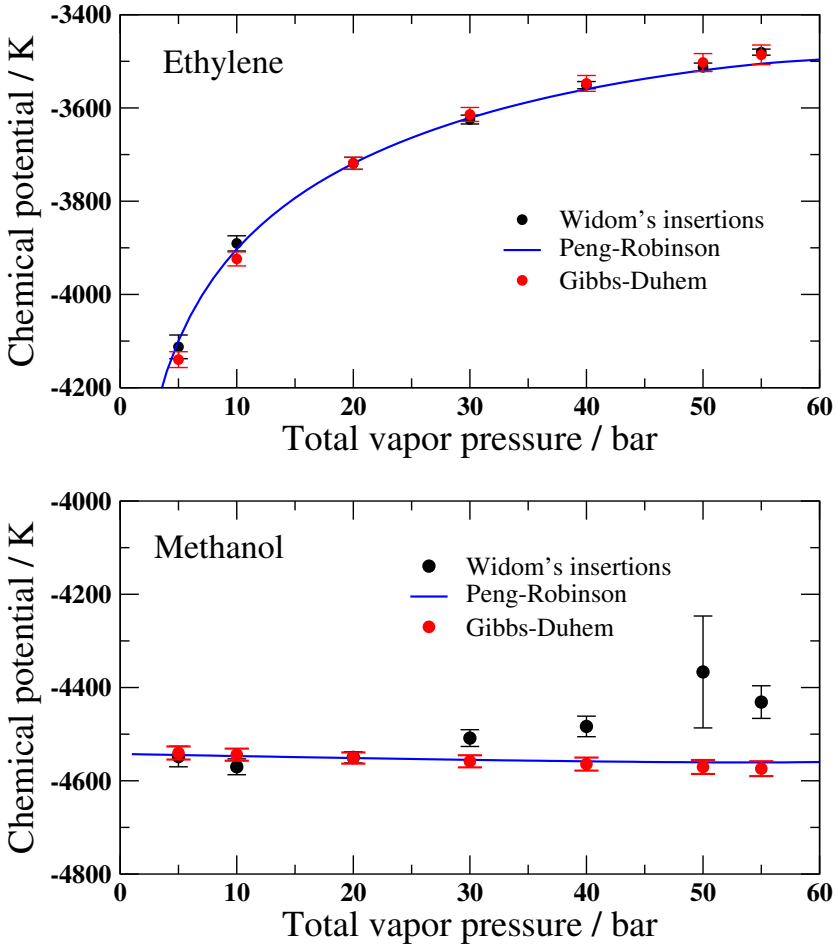

Figure 6.9: Chemical potentials for ethylene and methanol as determined from *NPT*-GEMC simulations of the binary vapor-liquid equilibrium system using the Widom's insertion method and Gibbs-Duhem integration. Peng-Robinson predictions are also shown. The Gibbs-Duhem results were used for the GCMC pore-filling simulations.

6.4 Conclusion

Simulations on ethylene-expanded methanol have been carried out using Monte Carlo and molecular-dynamics simulations. Phase equilibrium calculations for the

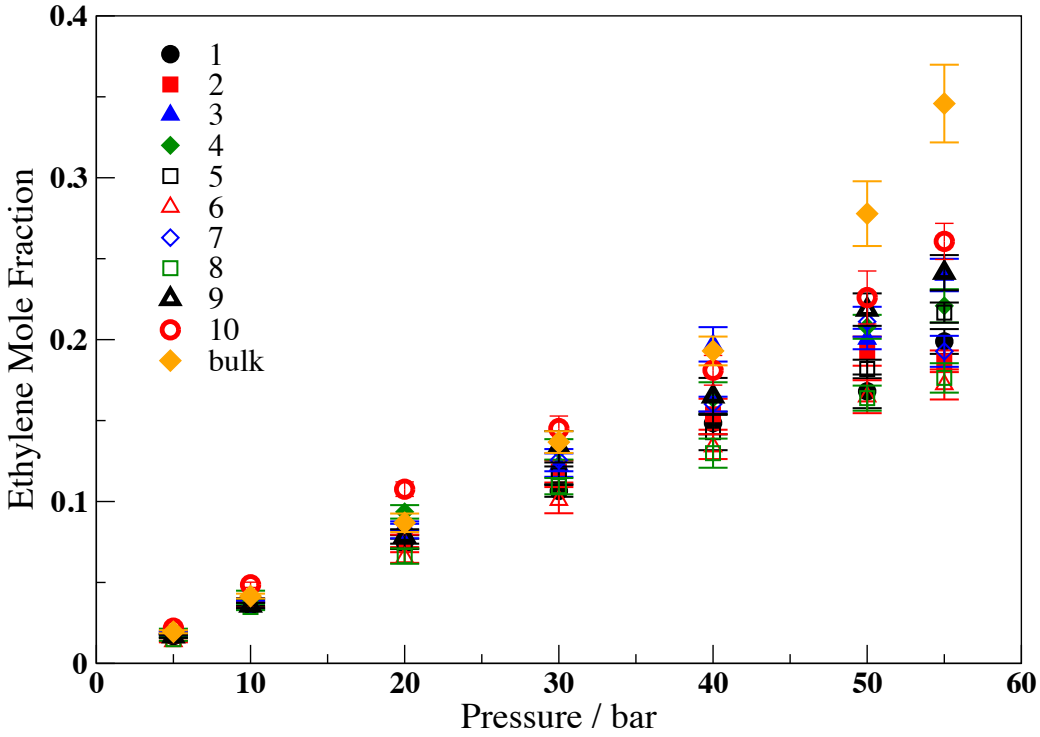

Figure 6.10: Ethylene/methanol mixture composition within ten model hydrophilic silica pores with varying structure, roughness, and number of surface silanol groups. Of the three model types, the hydrophilic pores have the lowest adsorption selectivity toward ethylene uptake. The ethylene mole fraction is generally less than that of the bulk at the same conditions.

pure and binary systems show good agreement with experimentally determined phase diagrams. The volume expansion results for the saturated liquid mixture are more accurate than the Peng-Robinson predictions and retain the characteristic super-linear dependence on pressure. Translational diffusion in the liquid decreases with increasing density. The ethylene and methanol force fields show promise as compatible models for future studies. Rotational diffusion remains to be charac-

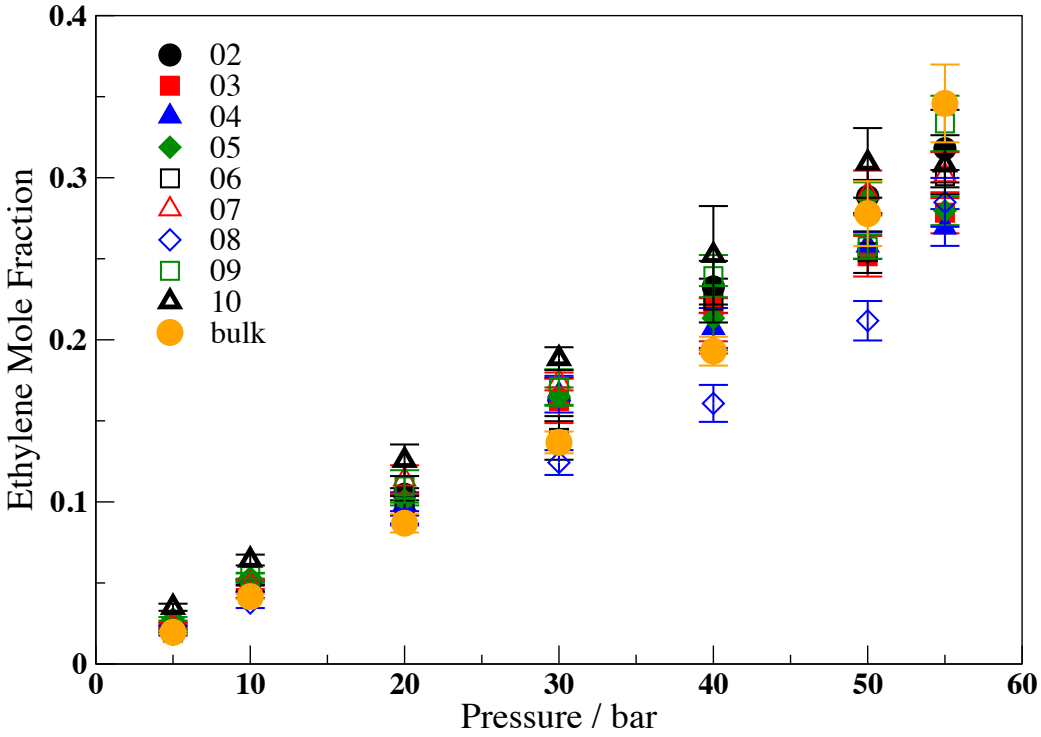

Figure 6.11: Ethylene/methanol mixture composition within nine model *pseudo*-hydrophobic (uncharged OH) silica pores with varying structure, roughness, and number of surface silanol groups. Of the three model types, the *pseudo*-hydrophobic pores have moderate adsorption selectivity toward ethylene uptake. The ethylene mole fraction is generally comparable to that of the bulk at the same conditions.

terized in these systems, including using the extended jump model [117, 118] to determine methanol reorientation lifetimes.

Grand Canonical Monte Carlo results show how the amorphous silica pores are filled by methanol/ethylene mixtures as the external conditions are varied. Like in the bulk, pronounced solubility of ethylene in methanol is achieved. The importance of long-ranged Coulombic interactions was demonstrated by comparing three models of different nominal hydrophobicity, where the ethylene mole fraction

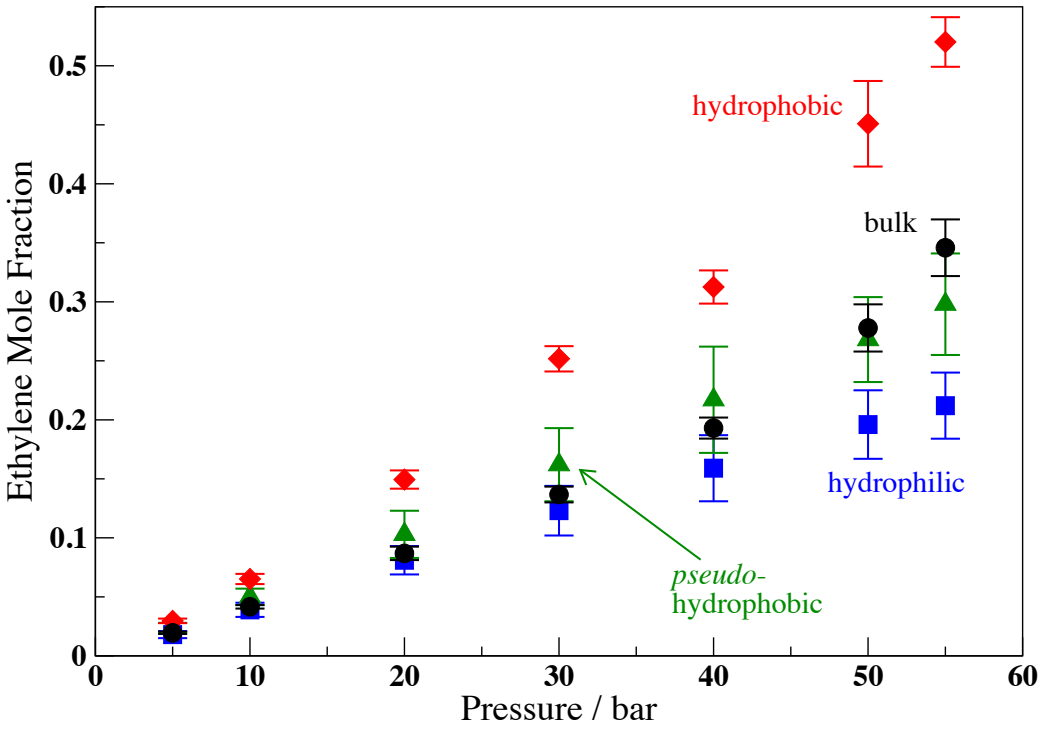

Figure 6.12: Comparison of mixture composition across bulk ethylene/methanol and the three pore models. The hydrophilic and *pseudo*-hydrophobic data represent averages and 2σ standard deviations for the confined mixture pore compositions shown in Fig. 6.10 and Fig. 6.11, respectively. The hydrophobic data is for the average mole fraction for a single pore. As charges are removed from the model, the adsorption selectivity toward ethylene increases.

of the confined liquid at 20°C and 55 bar ranges from 0.2 to 0.5 for our hydrophilic and hydrophobic models, respectively. Pores with a greater number of surface silanol groups show reduced adsorption selectivity toward ethylene, whether or not the OH atoms are charged. We also plan on investigating trends in ethylene uptake versus other details that vary among the pore models, such as accessible surface area. Future MD simulations on the confined pore system will allow us to

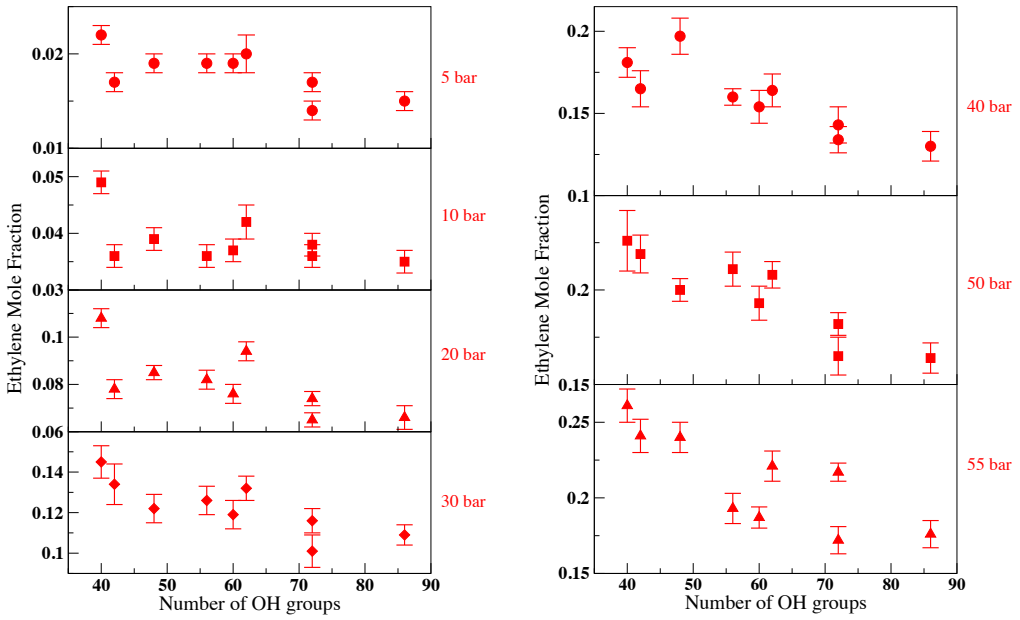

Figure 6.13: Dependence of "hydrophilic" pore composition on number of OH groups. The specified external conditions are those of methanol/ethylene vapor-liquid equilibrium at 20°C and the indicated pressure.

investigate dynamic properties within the pores, such as diffusion and methanol–silanol hydrogen-bonding lifetimes.

The ultimate goal of this work is to predict the composition and dynamics within silica mesopores, with respect to specified external parameters, of the mixtures of ethylene, methanol, water, hydrogen peroxide, and ethylene oxide that are present in the catalytic process. By calculating binary phase diagrams, we have demonstrated that the chosen force fields for ethylene and methanol are a suitable match for this purpose. Moving forward, the three remaining force fields must be chosen. For water, the SPC/E model [119] is an attractive option, due to its

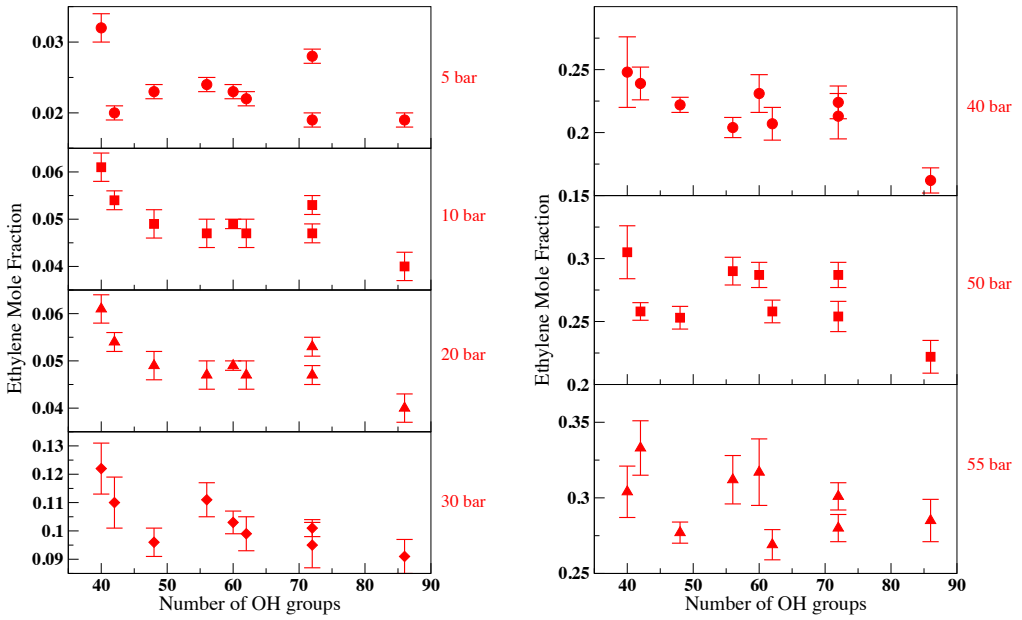

Figure 6.14: Dependence of "*pseudo*-hydrophobic" pore composition on number of OH groups. The specified external conditions are those of methanol/ethylene vapor-liquid equilibrium at 20°C and the indicated pressure.

simplicity and the fact that its self-diffusion coefficient agrees well with experiment. Preliminary calculations of the volumes and enthalpies of mixing in TraPPE-UA methanol–SPC/E water mixtures show good agreement with experiment. Hydrogen peroxide remains a challenge to accurately simulate within classical mechanics. Due to the complexity of the molecule, i.e., the presence of four lone pairs and a low torsional barrier, existing force fields range from a simple four-site model [120] to an 11-site fluctuating-charge model [121]. A number of ethylene oxide force fields have been developed [122, 123]. Taken together, the above molecular force fields should allow for classical modeling of the complex reaction media.

Chapter 7

Concluding remarks

Many intriguing phenomena in chemistry, biology, and materials science occur at condensed-phase interfaces. The study of basic properties of mixtures at interfaces contributes to new knowledge pertaining to the underlying atomistic nature of macroscopic phenomena. In this work, the thermodynamics, structure, phase behavior, and dynamics of a variety of mixtures are explored using molecular simulation.

Molecular dynamics (MD) was used to simulate a range of model binary hard-sphere mixtures confined between a pair of planar hard walls. Gibbs-Cahn Integration was used to calculate interfacial free energies γ using pressure, chemical potential, and adsorption measurements on the system. The contribution to γ from the differential adsorption is very small compared to that of the excess volume for all diameter ratios and mole fractions studied. At all but the highest densities, predictions from the White Bear Mark II classical density functional agree very

well with the MD results for pressure, chemical potential difference, interfacial excess volume, and interfacial free energy.

For the aluminum–gallium system, MD was used to prepare and simulate a planar solid–liquid interface at 368 K and 1 bar. The structural, thermodynamic, and transport properties of the interfaces for the (100), (110), and (111) crystal orientations were charaterized using density, potential energy, stress, and diffusion constant profiles. Two-dimensional Fourier analysis shows that the liquid prefreezes at the same lattice spacing as the corresponding solid substrate. This compression of the liquid Ga atoms results in moderate to large stress in the interfacial region.

In the filling of silica mesopores with methanol/ethylene mixtures, Monte Carlo (MC) techniques were used to determine vapor-liquid phase coexistence under experimental conditions of interest and subsequently to perform the filling of the pore. Ethylene and methanol molecular force fields were validated by using Gibbs Ensemble Monte Carlo (GEMC) to calculate pure and mixture vapor-liquid equilibria. The bulk methanol/ethylene mixtures were characterized by calculating volume expansion ratios, radial distribution functions, and translational diffusion coefficients. Grand Canonical Monte Carlo (GCMC) was used to fill model silica mesopores with the mixture at saturation conditions at 20°C and 5–55 bar. As in the bulk, the ethylene mole fraction of the confined phase increases as the hydrophobicity increases. At higher pressures, the composition within the pore also has a significant dependence on the number of silanol groups present, regardless of whether or not charges are included on the hydroxyl OH atoms.

Appendix A

Appendix

A.1 WBII excess volume and particle number

Fundamental-Measure Theory (FMT) has been used to generate accurate equations for thermodynamic quantities of hard-sphere (HS) systems; of interest here are the White Bear Mark II (WBII) equations [1–3]. These equations utilize the so-called scaled-particle or fundamental-measure variables for the fluid particle. For the binary hard-sphere system, these are $n_0 = \rho_1 + \rho_2 = \rho$, $n_1 = \frac{\sigma_1}{2}(\rho_1 + \alpha\rho_2)$, $n_2 = \pi\sigma_1^2\left(\rho_1 + \alpha^2\rho_2\right)$, $n_3 = \frac{\pi\sigma_1^3}{6}\left(\rho_1 + \alpha^3\rho_2\right) = \eta_1 + \eta_2 = \eta$. The WBII excess free-energy density functional of the bulk fluid is

$$\Phi_{\mathrm{WBII}} = -n_0\ln(1-n_3) + \frac{n_1 n_2(1+\frac{1}{3}\phi_2(n_3))}{1-n_3} + \frac{n_2^3(1-\frac{1}{3}\phi_3(n_3))}{24\pi(1-n_3)^2} \qquad \text{(A.1)}$$

where $\phi_2(n_3) = \frac{1}{n_3}(2n_3 - n_3^2 + 2(1-n_3)\ln(1-n_3))$ and $\phi_3(n_3) = \frac{1}{n_3^2}(2n_3 - 3n_3^2 + 2n_3^3 + 2(1-n_3)^2\ln(1-n_3))$. We compare our MD results for the interfacial free energy γ of the binary HS fluid mixture at a hard wall against the WBII prediction,

given by

$$\beta\gamma_{\mathrm{WBII}} = \frac{\partial\Phi}{\partial n_2} = \frac{n_1(1+\frac{1}{3}\phi_2(n_3))}{1-n_3} + \frac{n_2^2(1-\frac{1}{3}\phi_3(n_3))}{8\pi(1-n_3)^2} \tag{A.2}$$

or

$$\begin{aligned}\beta\sigma_1^2\gamma_{\mathrm{WBII}}(\eta,x_1,\alpha) =& \frac{3\eta(x_1+(1-x_1)\alpha)(1+\frac{1}{3}\phi_2(\eta))}{\pi(x_1+(1-x_1)\alpha^3)(1-\eta)} + \\ & \frac{9\eta^2(x_1+(1-x_1)\alpha^2)^2(1-\frac{1}{3}\phi_3(\eta))}{2\pi(x_1+(1-x_1)\alpha^3)^2(1-\eta)^2}\end{aligned}$$

In order to derive expressions for the WBII excess volume and particle number terms, we must first have the functions for γ, P, and $\Delta\mu$ in terms of α, x_1, and η.

The Carnahan-Starling Mark III (CSIII) equation of state [38] serves as the input pressure for the derivation of the WBII free energy density functional and is given by

$$\beta P_{\mathrm{CSIII}} = \frac{n_0}{1-n_3} + \frac{n_1 n_2(1+\frac{1}{3}n_3^2)}{(1-n_3)^2} + \frac{n_2^3(1-\frac{2}{3}n_3+\frac{1}{3}n_3^2)}{12\pi(1-n_3)^3} \tag{A.3}$$

or

$$\begin{aligned}\beta\sigma_1^3 P_{\mathrm{CSIII}}(\eta,x_1,\alpha) =& \frac{6\eta}{\pi(x_1+(1-x_1)\alpha^3)(1-\eta)} + \\ & \frac{18(1+\frac{1}{3}\eta^2)(x_1+(1-x_1)\alpha^2)(x_1+(1-x_1)\alpha)\eta^2}{\pi(1-\eta)^2(x_1+(1-x_1)\alpha^3)^2} + \\ & \frac{18(1-\frac{2}{3}\eta+\frac{1}{3}\eta^2)(x_1+(1-x_1)\alpha^2)^3\eta^3}{\pi(1-\eta)^3(x_1+(1-x_1)\alpha^3)^3}\end{aligned}$$

The WBII expression for chemical potential difference can be derived using

$$\beta\Delta\mu^{ex}_{\mathrm{WBII}} = \beta\mu^{ex}_1 - \beta\mu^{ex}_2 = \frac{\partial\Phi}{\partial\rho_1} - \frac{\partial\Phi}{\partial\rho_2} = \sum_{\alpha=0}^{3}\left[\frac{\partial\Phi}{\partial n_\alpha}\frac{\partial n_\alpha}{\partial\rho_1} - \frac{\partial\Phi}{\partial n_\alpha}\frac{\partial n_\alpha}{\partial\rho_2}\right]$$

$$\begin{aligned}\beta\Delta\mu^{ex}_{\mathrm{WBII}} \approx{}& \frac{\sigma_1}{2}(1-\alpha)\frac{n_2(1+\frac{1}{3}\phi_2(n_3))}{1-n_3}+\\ &\pi\sigma_1^2(1-\alpha^2)\left[\frac{n_1(1+\frac{1}{3}\phi_2(n_3))}{1-n_3}+n_2^2\frac{1-\frac{1}{3}\phi_3(n_3)}{8\pi(1-n_3)^2}\right]\\ &+\frac{\pi\sigma_1^3}{6}(1-\alpha^3)\left[\frac{n_0}{1-n_3}+\frac{n_1n_2(1+\frac{1}{3}n_3^2)}{(1-n_3)^2}+\frac{n_2^3(1-\frac{2}{3}n_3+\frac{1}{3}n_3^2)}{12\pi(1-n_3)^3}\right]\end{aligned}$$

or

$$\begin{aligned}\beta\Delta\mu^{ex}_{\mathrm{WBII}}(\eta,x_1,\alpha) \approx{}&(1-\alpha)\frac{3\eta(x_1+(1-x_1)\alpha^2)(1+\frac{1}{3}\phi_2(\eta))}{(x_1+(1-x_1)\alpha^3)(1-\eta)}+\\ &(1-\alpha^2)\left[\frac{3\eta(x_1+(1-x_1)\alpha)(1+\frac{1}{3}\phi_2(\eta))}{(x_1+(1-x_1)\alpha^3)(1-\eta)}+\right.\\ &\left.\frac{9\eta^2(x_1+(1-x_1)\alpha^2)^2(1-\frac{1}{3}\phi_3(\eta))}{2(x_1+(1-x_1)\alpha^3)^2(1-\eta)^2}\right]+\\ &(1-\alpha^3)\left[\frac{\eta}{(x_1+(1-x_1)\alpha^3)(1-\eta)}+\right.\\ &\frac{3(1+\frac{1}{3}\eta^2)(x_1+(1-x_1)\alpha^2)(x_1+(1-x_1)\alpha)\eta^2}{(1-\eta)^2(x_1+(1-x_1)\alpha^3)^2}+\\ &\left.\frac{3(1-\frac{2}{3}\eta+\frac{1}{3}\eta^2)(x_1+(1-x_1)\alpha^2)^3\eta^3}{(1-\eta)^3(x_1+(1-x_1)\alpha^3)^3}\right]\end{aligned}$$

where we have used βP_{CSIII} as an approximation for $\frac{\partial\Phi_{\mathrm{WBII}}}{\partial n_3}$

Given the functions for γ, P, and $\Delta\mu$ in terms of α, x_1, and η, one can derive the WBII equations for the interfacial excess volume

$$v_N = \left(\frac{\partial\gamma}{\partial P}\right)_{\Delta\mu} \approx \frac{\left(\frac{\partial\gamma}{\partial x_1}\right)_\eta - \left(\frac{\partial\gamma}{\partial\eta}\right)_{x_1}\left(\frac{\partial\Delta\mu}{\partial x_1}\right)_\eta \left(\frac{\partial\Delta\mu}{\partial\eta}\right)_{x_1}^{-1}}{\left(\frac{\partial P}{\partial x_1}\right)_\eta - \left(\frac{\partial P}{\partial\eta}\right)_{x_1}\left(\frac{\partial\Delta\mu}{\partial x_1}\right)_\eta \left(\frac{\partial\Delta\mu}{\partial\eta}\right)_{x_1}^{-1}} \tag{A.4}$$

and the interfacial excess particle number

$$\Gamma_{1|N} = -\left(\frac{\partial\gamma}{\partial\Delta\mu}\right)_P \approx -\frac{\left(\frac{\partial\gamma}{\partial x_1}\right)_\eta - \left(\frac{\partial\gamma}{\partial\eta}\right)_{x_1}\left(\frac{\partial P}{\partial x_1}\right)_\eta \left(\frac{\partial P}{\partial\eta}\right)_{x_1}^{-1}}{\left(\frac{\partial\Delta\mu}{\partial x_1}\right)_\eta - \left(\frac{\partial\Delta\mu}{\partial\eta}\right)_{x_1}\left(\frac{\partial P}{\partial x_1}\right)_\eta \left(\frac{\partial P}{\partial\eta}\right)_{x_1}^{-1}} \tag{A.5}$$

where the approximation is due to the approximation present in the equation used for $\Delta\mu$. For Eqs. (A.4) and (A.5), assume reduced units.

A.2 Interpolation error

Given a collection of N data points $\{(x_i, y_i, \delta y_i)\}$, suppose one wants to fit to the data a quadratic function $y(x) = c_1 + c_2 x + c_3 x^2$. One would ultimately like to use this fit to find y and δy at some $x \neq x_i$. The total deviation of the fit values from the real data squared—that is, the error ε—is given by

$$\varepsilon(c_1, c_2, c_3) = \sum_{i=1}^{N} \left(y(x_i) - y_i\right)^2 = \sum_{i=1}^{N} \left(c_1 + c_2 x_i + c_3 x_i^2 - y_i\right)^2. \tag{A.6}$$

The coefficients of the quadratic function that minimize the error can be found by solving

$$\begin{aligned}
\frac{\partial \varepsilon}{\partial c_1} &= \sum 2\left(c_1 + c_2 x_i + c_3 x_i^2 - y_i\right) \\
&= 2\left[N c_1 + c_2 \sum x_i + c_3 \sum x_i^2 - \sum y_i\right] = 0 \\
\frac{\partial \varepsilon}{\partial c_2} &= \sum 2x_i\left(c_1 + c_2 x_i + c_3 x_i^2 - y_i\right) \\
&= 2\left[c_1 \sum x_i + c_2 \sum x_i^2 + c_3 \sum x_i^3 - \sum x_i y_i\right] = 0 \\
\frac{\partial \varepsilon}{\partial c_3} &= \sum 2x_i^2\left(c_1 + c_2 x_i + c_3 x_i^2 - y_i\right) \\
&= 2\left[c_1 \sum x_i^2 + c_2 \sum x_i^3 + c_3 \sum x_i^4 - \sum x_i^2 y_i\right] = 0
\end{aligned} \tag{A.7}$$

where the summations remain from $i = 1$ to N. The simplified matrix representation of this system of equations $\mathbf{Ac} = \mathbf{b}$ is

$$\begin{pmatrix} N & \sum x_i & \sum x_i^2 \\ \sum x_i & \sum x_i^2 & \sum x_i^3 \\ \sum x_i^2 & \sum x_i^3 & \sum x_i^4 \end{pmatrix} \begin{pmatrix} c_1 \\ c_2 \\ c_3 \end{pmatrix} = \begin{pmatrix} \sum y_i \\ \sum x_i y_i \\ \sum x_i^2 y_i \end{pmatrix}. \tag{A.8}$$

The value of $y(x)$ can be given by the product of the vector $\begin{pmatrix} 1 & x & x^2 \end{pmatrix}$ with $\mathbf{c}$:

$$y = \begin{pmatrix} 1 & x & x^2 \end{pmatrix} \begin{pmatrix} c_1 \\ c_2 \\ c_3 \end{pmatrix} = \begin{pmatrix} 1 & x & x^2 \end{pmatrix} \mathbf{A}^{-1}\mathbf{b}. \tag{A.9}$$

Using x and the inverse matrix elements a_{jk}^{-1} to define $\omega_\alpha = a_{1\alpha}^{-1} + x a_{2\alpha}^{-1} + x^2 a_{3\alpha}^{-1}$

for $\alpha \in \{1,2,3\}$ yields

$$y = \sum \left(\omega_1 + \omega_2 x_i + \omega_3 x_i^2\right) y_i \tag{A.10}$$

and

$$\delta^2 y = \sum \left(\omega_1 + \omega_2 x_i + \omega_3 x_i^2\right)^2 \delta^2 y_i \tag{A.11}$$

for the interpolation value and error of y at some x.

A.3 Summary of interfacial free energy results for binary hard-sphere fluid/hard wall systems

Results from the simulations of binary hard-sphere mixtures at hard walls are summarized in the following tables.

Table A.1: Simulation results for $\alpha = 0.9$, $x_1 = 0.75$.

η	$P\sigma_1^3/k_BT$	v_N/σ_1	$\Delta\mu/k_BT$	$\Gamma_{1\|N}\sigma_1^2$	$\gamma\sigma_1^2/k_BT$
0.0	0.0	0.4875	$\ln(3) \approx 1.0986$	0.0	0.0
0.02356(3)	0.05307(4)	0.456(7)	1.1330(17)	–0.00050(17)	0.02503(19)
0.04705(4)	0.11678(5)	0.422(4)	1.1681(13)	–0.0008(3)	0.0530(3)
0.07047(4)	0.19311(7)	0.393(3)	1.2055(13)	–0.0014(5)	0.0842(4)
0.09384(5)	0.28444(7)	0.368(3)	1.2479(14)	–0.0018(5)	0.1190(4)
0.11714(5)	0.39345(9)	0.345(2)	1.2942(11)	–0.0019(6)	0.1579(5)
0.14040(6)	0.52367(10)	0.321(2)	1.3475(13)	–0.0020(8)	0.2014(5)
0.16363(6)	0.67895(13)	0.301(3)	1.4099(10)	–0.0025(6)	0.2499(7)
0.18678(5)	0.86411(9)	0.2807(18)	1.4764(11)	–0.0021(8)	0.3039(7)
0.20991(6)	1.08496(11)	0.2613(14)	1.5567(12)	–0.0030(12)	0.3640(8)
0.23303(8)	1.34848(14)	0.245(2)	1.6445(15)	–0.0021(15)	0.4310(10)
0.25607(7)	1.66293(14)	0.2264(18)	1.7479(14)	–0.0030(14)	0.5053(11)

0.27916(10)	2.03896(16)	0.2133(14)	1.8638(16)	–0.004(2)	0.5884(12)
0.30226(6)	2.48955(14)	0.2026(15)	1.9999(11)	–0.0033(15)	0.6826(14)
0.32523(7)	3.02928(19)	0.1893(14)	2.1509(12)	–0.0016(17)	0.7887(16)
0.34823(8)	3.67842(18)	0.1760(18)	2.3309(14)	–0.002(3)	0.9075(19)
0.37120(11)	4.4601(2)	0.165(2)	2.5416(19)	–0.001(4)	1.041(3)
0.39419(8)	5.4052(2)	0.1551(16)	2.7841(15)	–0.001(2)	1.192(3)
0.41716(10)	6.5510(2)	0.143(2)	3.072(2)	–0.002(5)	1.361(6)
0.44010(12)	7.9461(3)	0.131(2)	3.411(2)	–0.006(5)	1.556(5)
0.46293(18)	9.6502(4)	0.121(4)	3.809(3)	–0.001(10)	1.772(9)
0.47202(14)	10.435(4)	0.115(4)	3.984(2)	–0.00(3)	1.865(13)
0.48115(13)	11.290(5)	0.109(2)	4.183(3)	–0.009(10)	1.961(13)
0.49023(14)	12.217(7)	0.106(3)	4.390(3)	0.005(14)	2.061(14)
0.49926(16)	13.227(6)	0.101(4)	4.613(3)	0.005(15)	2.165(14)

Table A.2: Simulation results for $\alpha = 0.9$, $x_1 = 0.50$.

η	$P\sigma_1^3/k_BT$	v_N/σ_1	$\Delta\mu/k_BT$	$\Gamma_{1\|N}\sigma_1^2$	$\gamma\sigma_1^2/k_BT$
0.0	0.0	0.475	$\ln(1) = 0.0$	0.0	0.0
0.02184(3)	0.05268(4)	0.445(7)	0.0361(4)	–0.00061(18)	0.02425(18)
0.04360(3)	0.11504(5)	0.414(4)	0.0651(3)	–0.0010(2)	0.0510(3)
0.06533(5)	0.18882(7)	0.392(3)	0.1024(3)	–0.0017(4)	0.0808(4)
0.08699(5)	0.27592(6)	0.367(3)	0.1412(3)	–0.0021(8)	0.1139(4)
0.10861(4)	0.37866(8)	0.344(3)	0.1865(4)	–0.0024(7)	0.1505(5)
0.13020(6)	0.49979(12)	0.322(2)	0.2366(4)	–0.0030(9)	0.1910(6)
0.15175(6)	0.64248(10)	0.305(2)	0.2895(4)	–0.0024(6)	0.2358(7)
0.17327(7)	0.81040(15)	0.285(2)	0.3545(3)	–0.0030(14)	0.2855(7)
0.19472(8)	1.00791(12)	0.2672(17)	0.4250(4)	–0.0031(17)	0.3403(8)
0.21613(6)	1.24059(11)	0.2502(19)	0.5058(3)	–0.0028(8)	0.4008(9)
0.23756(9)	1.51471(11)	0.2337(16)	0.5955(5)	–0.004(3)	0.4674(10)
0.25896(8)	1.83792(15)	0.2208(17)	0.6984(5)	–0.004(3)	0.5413(12)
0.28035(9)	2.21941(16)	0.2072(16)	0.8132(4)	–0.003(3)	0.6233(13)

0.30173(7)	2.67004(16)	0.1951(12)	0.9472(6)	–0.005(3)	0.7145(15)
0.32303(10)	3.20339(19)	0.1841(16)	1.0963(6)	–0.001(3)	0.8161(17)
0.34441(8)	3.8358(2)	0.1727(15)	1.2710(9)	–0.002(4)	0.929(2)
0.36569(7)	4.58713(15)	0.1645(12)	1.4690(6)	–0.002(4)	1.056(2)
0.38702(13)	5.4819(3)	0.154(2)	1.7005(10)	–0.001(4)	1.199(3)
0.40838(11)	6.5516(3)	0.142(2)	1.9717(6)	–0.011(4)	1.359(4)
0.42962(15)	7.8321(3)	0.131(3)	2.2817(9)	–0.006(6)	1.536(5)
0.43811(16)	8.4139(4)	0.127(3)	2.4214(15)	–0.009(9)	1.612(6)
0.44658(15)	9.0414(4)	0.124(3)	2.5655(8)	–0.002(10)	1.692(7)
0.45511(15)	9.7172(4)	0.120(3)	2.7230(15)	–0.010(9)	1.775(7)
0.46358(11)	10.447(3)	0.117(2)	2.8904(9)	–0.003(9)	1.863(7)
0.47187(18)	11.214(6)	0.112(3)	3.0584(17)	–0.002(6)	1.952(8)
0.48049(14)	12.054(5)	0.108(3)	3.2380(13)	–0.002(6)	2.044(8)
0.49318(10)	13.455(3)	0.103(2)	3.5532(13)	–0.005(7)	2.194(9)
0.5058(2)	15.048(7)	0.099(6)	3.904(3)	–0.00(2)	2.356(11)

Table A.3: Simulation results for $\alpha = 0.9$, $x_1 = 0.25$.

η	$P\sigma_1^3/k_BT$	v_N/σ_1	$\Delta\mu/k_BT$	$\Gamma_{1\|N}\sigma_1^2$	$\gamma\sigma_1^2/k_BT$
0.0	0.0	0.4625	$\ln(\frac{1}{3}) \approx -1.0986$	0.0	0.0
0.02011(2)	0.05228(3)	0.436(5)	–1.0668(12)	–0.00046(9)	0.02350(13)
0.04021(3)	0.11350(5)	0.412(4)	–1.0337(12)	–0.0008(2)	0.0495(2)
0.06021(3)	0.18477(6)	0.388(3)	–0.9982(9)	–0.0014(3)	0.0780(3)
0.08019(5)	0.26797(6)	0.361(3)	–0.9588(13)	–0.0020(4)	0.1092(4)
0.10010(5)	0.36482(9)	0.343(2)	–0.9197(12)	–0.0020(8)	0.1434(4)
0.11998(5)	0.47757(8)	0.3232(16)	–0.8747(11)	–0.0017(6)	0.1811(5)
0.13987(4)	0.60882(8)	0.306(2)	–0.8238(9)	–0.0016(8)	0.2224(5)
0.15969(6)	0.76127(11)	0.287(3)	–0.7646(10)	–0.004(3)	0.2677(7)
0.17951(8)	0.93856(10)	0.273(2)	–0.7015(15)	–0.0031(10)	0.3176(8)
0.19933(7)	1.14487(13)	0.2578(18)	–0.6282(12)	–0.0027(16)	0.3726(8)
0.21900(8)	1.38401(14)	0.2414(16)	–0.5505(13)	–0.0036(12)	0.4325(9)
0.23877(7)	1.66274(15)	0.2300(18)	–0.4619(12)	–0.0022(14)	0.4984(10)
0.25851(9)	1.98718(16)	0.2150(14)	–0.3584(14)	–0.0019(14)	0.5709(11)
0.27821(8)	2.36480(18)	0.2025(14)	–0.2445(12)	–0.004(3)	0.6502(13)
0.29787(10)	2.80553(17)	0.1933(14)	–0.1199(15)	–0.005(2)	0.7377(14)

0.31758(9)	3.31960(17)	0.1825(16)	0.0280(13)	–0.001(3)	0.8346(17)
0.33724(9)	3.9214(2)	0.1746(16)	0.1878(13)	–0.003(3)	0.943(2)
0.35685(9)	4.62561(19)	0.1643(17)	0.3730(13)	–0.004(4)	1.063(2)
0.37653(12)	5.4529(3)	0.151(2)	0.5919(16)	–0.004(6)	1.194(3)
0.39619(10)	6.4259(3)	0.1426(19)	0.8361(14)	–0.006(6)	1.339(4)
0.41184(13)	7.3284(3)	0.137(2)	1.0516(18)	–0.007(5)	1.466(5)
0.41973(10)	7.8271(3)	0.134(2)	1.1751(13)	–0.004(9)	1.534(5)
0.42754(10)	8.3605(3)	0.130(2)	1.3008(15)	–0.003(6)	1.605(5)
0.43532(13)	8.9121(3)	0.127(3)	1.4255(18)	–0.010(9)	1.677(6)
0.44315(12)	9.5204(5)	0.123(3)	1.5643(16)	–0.000(16)	1.753(6)
0.45102(9)	10.1723(5)	0.120(3)	1.715(2)	–0.008(6)	1.833(7)
0.46251(11)	11.2390(5)	0.115(2)	1.9551(19)	–0.000(14)	1.959(7)
0.47461(8)	12.4253(5)	0.109(3)	2.2271(15)	–0.008(9)	2.094(8)
0.48213(16)	13.2879(5)	0.106(3)	2.417(2)	–0.007(12)	2.188(10)
0.48994(16)	14.2149(6)	0.102(4)	2.619(2)	–0.009(13)	2.286(11)
0.49779(11)	15.2132(6)	0.098(3)	2.8391(19)	–0.014(10)	2.388(11)

Table A.4: Simulation results for $\alpha = 0.8$, $x_1 = 0.75$.

η	$P\sigma_1^3/k_BT$	v_N/σ_1	$\Delta\mu/k_BT$	$\Gamma_{1\|N}\sigma_1^2$	$\gamma\sigma_1^2/k_BT$
0.0	0.0	0.475	1.0986	0.0	0.0
0.02219(4)	0.05274(3)	0.447(6)	1.1612(14)	–0.00075(15)	0.02432(15)
0.04431(6)	0.11527(6)	0.416(3)	1.2229(13)	–0.0014(3)	0.0514(2)
0.06637(6)	0.18928(6)	0.389(4)	1.2917(12)	–0.0024(4)	0.0813(4)
0.08837(7)	0.27685(10)	0.364(4)	1.3691(12)	–0.0029(5)	0.1144(5)
0.11032(6)	0.38031(11)	0.340(3)	1.4507(11)	–0.0033(4)	0.1511(5)
0.13227(8)	0.50265(10)	0.322(3)	1.5447(12)	–0.0032(9)	0.1919(6)
0.15412(10)	0.64670(11)	0.299(2)	1.6528(15)	–0.0046(11)	0.2370(7)
0.17596(9)	0.81677(12)	0.281(2)	1.7724(13)	–0.0048(9)	0.2870(8)
0.19775(10)	1.01732(11)	0.2637(18)	1.9062(13)	–0.0043(12)	0.3414(18)
0.21954(10)	1.25394(12)	0.245(2)	2.0600(13)	–0.0065(13)	0.4032(10)
0.24129(10)	1.5335(2)	0.232(2)	2.2295(12)	–0.0052(14)	0.4710(12)
0.26302(10)	1.86361(16)	0.219(2)	2.4221(15)	–0.004(2)	0.5464(14)
0.28475(14)	2.2545(2)	0.205(2)	2.6455(17)	–0.005(3)	0.6303(17)

0.30643(12)	2.7171(2)	0.194(2)	2.8964(15)	–0.005(2)	0.724(2)
0.32813(17)	3.2663(2)	0.179(2)	3.189(2)	–0.007(3)	0.828(2)
0.34973(17)	3.9190(2)	0.170(3)	3.516(2)	–0.004(3)	0.943(3)
0.37144(15)	4.6976(3)	0.161(2)	3.898(2)	–0.005(4)	1.073(4)
0.3931(2)	5.6275(3)	0.149(4)	4.338(3)	–0.004(7)	1.219(6)
0.41472(19)	6.7430(3)	0.140(3)	4.849(4)	–0.006(5)	1.384(7)
0.43633(19)	8.0845(4)	0.132(3)	5.456(4)	–0.008(6)	1.571(9)
0.4449(2)	8.6959(4)	0.130(4)	5.717(4)	–0.002(8)	1.653(10)
0.4536(2)	9.3567(5)	0.126(4)	6.003(6)	–0.001(8)	1.738(10)
0.46221(19)	10.0704(4)	0.123(4)	6.303(7)	–0.004(8)	1.827(11)
0.4708(2)	10.8426(4)	0.121(4)	6.629(7)	–0.001(9)	1.923(12)
0.47945(17)	11.6469(5)	0.119(6)	6.937(9)	–0.002(11)	2.020(13)
0.4881(3)	12.5500(10)	0.117(6)	7.315(14)	0.011(17)	2.124(15)
0.4968(2)	13.5300(7)	0.114(4)	7.699(13)	0.027(13)	2.230(17)
0.5055(2)	14.5950(10)	0.110(6)	8.131(16)	0.012(12)	2.341(17)

Table A.5: Simulation results for $\alpha = 0.8$, $x_1 = 0.50$.

η	$P\sigma_1^3/k_BT$	v_N/σ_1	$\Delta\mu/k_BT$	$\Gamma_{1\|N}\sigma_1^2$	$\gamma\sigma_1^2/k_BT$
0.0	0.0	0.45	0.0	0.0	0.0
0.01910(4)	0.05200(4)	0.427(3)	0.0633(5)	–0.00121(15)	0.02283(9)
0.03814(5)	0.11216(4)	0.401(4)	0.1197(4)	–0.0023(2)	0.0478(2)
0.05712(7)	0.18174(6)	0.378(4)	0.1793(4)	–0.0028(4)	0.0751(3)
0.07610(6)	0.26212(7)	0.359(3)	0.2486(4)	–0.0043(4)	0.1050(4)
0.09498(7)	0.35478(9)	0.336(2)	0.3232(4)	–0.0047(6)	0.1375(5)
0.11391(9)	0.46192(8)	0.320(2)	0.4066(5)	–0.0057(8)	0.1730(5)
0.13274(9)	0.58513(13)	0.300(2)	0.4976(5)	–0.0066(12)	0.2118(6)
0.15158(10)	0.72747(12)	0.285(2)	0.5966(6)	–0.0065(12)	0.2540(7)
0.17038(8)	0.89124(13)	0.268(2)	0.7097(6)	–0.0080(11)	0.3002(8)
0.18918(10)	1.08010(16)	0.254(2)	0.8337(5)	–0.0085(16)	0.3505(9)
0.20792(11)	1.29779(14)	0.2421(19)	0.9702(6)	–0.0080(18)	0.4057(10)
0.22664(12)	1.54850(16)	0.228(2)	1.1227(7)	–0.009(2)	0.4659(12)
0.24535(19)	1.8380(2)	0.216(3)	1.2916(7)	–0.007(3)	0.5316(15)
0.2641(2)	2.1721(3)	0.203(3)	1.4835(11)	–0.010(3)	0.6035(19)

0.28281(15)	2.5584(2)	0.194(3)	1.6956(10)	–0.010(2)	0.682(2)
0.30149(12)	3.0048(2)	0.1834(19)	1.9332(11)	–0.010(3)	0.769(2)
0.32014(17)	3.5222(3)	0.176(3)	2.1972(13)	–0.008(5)	0.864(3)
0.33882(17)	4.1216(2)	0.164(2)	2.5012(11)	–0.011(4)	0.969(3)
0.3574(2)	4.8186(4)	0.157(3)	2.8372(13)	–0.006(7)	1.084(5)
0.37607(11)	5.6292(4)	0.1478(19)	3.2223(12)	–0.013(3)	1.211(5)
0.3835(2)	5.9899(4)	0.146(3)	3.390(2)	–0.007(6)	1.266(6)
0.3910(3)	6.3741(6)	0.141(3)	3.5629(16)	–0.003(8)	1.322(6)
0.3984(3)	6.7828(5)	0.138(4)	3.7507(19)	–0.005(9)	1.380(6)
0.4059(2)	7.2183(4)	0.134(4)	3.947(3)	–0.009(8)	1.440(7)
0.4206(3)	8.1600(6)	0.129(5)	4.354(3)	–0.011(10)	1.568(8)
0.4354(3)	9.2447(4)	0.126(5)	4.821(4)	–0.007(9)	1.711(10)
0.4503(2)	10.4822(6)	0.121(4)	5.344(5)	–0.004(8)	1.866(12)
0.4652(3)	11.8942(8)	0.118(6)	5.937(7)	–0.004(12)	2.037(16)
0.4801(3)	13.5143(8)	0.114(4)	6.591(8)	–0.008(11)	2.229(18)
0.4949(2)	15.3781(6)	0.113(3)	7.336(14)	0.019(9)	2.437(19)

Table A.6: Simulation results for $\alpha = 0.8$, $x_1 = 0.25$.

η	$P\sigma_1^3/k_BT$	v_N/σ_1	$\Delta\mu/k_BT$	$\Gamma_{1\|N}\sigma_1^2$	$\gamma\sigma_1^2/k_BT$
0.0	0.0	0.425	–1.0986	0.0	0.0
0.01601(4)	0.05136(5)	0.408(4)	–1.0409(14)	–0.00079(13)	0.02141(13)
0.03195(4)	0.10928(6)	0.384(3)	–0.9877(10)	–0.0019(2)	0.0444(2)
0.04789(5)	0.17490(6)	0.368(2)	–0.9329(11)	–0.0022(3)	0.0692(3)
0.06377(6)	0.24881(9)	0.348(4)	–0.8700(10)	–0.0032(6)	0.0958(4)
0.07966(7)	0.33241(9)	0.335(3)	–0.8037(10)	–0.0040(6)	0.1246(4)
0.09548(6)	0.42659(8)	0.318(3)	–0.7344(9)	–0.0040(4)	0.1556(5)
0.11135(11)	0.53275(11)	0.304(3)	–0.6521(15)	–0.0058(9)	0.1890(6)
0.12715(10)	0.65238(11)	0.288(3)	–0.5653(12)	–0.0063(9)	0.2249(6)
0.14296(10)	0.78742(14)	0.277(2)	–0.4748(12)	–0.0066(11)	0.2636(7)
0.15870(9)	0.93931(13)	0.2651(15)	–0.3764(10)	–0.0054(13)	0.3054(7)
0.17445(10)	1.11025(18)	0.252(2)	–0.2658(10)	–0.0059(14)	0.3503(8)
0.19019(9)	1.30284(14)	0.2399(15)	–0.1448(10)	–0.0066(13)	0.3984(9)
0.20592(11)	1.52011(18)	0.2302(17)	–0.0135(11)	–0.0071(18)	0.4504(10)
0.22164(12)	1.76470(16)	0.2192(2)	0.1313(12)	–0.0076(19)	0.5064(11)
0.23734(12)	2.0405(2)	0.2108(18)	0.2877(11)	–0.0066(16)	0.5668(13)
0.25307(16)	2.3515(3)	0.198(2)	0.4631(14)	–0.010(2)	0.6318(15)
0.26867(14)	2.7025(3)	0.192(2)	0.6490(13)	–0.005(3)	0.7016(17)

0.28437(16)	3.0988(3)	0.184(2)	0.8570(14)	–0.006(3)	0.777(2)
0.30005(14)	3.5464(3)	0.175(2)	1.0882(13)	–0.008(3)	0.859(2)
0.31572(13)	4.0526(3)	0.1662(17)	1.3436(15)	–0.008(3)	0.948(2)
0.3219(2)	4.2730(4)	0.163(3)	1.4498(17)	–0.007(5)	0.985(3)
0.32822(12)	4.5057(3)	0.1610(18)	1.5634(13)	–0.008(3)	1.023(3)
0.33444(13)	4.7491(3)	0.159(3)	1.6801(13)	–0.006(4)	1.063(3)
0.34073(15)	5.0058(3)	0.157(2)	1.8045(12)	–0.005(4)	1.104(3)
0.3594(2)	5.8503(5)	0.148(3)	2.197(2)	–0.008(6)	1.235(4)
0.3780(2)	6.8401(5)	0.139(2)	2.647(2)	–0.002(6)	1.380(5)
0.3980(3)	8.0712(8)	0.129(4)	3.123(3)	–0.011(7)	1.548(7)
0.40930(18)	8.8737(5)	0.125(3)	3.546(3)	–0.012(6)	1.654(8)
0.4192(4)	9.6387(10)	0.122(6)	3.783(4)	–0.013(11)	1.752(10)
0.4289(4)	10.4519(11)	0.120(4)	4.121(5)	–0.004(9)	1.853(11)
0.4404(3)	11.5276(7)	0.115(3)	4.667(5)	–0.000(11)	1.981(12)
0.4587(4)	13.4500(11)	0.111(6)	5.332(8)	–0.000(13)	2.199(17)
0.4733(5)	15.2149(12)	0.102(8)	6.025(9)	–0.014(16)	2.39(3)
0.4887(4)	17.3700(11)	0.095(7)	6.853(16)	–0.018(15)	2.62(3)
0.4984(4)	18.8823(11)	0.093(8)	7.45(2)	–0.022(16)	2.77(3)

Table A.7: Simulation results for $\alpha = 0.7$, $x_1 = 0.75$.

η	$P\sigma_1^3/k_BT$	v_N/σ_1	$\Delta\mu/k_BT$	$\Gamma_{1\|N}\sigma_1^2$	$\gamma\sigma_1^2/k_BT$
0.0	0.0	0.4625	1.0986	0.0	0.0
0.02115(6)	0.05245(5)	0.434(6)	1.1928(17)	–0.00141(14)	0.02358(17)
0.04223(5)	0.11411(7)	0.409(5)	1.2725(12)	–0.0024(3)	0.0497(3)
0.06326(8)	0.18631(10)	0.381(4)	1.3677(12)	–0.0037(3)	0.0785(4)
0.08418(9)	0.27082(9)	0.358(3)	1.4694(15)	–0.0045(4)	0.1102(5)
0.10515(10)	0.37001(10)	0.340(3)	1.5819(13)	–0.0055(5)	0.1453(6)
0.12600(8)	0.48579(9)	0.317(3)	1.7076(12)	–0.0061(8)	0.1840(6)
0.14680(9)	0.62112(11)	0.2965(17)	1.8471(15)	–0.0066(6)	0.2264(7)
0.16758(13)	0.77941(13)	0.279(2)	2.0015(14)	–0.0070(11)	0.2730(8)
0.18831(16)	0.96426(18)	0.2610(16)	2.1786(16)	–0.0083(11)	0.3243(8)
0.20910(13)	1.1807(2)	0.2461(18)	2.3718(17)	–0.0087(8)	0.3809(9)
0.22979(15)	1.4335(2)	0.233(3)	2.5926(16)	–0.0088(18)	0.4433(12)

0.25042(15)	1.7292(2)	0.217(2)	2.8393(19)	–0.0098(18)	0.5121(14)
0.27114(19)	2.0761(3)	0.207(3)	3.1129(13)	–0.011(2)	0.5884(18)
0.2917(2)	2.4830(3)	0.194(3)	3.428(2)	–0.010(3)	0.673(2)
0.31234(18)	2.9605(3)	0.182(3)	3.7799(19)	–0.009(3)	0.766(3)
0.33296(19)	3.5224(3)	0.174(2)	4.183(3)	–0.007(3)	0.869(3)
0.3535(3)	4.1846(4)	0.163(3)	4.644(4)	–0.008(5)	0.985(4)
0.3741(2)	4.9673(4)	0.152(4)	5.162(4)	–0.007(5)	1.112(6)
0.39473(16)	5.8937(3)	0.142(3)	5.771(5)	–0.012(4)	1.254(7)
0.4152(4)	6.9944(7)	0.133(5)	6.453(6)	–0.004(6)	1.411(9)
0.4358(2)	8.3073(5)	0.126(4)	7.259(11)	–0.011(6)	1.587(11)
0.4563(3)	9.8768(7)	0.118(5)	8.17(2)	–0.010(7)	1.788(15)
0.4768(5)	11.7657(9)	0.113(8)	9.28(3)	–0.008(12)	2.02(2)
0.4972(3)	14.0527(9)	0.111(4)	10.55(5)	0.021(9)	2.26(2)

Table A.8: Simulation results for $\alpha = 0.7$, $x_1 = 0.50$.

η	$P\sigma_1^3/k_BT$	v_N/σ_1	$\Delta\mu/k_BT$	$\Gamma_{1\|N}\sigma_1^2$	$\gamma\sigma_1^2/k_BT$
0.0	0.0	0.425	0.0	0.0	0.0
0.01695(5)	0.05139(4)	0.400(4)	0.0841(5)	–0.00150(10)	0.02127(10)
0.03387(8)	0.10974(5)	0.382(4)	0.1587(3)	–0.0034(2)	0.0443(2)
0.05076(8)	0.17592(7)	0.362(2)	0.2417(5)	–0.0053(3)	0.0693(3)
0.06761(9)	0.25107(7)	0.3463(19)	0.3281(3)	–0.0065(5)	0.0964(3)
0.08440(8)	0.33616(8)	0.327(3)	0.4226(5)	–0.0072(5)	0.1257(4)
0.10124(11)	0.43272(9)	0.311(2)	0.5276(5)	–0.0090(8)	0.1573(5)
0.11799(10)	0.54200(10)	0.2976(17)	0.6407(6)	–0.0099(10)	0.1916(5)
0.13473(7)	0.66577(12)	0.2834(14)	0.7628(7)	–0.0101(4)	0.2288(5)
0.15141(13)	0.80576(13)	0.267(2)	0.8986(7)	–0.0114(13)	0.2688(6)
0.16811(15)	0.96462(15)	0.2564(16)	1.0442(6)	–0.0113(12)	0.3120(7)
0.18478(14)	1.1443(2)	0.244(3)	1.2054(6)	–0.0117(13)	0.3588(8)
0.20150(12)	1.34804(18)	0.231(2)	1.3842(5)	–0.0137(16)	0.4094(10)
0.21810(18)	1.5787(2)	0.219(2)	1.5775(9)	–0.014(2)	0.4640(11)
0.23479(19)	1.8405(3)	0.210(2)	1.7901(10)	–0.014(3)	0.5230(14)
0.2514(2)	2.1373(3)	0.198(2)	2.0258(11)	–0.016(3)	0.5870(17)
0.2680(2)	2.4741(3)	0.189(3)	2.2831(11)	–0.015(3)	0.656(2)

0.2846(2)	2.8569(4)	0.181(3)	2.5699(13)	–0.014(2)	0.731(2)
0.3012(2)	3.2918(4)	0.171(3)	2.8846(16)	–0.017(4)	0.813(3)
0.3177(2)	3.7871(4)	0.166(3)	3.2321(15)	–0.012(3)	0.901(3)
0.3344(3)	4.3516(5)	0.155(5)	3.6204(18)	–0.016(5)	0.997(5)
0.3410(2)	4.5985(4)	0.151(3)	3.787(2)	–0.016(4)	1.037(5)
0.3476(2)	4.8598(5)	0.149(3)	3.961(2)	–0.013(5)	1.079(5)
0.35426(15)	5.1350(3)	0.147(3)	4.143(2)	–0.015(4)	1.123(5)
0.3609(2)	5.4253(5)	0.142(4)	4.331(3)	–0.017(5)	1.168(5)
0.3739(4)	6.0466(7)	0.139(5)	4.721(3)	–0.012(8)	1.260(6)
0.3872(4)	6.7463(8)	0.134(3)	5.167(5)	–0.016(7)	1.362(7)
0.4003(3)	7.5280(6)	0.126(3)	5.642(6)	–0.006(6)	1.469(8)
0.4170(3)	8.6350(8)	0.119(4)	6.316(7)	–0.022(6)	1.614(10)
0.4334(4)	9.9097(8)	0.115(5)	7.076(7)	–0.017(7)	1.777(12)
0.4500(4)	11.3835(9)	0.111(5)	7.927(15)	–0.024(11)	1.961(17)
0.4665(5)	13.0906(10)	0.108(6)	8.88(3)	–0.010(12)	2.16(2)
0.4831(3)	15.0703(8)	0.104(3)	9.99(5)	–0.030(8)	2.40(2)
0.5004(8)	17.507(2)	0.102(6)	11.5(2)	–0.003(18)	2.67(3)

Table A.9: Simulation results for $\alpha = 0.7$, $x_1 = 0.25$.

η	$P\sigma_1^3/k_BT$	v_N/σ_1	$\Delta\mu/k_BT$	$\Gamma_{1\|N}\sigma_1^2$	$\gamma\sigma_1^2/k_BT$
0.0	0.0	0.3875	–1.0986	0.0	0.0
0.01280(7)	0.05054(4)	0.374(6)	–1.0196(18)	–0.00135(12)	0.01929(14)
0.02557(7)	0.10616(6)	0.360(4)	–0.9540(13)	–0.0025(3)	0.0398(3)
0.03833(7)	0.16740(5)	0.344(3)	–0.8838(11)	–0.0039(4)	0.0616(3)
0.05104(11)	0.23463(10)	0.329(2)	–0.8096(16)	–0.0049(6)	0.0846(3)
0.06377(6)	0.30868(10)	0.319(2)	–0.7285(8)	–0.0062(6)	0.1090(4)
0.07647(11)	0.39007(16)	0.305(3)	–0.6420(11)	–0.0074(9)	0.1350(4)
0.08912(10)	0.47957(12)	0.2952(16)	–0.5539(11)	–0.0073(10)	0.1625(5)
0.10183(9)	0.57791(15)	0.2831(16)	–0.4544(9)	–0.0091(8)	0.1917(5)
0.11443(13)	0.68590(17)	0.2727(17)	–0.3533(12)	–0.0084(9)	0.2226(5)
0.12710(13)	0.80441(19)	0.2623(15)	–0.2405(12)	–0.0104(15)	0.2554(6)
0.13970(17)	0.9347(2)	0.2516(15)	–0.1221(14)	–0.0108(16)	0.2901(6)
0.15232(12)	1.07791(19)	0.244(2)	0.0040(10)	–0.0107(18)	0.3270(8)
0.16495(17)	1.2351(3)	0.235(3)	0.1412(13)	–0.013(2)	0.3662(9)
0.17752(16)	1.4078(3)	0.227(3)	0.2857(13)	–0.011(2)	0.4077(10)
0.1901(2)	1.5977(3)	0.219(3)	0.4415(16)	–0.012(3)	0.4519(12)
0.20268(16)	1.8057(3)	0.209(2)	0.6115(11)	–0.0146(16)	0.4986(13)
0.2153(2)	2.0350(3)	0.202(3)	0.7915(13)	–0.013(3)	0.5482(16)
0.2278(2)	2.2867(4)	0.196(3)	0.9837(16)	–0.014(3)	0.6009(19)

0.24033(18)	2.5630(4)	0.188(3)	1.1921(12)	–0.013(3)	0.657(2)
0.2529(2)	2.8676(5)	0.180(3)	1.4162(14)	–0.015(4)	0.716(2)
0.2654(3)	3.2020(6)	0.172(4)	1.6583(18)	–0.015(5)	0.778(3)
0.2779(2)	3.5710(5)	0.169(2)	1.9168(17)	–0.012(4)	0.845(3)
0.2904(2)	3.9766(5)	0.163(4)	2.197(2)	–0.013(5)	0.915(4)
0.30298(18)	4.4241(5)	0.1574(18)	2.5036(16)	–0.017(4)	0.992(4)
0.3154(2)	4.9173(6)	0.152(3)	2.8287(19)	–0.012(5)	1.073(5)
0.3280(2)	5.4615(5)	0.147(3)	3.185(3)	–0.013(5)	1.159(5)
0.3405(3)	6.0623(7)	0.141(4)	3.574(3)	–0.013(7)	1.250(6)
0.3530(3)	6.7267(8)	0.135(4)	3.990(3)	–0.014(6)	1.348(7)
0.3723(5)	7.887(13)	0.127(6)	4.407(8)	–0.012(8)	1.505(9)
0.3898(4)	9.1018(11)	0.119(3)	5.101(5)	–0.021(5)	1.666(11)
0.4041(6)	10.2570(19)	0.112(5)	5.731(10)	–0.018(5)	1.812(13)
0.4192(7)	11.654(2)	0.108(3)	6.468(16)	–0.010(8)	1.976(14)
0.4337(6)	13.1407(17)	0.107(7)	7.25(3)	–0.014(9)	2.145(18)
0.4481(9)	14.824(3)	0.103(9)	8.13(5)	–0.013(14)	2.34(3)
0.4636(7)	16.879(2)	0.098(5)	9.09(6)	–0.028(12)	2.56(3)
0.4787(8)	19.236(3)	0.095(6)	10.27(12)	–0.011(13)	2.81(4)
0.4943(7)	21.952(2)	0.085(11)	11.6(3)	–0.031(14)	3.08(4)

A.4 Silica mesopore structures

Top-down and inside views of the ten mesopore structures are shown in Figs. A.1–A.10. The silica (yellow) and oxygen (red) atom locations are indicated by a colored surface, and silanol hydrogen (blue) sites are indicated by spheres. Due to the surface roughness, not all silanol groups are visible in these visualizations. All pores have a depth of 30 Å and cross-sectional area of 44 Å $\times$ 44 Å.

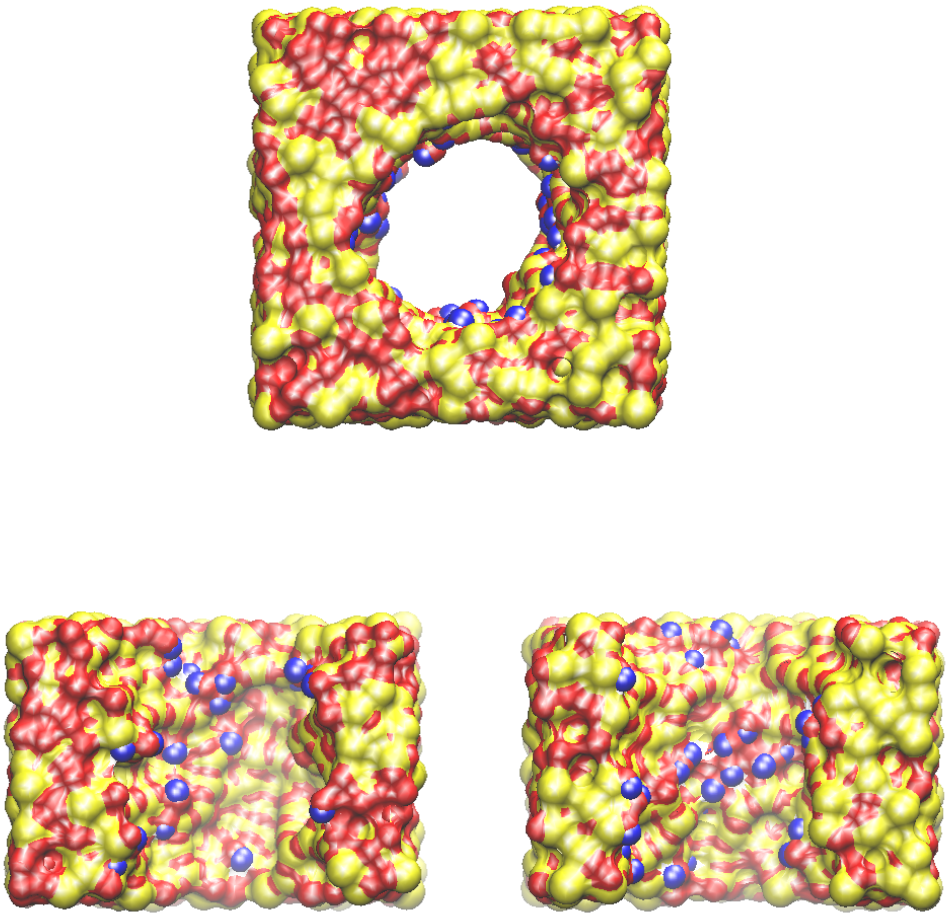

Figure A.1: Visualization of silica pore #01.

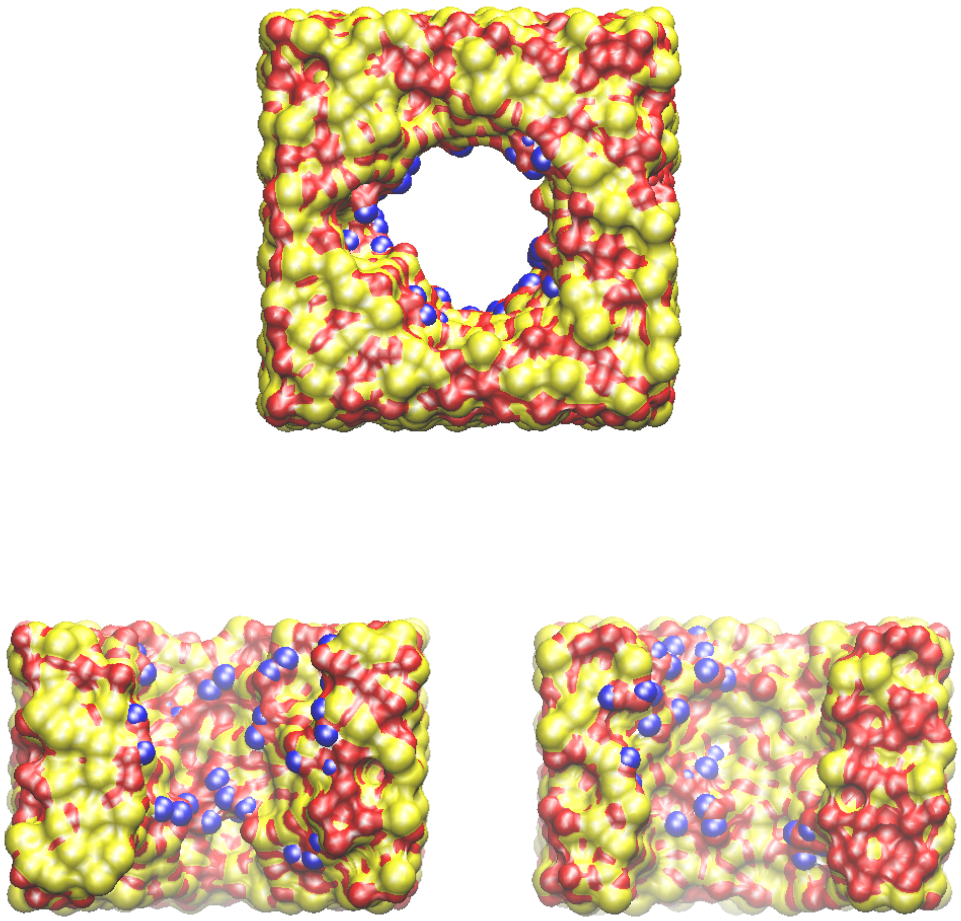

Figure A.2: Visualization of silica pore #02.

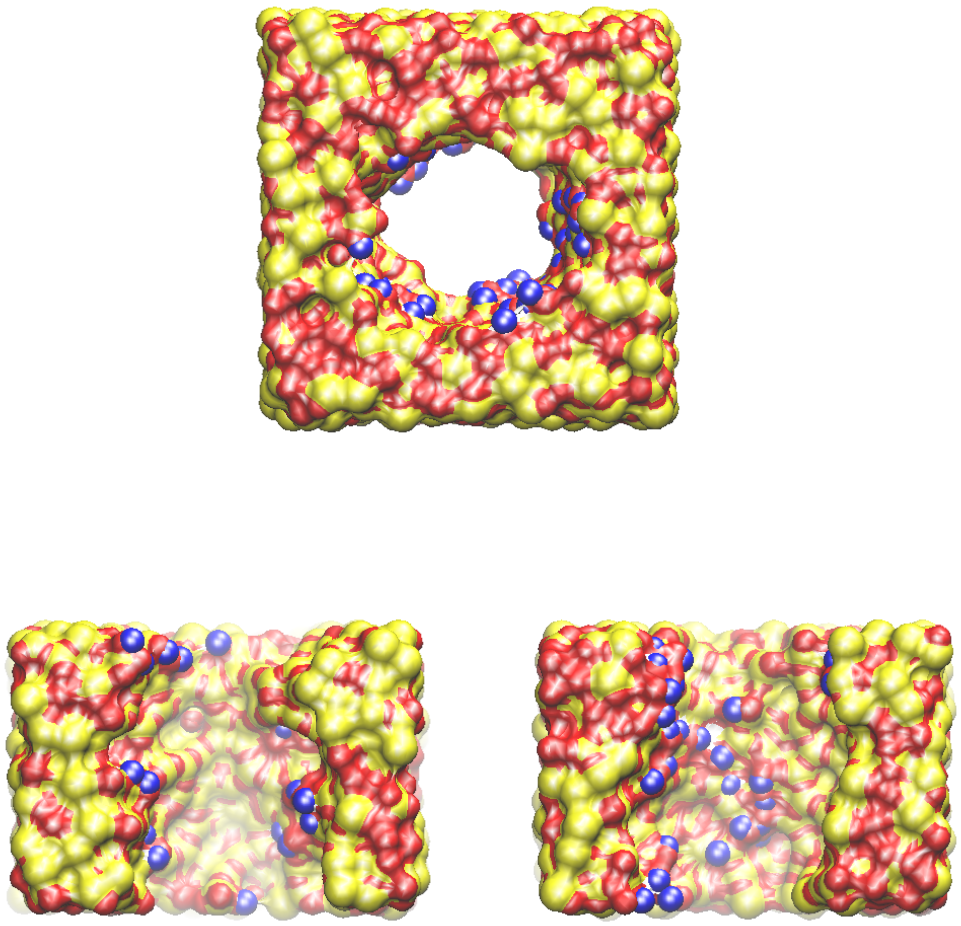

Figure A.3: Visualization of silica pore #03.

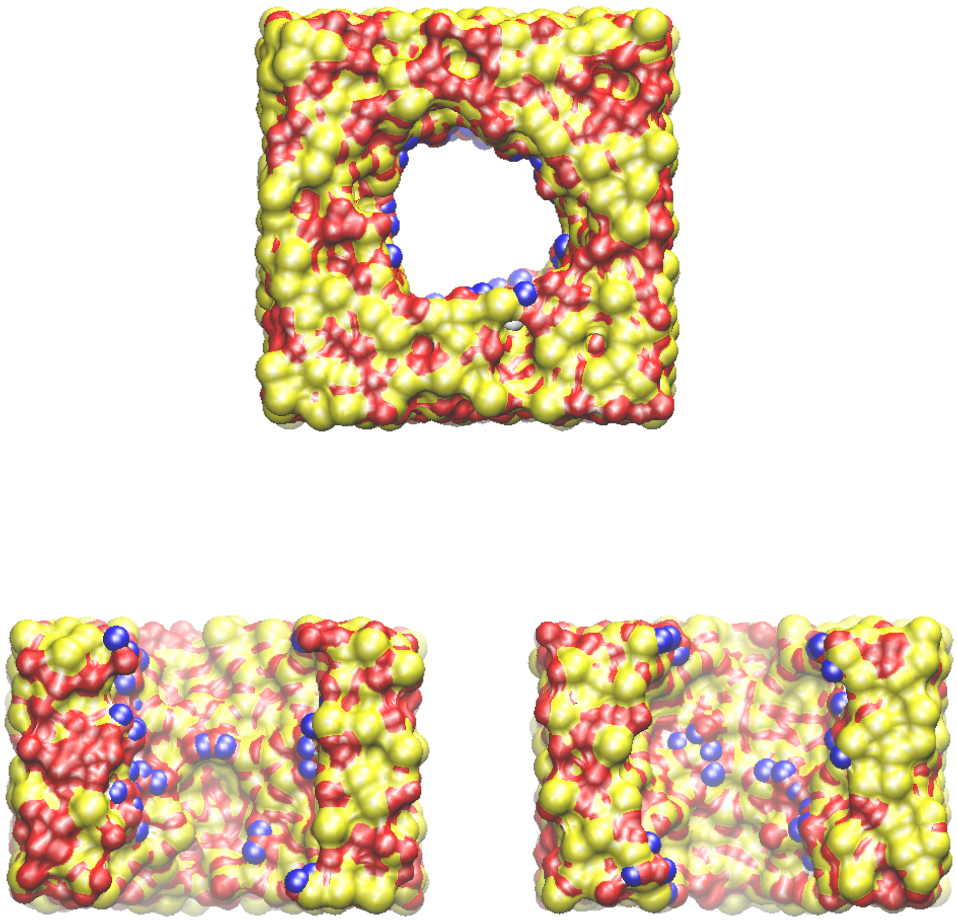

Figure A.4: Visualization of silica pore #04.

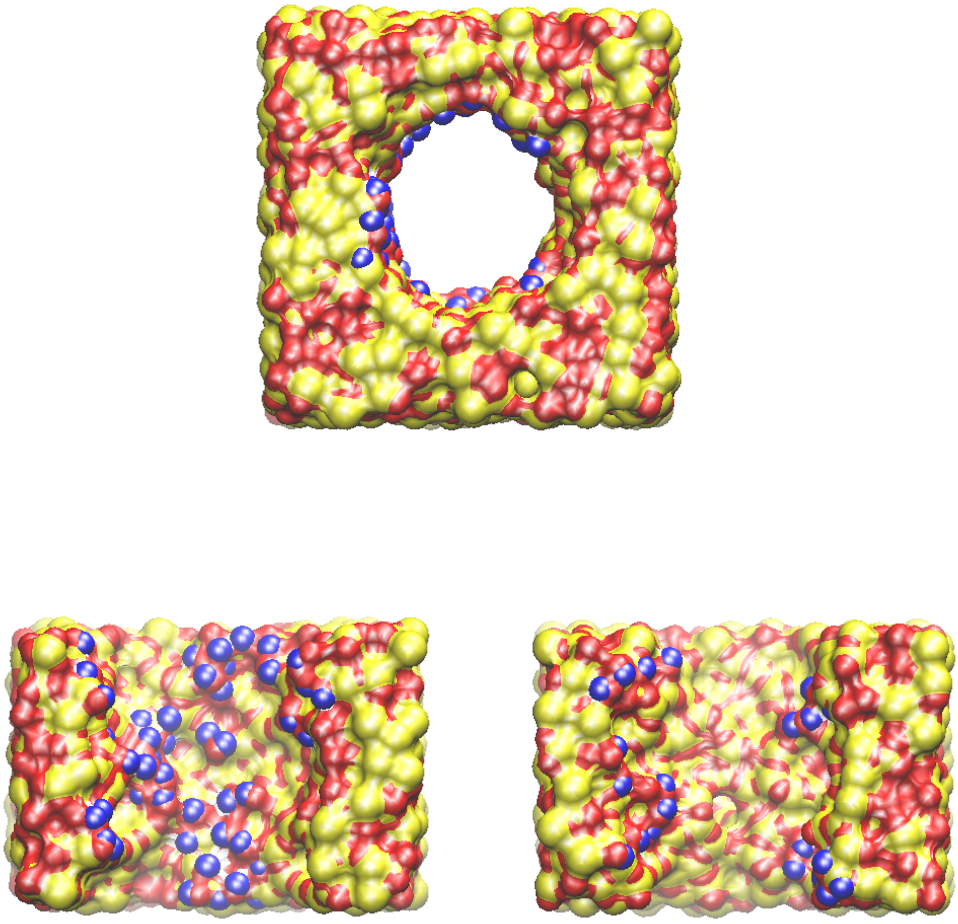

Figure A.5: Visualization of silica pore #05.

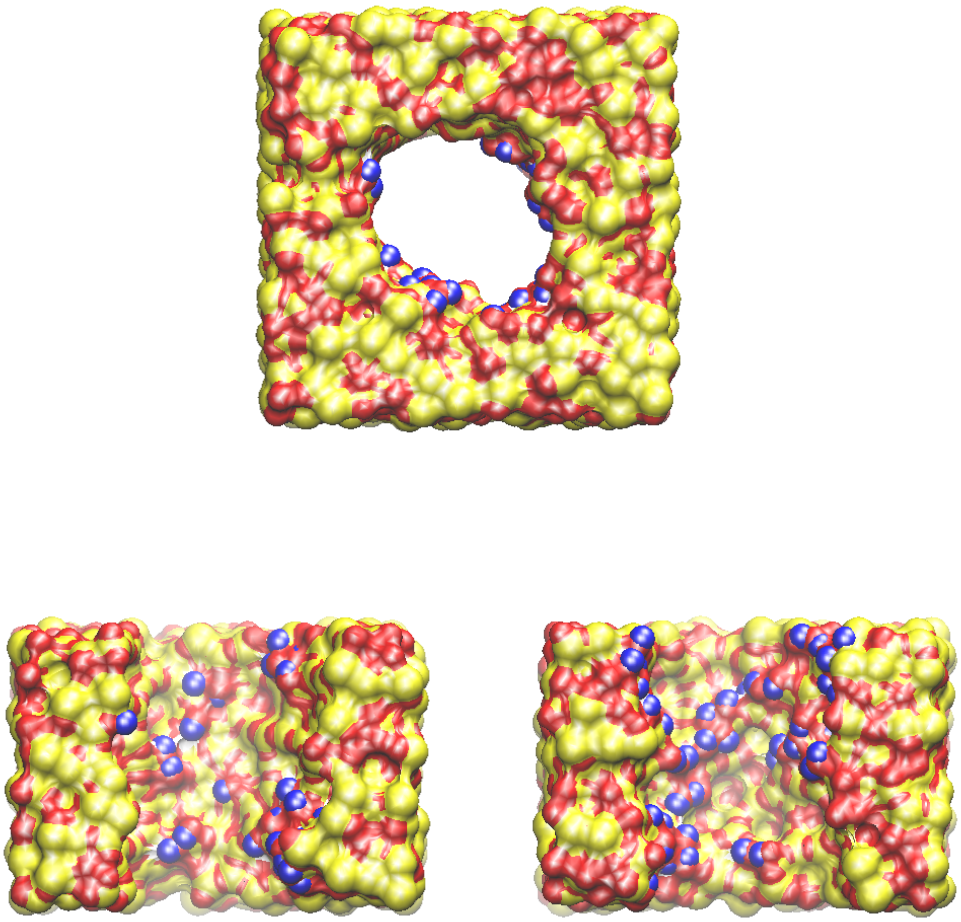

Figure A.6: Visualization of silica pore #06.

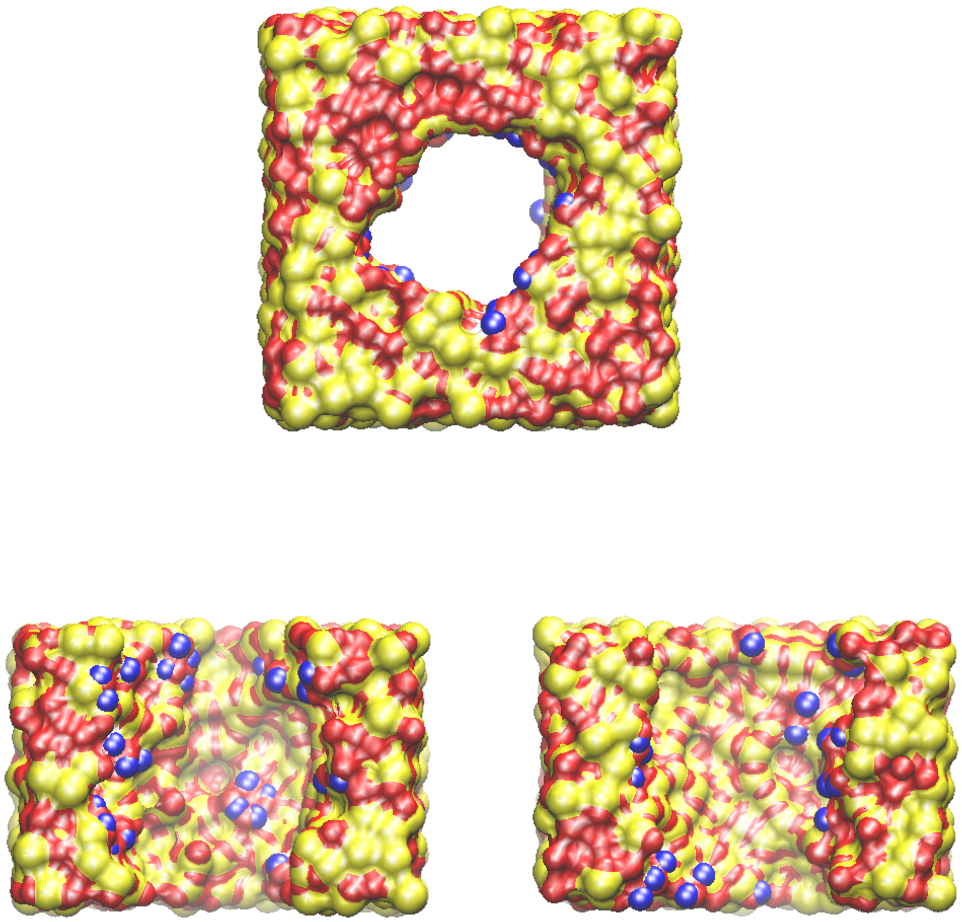

Figure A.7: Visualization of silica pore #07.

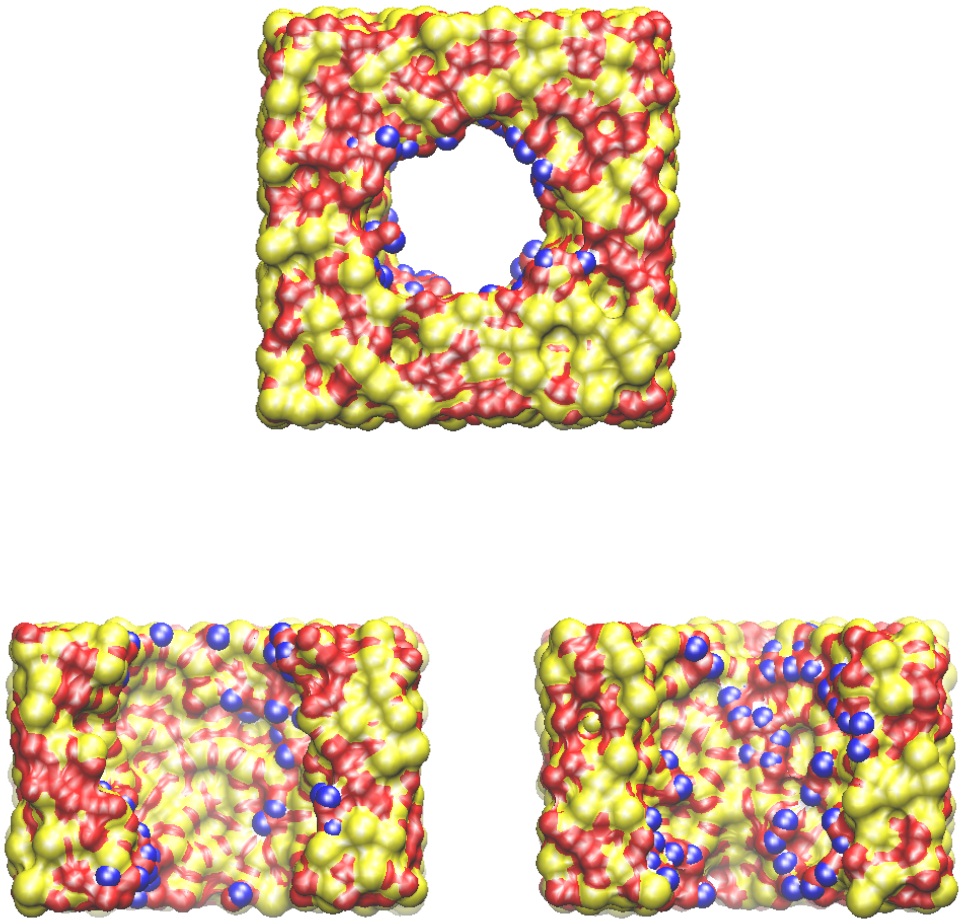

Figure A.8: Visualization of silica pore #08.

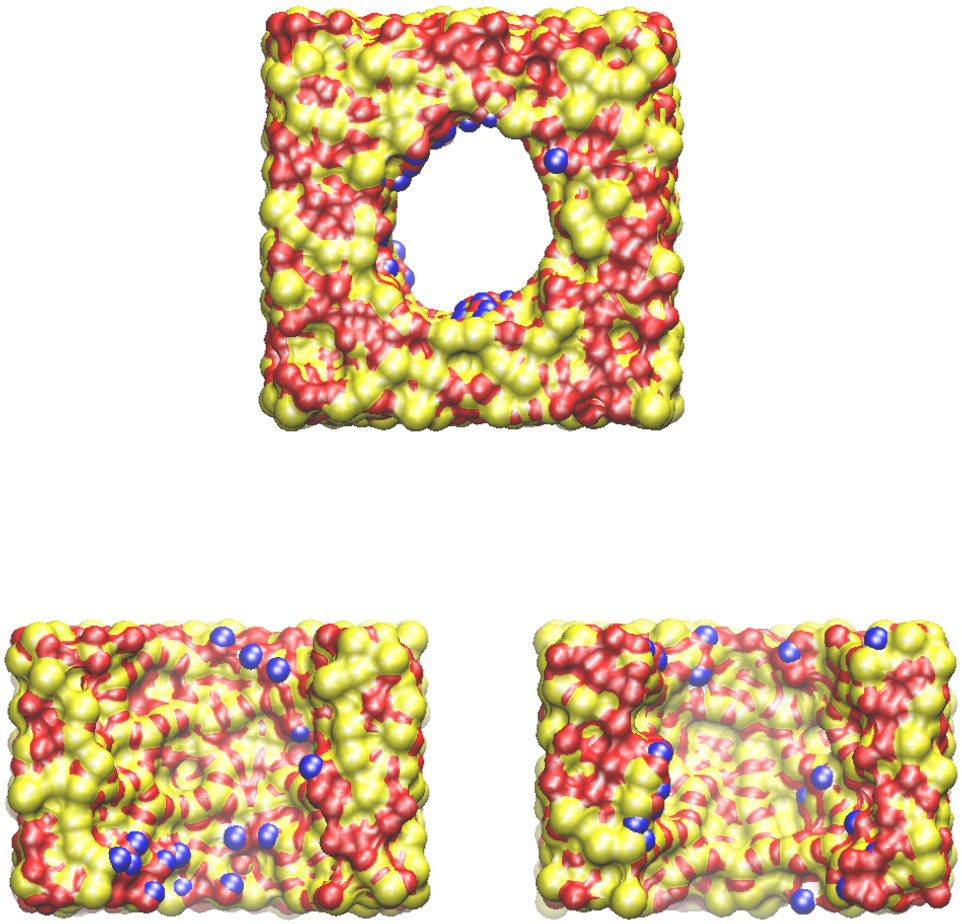

Figure A.9: Visualization of silica pore #09.

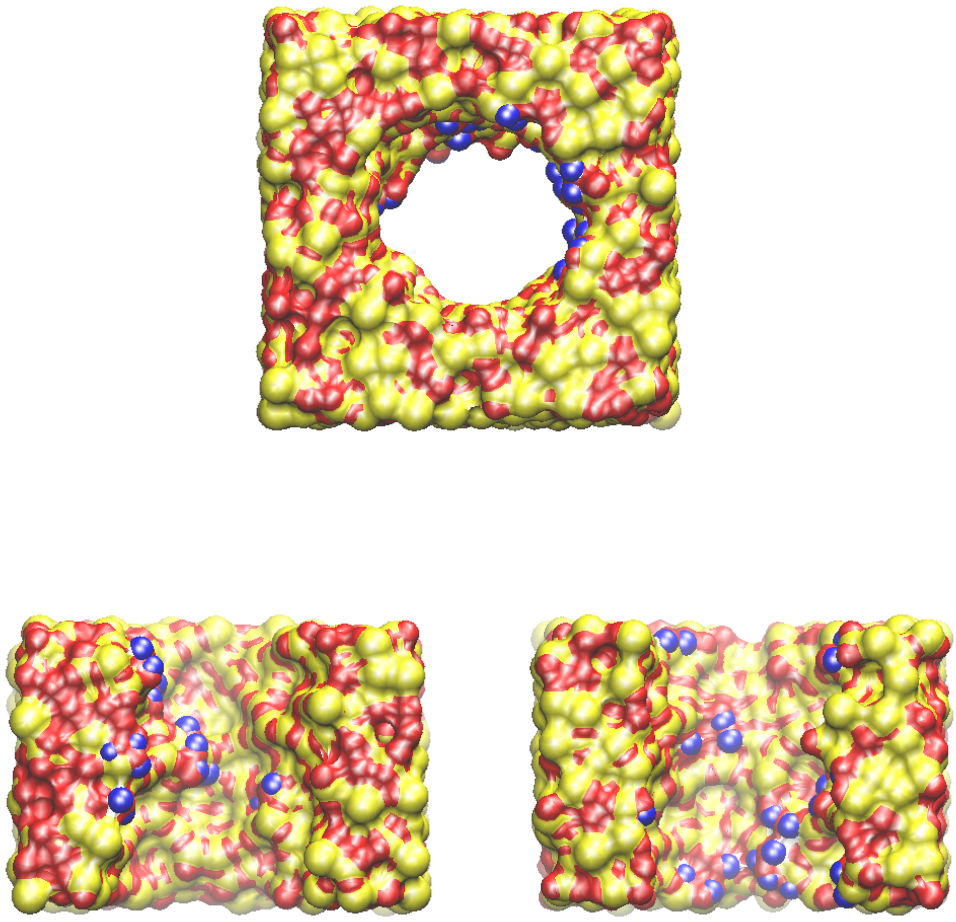

Figure A.10: Visualization of silica pore #10.

Bibliography

[1] E. Pereiro-López, W. Ludwig, D. Bellet, and C. Lemaignan, Acta Mater. **54**, 4307–4316 (2006).

[2] C. Roques-Carmes, M. Aucouturier, and P. Lacombe, Can. Met. Qtly. **13**, 115 (1974).

[3] M.G. Nicholas and C.F. Old, J. Mater. Sci. **14**, 1–18 (1979).

[4] A. Ramanathan, B. Subramaniam, D. Badloe, U. Hanefeld, and R. Maheswari, J. Porous Mater. **19**, 961–968 (2012).

[5] M.A. Allen and D.J. Tildesley, *Computer Simulation of Liquids*, (Oxford Science Press, Oxford, 1987).

[6] D. Frenkel and B. Smit, *Understanding Molecular Simulation, 2nd Ed.*, (Academic Press, New York, 2002).

[7] D.C. Rapaport, *The Art of Molecular Dynamics Simulation*, (Cambridge University Press, New York, 2nd edition, 2004).

[8] B.J. Alder and T.E. Wainwright, J. Chem. Phys. **27**, 1208–1209 (1957).

[9] Steve Plimpton, J. Comput. Phys. **117**, 1 – 19 (1995).

[10] M.E. Tuckerman, *Statistical Mechanics: Theory and Molecular Simulation*, (Oxford University Press, New York, 2010).

[11] W.C. Swope, H.C. Andersen, P.H. Berens, and K.R. Wilson, J. Chem. Phys. **76**, 637 (1982).

[12] S. Nosé and M.L. Klein, Mol. Phys. **50**, 1055 (1983).

[13] S. Nosé, J. Chem. Phys. **81**, 511 (1984).

[14] W.G. Hoover, Phys. Rev. A **31**, 1695 (1985).

[15] S.D. Bond, B.J. Leimkuhler, and B.B. Laird, J. Comp. Phys. **151**, 114 (1999).

[16] H.C. Andersen, J. Chem. Phys. **72**, 2384 (1980).

[17] G.J. Martyna, M.L. Klein, and M. Tuckerman, J. Chem. Phys. **97**, 2635 (1992).

[18] G.J. Martyna, D.J. Tobias, and M.L. Klein, J. Chem. Phys. **101**, 4177 (1994).

[19] D.E. Knuth. Fundamental algorithms. In *The Art of Computer Programming*, volume 1., Addison-Wesley, Reading, MA, 1968.

[20] D.E. Knuth. Sorting and searching. In *The Art of Computer Programming*, volume 3., Addison-Wesley, Reading, MA, 1973.

[21] N. Metropolis and S. Ulam, J. Am. Stat. Assoc. **44**, 335–341 (1949).

[22] N. Metropolis, A.W. Rosenbluth, M.N. Rosenbluth, A.H. Teller, and E. Teller, J. Chem. Phys. **21**, 1087–1092 (1953).

[23] D.J. Adams, Mol. Phys. **28**, 1241–1252 (1974).

[24] D.J. Adams, Mol. Phys. **29**, 307–311 (1975).

[25] A.Z Panagiotopoulos, Mol. Phys. **61**, 813 (1987).

[26] A.Z Panagiotopoulos, N. Quirke, M. Stapleton, and D.J. Tildesley, Mol. Phys. **63**, 527 (1988).

[27] J.W. Gibbs, *On the equilibrium of heterogeneous substances*, New Haven, 1876).

[28] M.G. Martin, Mol. Simulat. **39**, 1212–1222 (2013).

[29] B.B. Laird and R.L. Davidchack, J. Chem. Phys. **132**, 204101 (6 pages) (2010).

[30] B.B. Laird, A. Hunter, and R.L. Davidchack, Phys. Rev. E **86**, 060602 (2012).

[31] T. Frolov and Y. Mishin, Phys. Rev. B **79**, 045430 (2009).

[32] T. Frolov and Y. Mishin, J. Chem. Phys **131**, 054702 (2009).

[33] B.B. Laird, R.L. Davidchack, Y. Yang, and M. Asta, J. Chem. Phys. **131**, 114110 (8 pages) (2009).

[34] J.L. Kern and B.B. Laird, J. Chem. Phys. **140**, 024703 (2014).

[35] V.D. Nguyen, Z. Hu, and P. Schall, Phys. Rev. E **84**, 011607 (2011).

[36] P. Hohenberg and W. Kohn, Phys. Rev. **136**, B864–B871 (1964).

[37] R. Evans, Adv. Phys. **28**, 143–200 (1979).

[38] H. Hansen-Goos and R. Roth, J. Stat. Phys.: Condens. Matter **18**, 8413 (2006).

[39] H. Reiss, H.L. Frisch, E. Helfand, and J.L. Lebowitz, J. Chem. Phys. **32**, 119 (1960).

[40] E. Helfand J.L. Lebowitz and E. Praestgaard, J. Chem. Phys. **43**, 774–779 (1965).

[41] J.R. Henderson and F. van Swol, Mol. Phys. **51**, 991 (1984).

[42] M. Heni and H. Löwen, Phys. Rev. E **60**, 7057–7065 (1999).

[43] A. Fortini and M. Dijkstra, J. Phys.: Condens. Matter 18 (2006).

[44] D. Deb, D. Wilms, A. Winkler, P. Virnau, and K. Binder, Int. J. Mod. Phys. C **23**, 1240011 (2012).

[45] E. De Miguel and G. Jackson, Mol. Phys. **104(22-24)**, 3717–3734 (2006).

[46] B.B. Laird and R.L. Davidchack, J. Phys. Chem. C **111**, 15952–15956 (2007).

[47] Y. Rosenfeld, Phys. Rev. Lett. **63**, 980–983 (1989).

[48] R. Roth, R. Evans, A. Lang, and G. Kahl, J. Stat. Phys.: Condens. Matter **14**, 12063 (2002).

[49] A.R. Denton and N.W. Ashcroft, Phys. Rev. A **44**, 8242–8248 (1991).

[50] R. Roth and S. Dietrich, Phys. Rev. E **62**, 6926–6936 (2000).

[51] R. Roth, J. Phys.: Condens. Matter **22**, 063102 (2010).

[52] J.P. Noworyta, D. Henderson, and S. Sokolowski, Mol. Phys. **95**, 415 (1998).

[53] Z. Tan, U.M.B. Marconi, F. van Swol, and K.E. Gubbins, J. Chem. Phys. **90**, 3704–3712 (1989).

[54] J.W. Cahn. Thermodynamics of solid and fluid surfaces. In W.C. Johnson and J.M. Blakely, editors, *Interfacial Segregation*, pages 3–23., ASM International, International Materials Park, OH, 1979.

[55] J.W. Gibbs, *The Collected Works*, volume 1, (Yale University Press, New Haven, 1957).

[56] B.B. Laird, J. Chem. Phys. **115**, 2889–2888 (2001).

[57] W.A. Tiller, *The Science of Crystallization: Microscopic Interfacial Phenomena*, (Cambridge University Press, New York, 1991).

[58] W.G.T. Kranendonk and D. Frenkel, Mol. Phys. **3**, 679–697 (1991).

[59] X. Cottin and P.A. Monson, J. Chem. Phys. **107**, 6855 – 6858 (1997).

[60] S. Punnathanam and P.A. Monson, J. Chem. Phys. **125**, 24508:1–8 (2006).

[61] B. Widom, J. Chem. Phys. 39 (1963).

[62] P. Sindzingre, G. Ciccotti, C. Massobrio, and D. Frenkel, Chem. Phys. Lett. **136**, 35–41 (1987).

[63] D.M. Heyes, Chem. Phys. **159**, 149–167 (1992).

[64] G.A. Mansoori, N.F. Carnahan, K.E. Starling, and T.W. Leland Jr., J. Chem. Phys. 54 (1971).

[65] R. Sibug-Aga and B.B. Laird, Phys. Rev. B **66**, e410 (2002).

[66] J.W. Perram, J. Comp. Phys. **58**, 409–416 (1985).

[67] M. Marechal and H. Löwen, Phys. Rev. Lett. **110**, 137801 (2013).

[68] A. Isihara, J. Chem. Phys. **19**, 397 (1951).

[69] M. Dennison, K. Milinković, and M. Dijkstra, J. Chem. Phys. **137**, 044507 (2012).

[70] W.D. Kaplan and Y. Kauffman, Annu. Rev. Mater. Res. **36**, 1–48 (2006).

[71] P. Geysermans, D. Gorse, and V. Pontikis, J. Chem. Phys. **113**, 6382 (2000).

[72] J. Pablo Palafox-Hernandez, Brian B. Laird, and Mark Asta, Acta Mater. **59(8)**, 3137 – 3144 (2011).

[73] Y. Yang, D.L. Olmsted, M. Asta, and B.B. Laird, Acta Mater. **60**, 4960–4971 (2012).

[74] Y. Yang, M. Asta, and B.B. Laird, Phys. Rev. Lett. **110**, 096102 (2013).

[75] A.K. Huntington, J. Inst. Metals **11**, 108 (1914).

[76] W. Ludwig, D. Bellet, J. Teyssier, J. Ouillier, N. Marie, K. Wolski, A. Simionovici, and C. Rau, J. Phys. IV **12**, 289–298 (2002).

[77] W. Ludwig, E. Pereiro-López, and D. Bellet, Acta Mater. **53**, 151–162 (2005).

[78] H.-S. Nam and D.J. Srolovitz, Phys. Rev. B **76**, 184114 (2007).

[79] H.-S. Nam, M.I. Mendelev, and D.J. Srolovitz, Phys. Rev. B **75**, 014204 (2006).

[80] H. Reichert, O. Klein, H. Dosch, M. Denk, V. Honkimäki, and T. Lippmann, Nature **408**, 839 (2000).

[81] W.J. Huisman, J.F. Peters, M.J. Zwanenburg, S.A. de Vries, T.E. Derry, D. Abernathy, and J.F. van der Veen, Nature **390**, 379–381 (1997).

[82] D. Kaminski, P. Poodt, E. Aret, N. Radenovic, and E. Vlieg, Phys. Rev. Lett. **96**, 056102 (2002).

[83] H.-S. Nam and D.J. Srolovitz, PRL **99**, 025501 (2007).

[84] R.L. Davidchack and B.B. Laird, J. Chem. Phys. **108**, 9452 (1998).

[85] N. W. Ashcroft and D. N. Mermin, *Solid State Physics*, (Thomson Learning, Toronto, 1976).

[86] S. W. Sides, G. S. Grest, and M. D. Lacasse, Phys. Rev. E **60**, 6708 (1999).

[87] R. Ishikawa, R. Mishra, A.R. Lupini, S.D. Findlay, T. Taniguchi, S.T. Pantelides, and S.J. Pennycook, Phys. Rev. Lett. **113**, 155501 (2014).

[88] M. Ghanta, T. Ruddy, D. Fahey, D. Busch, and B. Subramaniam, Ind. Eng. Chem. Res. **52**, 18–29 (2012).

[89] P.G. Jessop and B. Subramaniam, Chem. Rev. **107**, 2666–2694 (2007).

[90] B. Subramaniam, Coord. Chem. Rev. **254**, 1843–1853 (2010).

[91] M. Ghanta, B. Subramaniam, H.-J. Lee, and D. H. Busch, AIChE J. **59**, 180–187 (2013).

[92] W. Yan, A. Ramanathan, M. Ghanta, and B. Subramaniam, Catal. Sci. Technol. **4**, 4433–4439 (2014).

[93] R.C. Reid, J.M. Prausnitz, and B.E. Poling, *The Properties of Gases and Liquids*, (McGraw-Hill, New York, 4th edition, 1987).

[94] B. Chen, J.J. Potoff, and J.I. Siepmann, J. Phys. Chem. B **105**, 3093–3104 (2001).

[95] H.A. Lorentz, Annalen der Physik **12**, 127–136 (1881).

[96] D. Berthelot, Comptes rendus hebdomadaires des séances de l'Académie des Sciences **126**, 1703–1855 (1898).

[97] W.W. Wood and F.R. Parker, J. Chem. Phys. **27**, 720 (1955).

[98] C.D. Wick, M.G. Martin, and J.I. Siepmann, J. Phys. Chem. B **104**, 8008–8016 (2000).

[99] S.L. Weitz and J.J. Potoff, Fluid Phase Equilibr. **234**, 144–150 (2005).

[100] C.G. Gray and K.E. Gubbins, *Theory of Molecular Fluids: Fundamentals, Vol. I*, (Clarendon Press, Oxford, 1984).

[101] T.S. Gulmen and W.H. Thompson, Mater. Res. Soc. Symp. Proc. **899E**, 1–10 (2005).

[102] T.S. Gulmen and W.H. Thompson, Langmuir **22**, 10919–10923 (2006).

[103] T.S. Gulmen and W.H. Thompson, Langmuir **25**, 1103–1111 (2009).

[104] C.M. Morales and W.H. Thompson, J. Phys. Chem. **113**, 1922âĹŠ–1933 (2009).

[105] C.D. Norton and W.H. Thompson, J. Phys. Chem. C **117**, 19107âĹŠ–19114 (2013).

[106] A.A. Vartia and W.H. Thompson, J. Phys. Chem. B **116**, 5414–5424 (2012).

[107] A. Brodka and T.W. Zerda, J. Chem. Phys. **104**, 6319–6326 (1996).

[108] B.D. Smith and R. Srivastava, *Thermodynamic data for pure compounds: Part A, Hydrocarbons and ketones*, (Elsevier, Amsterdam, 1986).

[109] B.D. Smith and R. Srivastava, *Thermodynamic data for pure compounds: Part B, Halogenated hydrocarbons and alcohols*, (Elsevier, Amsterdam, 1986).

[110] K. Ohgaki, H. Nishii, T. Saito, and T. Katayama, J. Chem. Eng. Jpn. **16**, 263–267 (1983).

[111] T.F. Miller, M. Eleftheriou, P. Pattnaik, A. Ndirango, D. Newns, and G. J. Martyna, J. Chem. Phys. **116**, 8649 (2002).

[112] D.Y. Peng and D.B. Robinson, Indust. and Engr. Chemistry: Fundamentals **15**, 59 (1976).

[113] H.-J. Lee, M. Ghanta, D.H. Busch, and B. Subramaniam, Chem. Eng. Sci. **65**, 128–134 (2010).

[114] W.H. Press, S.A. Teukolsky, W.T. Vetterling, and B.P. Flannery, *Numerical Recipes in Fortran*, (Cambridge University Press,, New York, 1992).

[115] Y. Houndonougbo, H. Jin, B. Rajagopalan, K. Wong, K. Kuczera, B. Subramaniam, and B. Laird, J. Phys. Chem. B **110**, 13195–13202 (2006).

[116] Y. Houndonougbo, J.-X. Guo, G.H. Lushington, and B. Laird, Mol. Phys. **104**, 2955–2960 (2006).

[117] D. Laage and J.T. Hynes, Science **311**, 832–835 (2006).

[118] D. Laage and J.T. Hynes, J. Phys. Chem. B **112**, 14230–14242 (2008).

[119] H.J.C. Berendsen, J.R. Grigera, and T.P. Straatsma, J. Phys. Chem. **91**, 6269–6271 (1987).

[120] R. Vácha and P. Slavíček and M. Mucha and B.J. Finlayson-Pitts and P. Jungwirth, J. Phys. Chem. A **108**, 11573–11579 (2004).

[121] C.-Y. Yu and Z.-Z. Yang, J. Phys. Chem. A **115**, 2615–2626 (2011).

[122] M.-B.H. Ketko, J. Rafferty, J.I. Siepmann, and J.J. Potoff, Fluid Phase Equilibr. **274**, 44–49 (2008).

[123] B. Eckl, J. Vrabec, and H. Hasse, Fluid Phase Equilibr. **274**, 16–26 (2008).